U. S. DEPARTMENT OF THE INTERIOR
GEOLOGICAL SURVEY

Petrography and Chemistry of Hydrothermal Manganese Oxyhydroxides from the Mariana and Izu-Bonin Volcanic Arcs, West Pacific

by

Marjorie S. Schulz and James R. Hein

Open File Report 91-557

ABSTRACT

Manganese oxyhydroxide-cemented sandstone and stratabound manganese oxyhydroxides were collected along the active Mariana Island Arc. X-ray diffraction shows three manganese oxide phases: a 10Å phase (todorokite and/or buserite), a 7Å phase (birnessite), and δ-MnO_2 (vernadite). The 10Å phase collapses to a 7Å phase in some samples on exposure to air. The collapse of the 10Å phase is most likely due to the absence of stabilizing cations.

Manganese oxyhydroxides that cement sandstone and breccia have several textural varieties: uniform cement, dendrite cement, dense layers and lenses, and fracture fill. Stratabound manganese oxyhydroxides occur as dense layers or lenses within sandstone and as curvilinear layers recovered with iron-rich mud. Stratabound manganese oxyhydroxides from several dredge sites have a morphology suggestive of mound deposits.

Microscopic textures of the manganese oxyhydroxide minerals are defined by morphology and crystallite size. Microscopic morphologies include the forms: colloform, homogeneous dense, laminated dense, porous fibrous, and scaly. Manganese oxyhydroxides occur in three crystalline forms: amorphous to cryptocrystalline (AC), microcrystalline, and crystallites.

SEM and electron microprobe analyses of the manganese oxyhydroxides show that AC manganese oxyhydroxides have very high water contents. AC oxides generally occur as the initial phase of mineralization and are also present as layers or laminae within colloform and laminated textures. The intercalation of AC and crystalline laminae probably reflects waxing and waning hydrothermal events or changing Eh and pH of hydrothermal fluids.

Manganese content of stratabound layers is as great as 48%, with an average of 42%. Mo, Zn, and Cd are concentrated in these manganese oxyhydroxide deposits. The chemical composition of manganese cemented sandstones is similar to stratabound deposits with an added detrital component. Chemical composition, textural, and mineralogical evidence all support a low temperature hydrothermal genesis for these deposits.

TABLE OF CONTENTS

INTRODUCTION

Marine ferromanganese oxyhydroxides (hereafter called Fe-Mn oxides) form by hydrogenetic, diagenetic, and hydrothermal processes. Fe-Mn oxide deposits produced by these processes can be distinguished by their mineralogy, morphology, chemistry, and texture (Hein et al., 1990). Hydrogenetic (precipitated from ambient seawater) Fe-Mn oxides comprise most of the Fe-Mn encrustations that coat hard substrate rocks throughout the ocean basins. Diagenetic Fe-Mn oxides precipitate from sediment pore waters and are the result of dissolution reactions, mobilization during oxidation-reduction reactions, and diffusion. Abyssal Fe-Mn oxide nodules form on a soft sediment substrate and are produced by both diagenetic and hydrogenetic processes. Hydrothermal Fe-Mn deposits were recognized initially at seafloor spreading centers (Scott et al., 1974) and are commonly the distal products of hydrothermal systems that produce massive sulfides. More recently, hydrothermal Mn oxyhydroxides (hereafter called Mn-oxides) have been collected from active volcanic arcs, along back-arc spreading centers, and on active mid-plate volcanic edifices (Cronan et al., 1982; Moorby et al., 1984; Koski et al., 1985; Usui et al., 1989; Hein et al., 1987). Hydrothermal Mn deposits occur as crusts coating substrate rock and as sediment-hosted deposits. Sediment-hosted hydrothermal Mn-oxide deposits occur as stratabound layers of Mn-oxides and as cements of clastic rocks, predominantly sandstones and breccias.

Each type of Fe-Mn oxide deposit has a characteristic chemical signature that can be used to identify its mode of deposition (Hein et al., 1990). However, many deposits formed from two of the three depositional mechanisms and have chemical compositions intermediate to those of the end members. For example, crusts from an active volcanic arc may have both hydrogenetic and hydrothermal layers and nodules form from both diagenetic and hydrogenetic processes.

Hydrothermal Mn-oxide deposits are chemically differentiated from hydrogenetic crusts and nodules by low iron and trace element contents, and higher Mn content (up to 48 wt.% Mn). Like abyssal nodules, hydrothermal deposits commonly contain the minerals todorokite, birnessite, and vernadite. Hydrothermal deposits are morphologically distinct. Hydrothermal stratabound deposits commonly have a metallic to submetallic luster and alternating dense and fibrous or porous layers (Kang and Hein, 1988), in contrast to the dull luster and earthy to vitreous textures of crusts and nodules.

Here, we describe the hydrothermal Mn-oxide deposits and host sediments recovered aboard the R/V *T. Thompson* (Cruise TT192) in the Mariana Island Arc, November and December 1985. This is a companion report to that of Hein et al. (1987) that described the samples, and reported general chemistry, and other data.

We used petrographic and scanning electron microscopy to determine Mn-oxide textures and x-ray diffraction to determine their crystallinity. The chemical compositions of the Mn-oxide deposits, reported by Hein et al. (1987), are discussed in the context of Mn mineralization and we report additional chemical analyses from inductively coupled plasma-atomic emission spectrometry and electron microprobe analysis. Relationships among the Mn-oxide crystallinity, mineralogy, chemical composition, and texture are synthesized into a model for the formation of hydrothermal Mn-oxide deposits.

Setting

The Mariana Island Arc extends from 12°N latitude to about 24°N latitude. North of 24° the arc is called the Izu-Bonin Arc. Bloomer et al. (1989a) divided the volcanically active Mariana Arc into three provinces based on the distribution of submarine and subaerial edifices: the Northern Seamount Province from 24°N to 20°30'N, the Southern Seamount Province from 16°30'N to 13°20'N, and the Central Island Province from Uracas Island at 20°30'N to Anataham Island at 16°30'N. These provinces are defined by

geomorphological and petrologic characteristics. The Northern and Southern Seamount Provinces are entirely submarine, whereas the Central Island Province contains many subaerially exposed volcanos and submarine volcanos. The islands of Guam, Rota, Tinian, Saipan, and Medinilla are within the forearc of the Southern Seamount Province and are not volcanically active. All of the hydrothermal Mn-oxide samples of this study are from the Central Island Province and the Northern Seamount Province, with one dredge from the Izu-Bonin Ridge (Fig. 1).

Island arc sedimentation

We would first like to describe the general characteristics of volcaniclastic sediments in volcanic arcs as the Mn-oxide deposits described here occur within these deposits. Clastic arc deposits are derived directly from eruptions, from reworking of juvenile volcaniclastic sediments, from epiclastic material of subaerial environments, and in some places from reefal debris. Pelagic sediment (foraminifera, radiolarians, etc.) is a small component of western Pacific arc deposits and probably represents accumulation during periods of volcanic dormancy. Hydrothermal deposits associated with volcanism, such as Mn-oxides, sulfate, and sulfide deposits, are also possible sources of detritus. Subaerial and subaqueous eruptive processes of volcanic arcs produce large amounts of detritus that result in extensive volcaniclastic aprons. Volcanism contributes many types of grains to the sediments including: pumice and glass lapilli, lithic fragments, individual crystal fragments (e.g. olivine, plagioclase and pyroxene), and fine-grained ash. The transport and deposition of arc sediments occur as direct deposition by fallout from an eruption column, pyroclastic flows, and turbidity currents and other gravity flows.

Mariana Arc sediments accumulated in the fore-arc, in the back-arc basin, in intra-arc basins between volcanic edifices, on the flanks of volcanos, and in pocket basins produced by faulting and other surface irregularities. Sedimentary rocks studied here were dredged from flanks of Mariana Arc seamounts. Some deposits are products of gravity movement; for example, dredge #41 recovered sub-rounded to sub-angular, pebbly sandstone and pebbly mudstone indicative of downslope transport. In contrast, dredge #73 sandstone is composed of delicate vesicular volcanic glass and euhedral crystals that probably formed *in situ* (as hyaloclastites) or with only minor reworking. Facies characterizations of clastic deposits in this study are difficult because problems with the single-channel seismic-reflection equipment prohibited lateral and stratigraphic correlations around the sampling sites.

The clast composition of sandstone is used to identify its provenance. In this study the only possible sources are the volcanic arc and pelagic debris. This work supports provenance models characterized by the QFL diagram developed by Dickinson et al. (1983). The QFL plot of point counts (Fig. 2) illustrates that the sandstones studied here (with one exception to be discussed later) fit within the undissected arc field, as expected. Large amounts of fresh glass attest to the chemical and mechanical immaturity of the sandstone.

Mineralization of volcanic arcs

Submarine volcanism and volcanically driven hydrothermal systems are important ore-forming processes. Some of the ore deposits that are the result (directly or indirectly) of submarine volcanism or volcanism in volcanic arcs include porphyry-type deposits, skarn deposits, massive sulfide deposits, and epithermal deposits (Guilbert and Park, 1986). Kuroko type massive sulfide deposits are one type of ore body that forms in submarine volcanic settings. The Mn-oxides of this study are likely either the distal products of larger hydrothermal systems, or the result of smaller, shallower epithermal systems.

Hydrothermal Mn-oxides from island arcs have been reported only recently. Cronan et al. (1982) described hydrothermal Mn-oxides from the active Tonga-Kermadec Ridge, an

island arc of the S.W. Pacific. Koski et al. (1985) and Hein et al. (1991) have described hydrothermal Mn-oxides of Tonga Ridge. Kang (1984) provided a detailed petrographic and morphologic description of hydrothermal oxyhydroxides from the Lesser Antilles (active arc) and Aves Ridge (remnant arc) of the eastern Caribbean. Usui (1986, 1989) reported on hydrothermal Mn-oxides deposits of the Kaikata seamount, of the active Bonin-Izu Arc. All of these island-arc Mn-oxide deposits have similar chemical compositions and morphology. The world-wide distribution of samples indicates that the processes of their formation are not local, but are a common consequence of submarine volcanism.

Samples and Methods

The primary objective of Cruise TT192 aboard R/V T. Thompson was to collect samples for a study of the petrologic and geochemical evolution of the Mariana volcanic arc. That work is being conducted by the chief scientists, R.J. Stern and S.H. Bloomer, and their students (Bloomer et al., 1989a, b; and Lin et al., 1989). Ferromanganese oxides samples were collected by J. R. Hein to study the mechanisms of their formation on an active arc. Hydrothermal Mn-oxide samples studied here are a subset of the Fe-Mn oxides (Hein et al., 1987). Figure 3 is a bathymetric map with location of dredges included in this study. Individual samples are numbered with dredge number (e.g. D1) and with a rock designation number (e.g. D1-1, D1-2, and D1-3).

Dredges

Working with dredged samples provides several challenges: 1) orientation of rocks (which side is up) is not known and cannot always be determined; 2) relationship of the recovered sample to the outcrop is difficult or impossible to know; 3) relationship of a rock to others from the same dredge is commonly unknown (e.g., are they pieces of the same strata or similar, but adjacent strata?); and 4) where were the samples collected along the dredge track? Under the best conditions, navigation at sea is precise to within 10's to 100's of meters; however, dredging at depth presents the added problem of the dredge bag location in relation to the ship's location. Some of these drawbacks can be overcome with careful logging of the dredges, description of the samples, petrographic studies, and correlation of dredge lines with seismic reflection profiles.

Methods

Petrographic examinations were performed on doubly polished thin sections using transmitted and reflected light. Chemical analysis of all samples was performed by the U.S. Geological Survey Analytical Chemistry Branch. Major and minor elements were determined using inductively coupled plasma-atomic emission spectrometry (ICP) by analyst H. Kirschenbaum (Kirschenbaum et al., 1989). Major oxides were determined by X-ray fluorescence spectroscopy.

X-ray diffraction analysis was performed using a Norelco generator with Cu-Kα radiation and a curved-crystal graphite monochrometer. Analog diffraction data were collected and analyzed for mineral identification and crystallinity determination.

Scanning electron microscopy (SEM) investigations were performed on doubly polished thin sections and on selected fracture surfaces of samples. Samples were carbon coated and investigated using backscattered and secondary electron imaging. Semi-quantitative chemical analyses were accomplished using an energy dispersion X-ray analyzer (EDX).

Major element analyses of doubly polished thin sections were performed on an ARL-SEMQ nine-spectrometer electron microprobe. Volcanic glass and manganese

oxyhydroxides were analyzed using a defocused beam (~50 μm) with an accelerating voltage of 15 kV and sample current of 10 nA. Counting times were 10 seconds. All raw microprobe data were reduced on-line with a modified version of the Bence-Albee method (Albee and Ray, 1970). For the standards used and the percent error for each element analyzed see Appendix I.

MINERALOGICAL STUDIES

Manganese oxyhydroxides

Manganese oxyhydroxide minerals include a 10 Å phase (todorokite and/or buserite), a 7 Å phase (birnessite), and a phase characterized by only two X-ray reflections (vernadite or δ-MnO_2). For this study these phases are defined by the X-ray diffraction spacings listed in Table 1. Even though the manganese phases are oxyhydroxides, we will refer to them as manganese oxides (Mn oxides).

Table 1: X-ray diffraction spacings of manganese oxyhydroxide phases in degrees 2θ and corresponding d-spacing in Å.

10 Å Phase		7 Å Phase		Vernadite	
2θ	Å	2θ	Å	2θ	Å
9.2	9.6	12.3	7.20	36.7	2.45
18.3	4.85	25.2	3.53	66	1.42
26	3.43	36	2.50		
36	2.50	44	2.06		
42	2.15	52	1.76		
52	1.76	66	1.42		
66	1.42				

Manganese oxide minerals and their structural relationships have been topics of scientific debate for a number of years (Turner et al., 1982; Burns et al., 1983; Giovanoli, 1985; Burns et al., 1985; Ostwald and Dubrawski, 1987; Usui et al., 1989). The validity of the mineral name todorokite was questioned by Giovanoli (1985) who favored calling the 10 Å phase buserite. However, Burns et al. (1985) refuted Giovanoli's assertion, and reaffirmed todorokite as a valid mineral species. Todorokite and buserite have similar X-ray diffraction reflections; therefore X-ray diffraction alone cannot differentiate between a todorokite structure and a buserite structure (Burns and Burns, 1977). Buserite has not been commonly reported because investigators identified any 10 Å phase present as todorokite. In order to avoid adding to the confusion, Mn-oxide phases discussed here will not be assigned specific mineral names.

There are two types of 10 Å phases in the samples from the Mariana Arc: 1) a 10 Å phase, that when exposed to air (dehydration and oxidation) collapses to a 7 Å phase (e.g. sample D3-8); and 2) a 10 Å phase that maintains a 10 Å d-spacing even after drying (e.g. D3-1). A majority of the samples seem to be a mixture of the two minerals; some of the 10 Å phase collapses to 7 Å and some of it does not. We regard the 7 Å phase (birnessite) to be a transformation product created by collapse of the structurally unstable 10 Å phase, whether or not the original 10 Å phase was identified by XRD (as does Usui, 1989).

Todorokite has a tunnel structure constructed with chains of edge-shared [MnO_6] octahedra. The tunnel "walls" are triple chains of [MnO_6] octahedra; the "floors" and "ceilings" are generally 3 chains wide (like the "walls"). The [3 x 3] tunnels are commonly

intergrown with tunnels that have "floors" and "ceilings" of other dimensions ranging from [3 x 2] to [3 x 8] and larger (Burns et al., 1983, 1985). When todorokite tunnels have "floors" and "ceilings" greater than three chains long they are structurally "unstable." Without stabilizing cations or absorbed water the tunnel structure collapses to a 7 Å phase (Fig. 4).

Buserite is a phyllo-manganate mineral originally identified from synthetically produced phases; it has been reported only a few times in the natural environment (Arrhenius and Tsai, 1981; Usui et al., 1989). Buserite consists of sheets of linked [MnO_6] octahedra that accommodate double layers of H_2O-OH and stabilizing cations (Usui, 1989). According to Usui (1989) (Fig. 4) both todorokite and buserite can collapse to a 7 Å phase. However, todorokite cannot completely collapse to a 7 Å phase because tunnel "walls" maintain the 10 Å d-spacing; only the center of larger tunnels will collapse. The 10 Å phase that collapses completely to 7 Å is presumably buserite.

In Mariana Arc samples, the 10 Å phase collapses totally to a 7 Å phase in six samples: D3-3I, D3-8, D41-3AI, D52-4-III, D52-10AII, and D55-4I. Samples D3-3I and D3-8 are the only two that were X-rayed quickly enough after exposure in air to document the transformation. D41-3AI, D52-4-III, D52-10AII, and D55-4I are presumed to have been a 10 Å phase initially, but they transformed completely to a 7 Å phase before being X-rayed. However, we cannot totally rule out the possibility that a primary 7 Å phase (birnessite) was present in these samples (see Ostwald and Dubrawski, 1987).

Figure 5 illustrates the complete collapse of a 10 Å phase to a 7 Å phase that took place in less than two weeks. Sample D3-8 was stored in water after collection. It was ground while wet and air dried for about 2 hours before being X-rayed the first time. The sample was then kept at room temperature for 2 weeks and X-rayed again. The transformation from a well crystallized 10 Å phase to a moderately crystalline 7 Å phase was complete.

None of the 10 Å phase transformed to a 7 Å phase in the following samples: D3-1, D3-3IV, D3-5, D8-2B, D8-8, D8-12-I, D8-12-II, D13-1-I, D15-1-I, D28-4-I, D28-4C, D28-4D, D28-7-I, D47-2-II, D54-2-I, D57-4-I, and D73-1C-B. All of the other samples showed some transformation to a 7 Å phase, but not complete transformation. These samples contain either a mixture of uncollapsed todorokite tunnels and buserite layers, or are partially collapsed todorokite tunnels.

Vernadite is the most highly oxidized and poorly crystalline Mn-oxide mineral found in the Mariana Arc samples. It has two characteristic X-ray reflections that are very broad: 2.40 to 2.45 Å and 1.40 to 1.42 Å. When both the 10 Å phase and the 7 Å phase are present, it is difficult to determine the presence of vernadite, as all three of these Mn-oxide minerals have X-ray diffraction reflections at these same d-spacings. In other words, vernadite has no distinctive X-ray reflections to differentiate it from the associated Mn-oxides when they are present. Burns and Burns (1977) suggested that vernadite is present when the reflection at 2.40 Å has a greater intensity than those at 7 Å or 9.2 Å. The X-ray reflections measured in this study at 2.40 Å to 2.45 Å and 1.40 Å to 1.42 Å are highly variable and rarely of greater intensity than the 7 Å or the 10 Å reflections. The d-spacings at 2.40 Å to 2.45 Å commonly produce asymmetric or double peaked reflections. In the diffractograms of samples run twice, the shape and size of the reflections commonly change (Fig. 6, Appendix II). The variability of these peaks is likely the result of changes in the 10 Å and 7 Å phases, and perhaps also changes of vernadite crystallinity. Vernadite is likely present in these samples; however, diffractograms were not analyzed quantitatively for its presence.

Crystallinity of manganese oxides

The crystallinity changes of the 10 Å to 7 Å minerals were studied by X-raying prepared diffraction slides several times after various intervals of time (ranging from 2 weeks to 2 years). Crystallinity (peak height / peak width at half height) of the Mn-oxide minerals is highly variable with X-ray diffraction peaks ranging from broad low-intensity

to sharp high-intensity peaks for the same mineral at the same 2θ angle (Appendices II and III). In general, crystallinity increases with increasing exposure to air. This is true for the non-collapsing 10 Å phase in most samples and for the 7 Å phase if present in the first X-ray diffractogram (XRD). However, increases in 7 Å phase crystallinity can be accompanied by either a decrease or an increase in the associated 10 Å phase crystallinity.

Changes in crystallinity are the result of dehydration through loss of both absorbed and structural water, and perhaps also oxidation of Mn-oxide phases. The increase in crystallinity of the 10 Å phase that does not transform to 7 Å is probably dehydration creating decreased distortion of the Mn-oxide tunnel structure. The few samples containing a 10 Å phase that does not transform to a 7 Å phase, or show an increase in crystallinity, must be in a stable crystalline state. The crystallinity of the 7 Å phase continued to increase with time because the 10 Å to 7 Å phase transformation proceeds with additional dehydration and oxidation.

Initial sub-samples for X-ray diffraction were run after various intervals of time following collection. Samples from the first dredges were X-rayed, and additional work was delayed many months. The amount of 10 Å Mn-oxides decreased in samples X-rayed after the delay. Figure 7 is a bar graph of the crystallinity data from Appendix III. In the first XRD's, the 10 Å phase crystallinity is high until sample D28-1A. At this point the analysis of the samples was delayed. After D28-1A, the 10 Å phase crystallinity is low in the initial runs, except for the samples that did not transform to the 7 Å phase.

The transformation of the 10 Å phase to the 7 Å phase does not appear to be related to the deposit type, texture, age of Mn-oxide deposit, or sandstone composition. Usui et al. (1989) related the stability of the 10 Å Mn-oxide phases to their proximity to the hydrothermal source, inferring that higher temperatures produce more stable 10 Å phases. The Kaikata Seamount (Izu-Bonin Arc) samples that Usui et al. studied were well located (box core and submersible samples) around a hydrothermal vent. Dredges gather samples over a wider area; therefore, proximal and distal samples of a hydrothermal vent can occur in the same dredge . The poor control of sample location in this study cannot definitely support or refute Usui's suggestion that the temperature of formation controls the stability of the Mn-oxide mineral.

Petrography of host sedimentary rocks

Most of the sandstones and breccias are volcaniclastic rocks derived from the volcanic arc; the remainder are foraminiferal sandstones containing minor siliciclastic debris. Clastic grains of unaltered samples consists of plagioclase and clinopyroxene, with minor olivine, orthopyroxene, amphibole, and quartz. Mineral grains are commonly euhedral. Pyroxene and plagioclase are commonly twinned and zoned, and less commonly embayed. Volcanic rock fragments and fresh volcanic glass fragments are present in all sections counted.

Point counts were completed for nine polished sections to classify the sandstones. For statistical accuracy, counts were continued until the total number of framework grains counted equaled 100. This resulted in higher total points counted for sections with more cement, matrix, and/or pore space (see Table 2 and Fig. 2).

Doubly polished thin sections (DPTS) were not point counted if composed only of stratabound Mn-oxides, nor were breccias or silty mudstones. The detrital grains in these rock types are either too sparse or too altered. With one exception, all sections counted plot within the undissected arc field of the QFL diagram (Fig. 2). The exception is a sandy siltstone (D28-6) that plots in the transitional arc field. This sample is from the west side of the cross-chain seamount, located west of Uracas Seamount. Its anomalous composition is due to its fine-grained nature which discriminates against the incorporation of and/or identification of lithic fragments. However, the presumably greater age of cross-chain seamounts at their western end also may be reflected by the sediment composition.

Several sandstones with unusual grain types were identified. One of these, a coarse-grained sandstone (D28-2), contains the typically altered volcanic rock fragments,

Table 2. Volcaniclastic and bioclastic sandstone point counts. D73-1C has two separate totals, one for each sandstone type.

Sample Number	D8-5	D8-12	D11-1	D28-6	D33-2	D73-1A	D73-1C	D73-1C	D73-1D
Volcanic Rock Fragments (VRF)	35	90	90	7	22	16	13	12	56
Altered VRF	12	-	-	7	25	28	6	7	5
Volcanic Glass	8	8	11	2	3	69	89	12	65
Pyroxene	5	2	2	5	7	3	1	10	10
Plagioclase	17	17	10	27	12	4	11	18	14
Quartz	1	-	-	-	-	-	-	-	-
Foraminifers		7	10	15	1	-	1	62	1
Dissolved Foraminifers	5	5	-	-	-	-	-	2	-
Radiolarians	-	-	-	2	-	-	-	1	-
Matrix	11	22	2	46	1	-	-	12	-
Fe rich matrix	5			6	10	-	-	-	-
Pore Space	11	9	6	17	32	29	24	7	48
Mn Cement	92	85	69	10	84	51	26	90	73
Total points counted	202	245	200	144	197	200	171	233	272
Lithic = glass plus all VRF	55	98	101	16	50	113	108	31	126
Mineral Crystals	23	19	12	32	19	7	12	28	24
All VRF = VRF + Altered VRF	47	90	90	14	47	44	19	19	61

plagioclase, and pyroxene grains, but also contains clasts of iron-rich mud, detrital barite, and detrital grains of polycrystalline quartz (presumably of hydrothermal origin). The provenance of this sandstone appears to have been, in part, a hydrothermal deposit.

The delicate structure of detrital glass in several sections indicates only minor transport before deposition. Dredge 73 recovered several sandstones with volcanic glass fragments as a major component (Appendix IV). Glass fragments are vesiculated and fragile. These sandstones have minor lithic fragments with both broken and euhedral mineral crystals. Sample D73-1D is a graded sandstone with coarse lithic fragments grading into fine glass and mineral fragments. Petrographic textures and hand sample textures of dredge 73 sandstones are suggestive of an eruptive center facies. However, microprobe analyses of volcanic glasses from samples D73-1D and D73-1A indicate that glass fragments are derived from two or more eruptive events and subsequently mixed by reworking. The glass fragments of this dredge follow a compositional trend that shows derivation from the

same parent magma (Table 3, Fig. 8). These samples probably represent reworked detritus from several eruptive phases of a single eruptive center.

Table 3. Compositions determined by electron microprobe (Wt %) of glass fragments in samples D73-1A and D73-1D.

	1A-1	1A-2	1A-3	1A-5	1A-6	1D-1	1D-2	1D-2B	1D-3	1D-4	1D-5	1D-6	1D-7
SiO_2	56.2	52.6	56.6	57.0	53.7	56.3	62.5	61.6	55.4	60.5	59.6	56.2	62.4
Al_2O_3	15.8	14.9	16.5	15.8	14.8	16.6	16.3	16.2	15.5	16.1	16.2	16.5	16.4
FeO	7.64	11.34	6.34	8.6	11.9	7.73	5.29	5.20	7.11	5.94	5.94	7.87	5.43
MnO	0.26	0.38	0.36	0.32	0.27	0.22	0.24	0.25	0.27	0.45	0.26	0.23	0.26
MgO	1.87	3.24	1.60	2.11	3.48	2.48	1.15	1.14	2.06	1.46	1.53	2.56	1.24
CaO	3.96	7.43	3.55	4.32	7.25	5.50	2.74	2.70	4.38	3.13	3.42	5.61	2.86
Na_2O	5.83	3.76	5.93	5.65	3.85	3.85	3.57	5.82	5.26	5.83	5.86	4.86	5.95
K_2O	3.74	1.04	3.93	3.87	1.01	3.17	3.87	3.85	2.88	3.42	3.33	3.08	3.92
P_2O_5	0.59	0.22	0.47	0.65	0.21	0.64	0.31	0.33	0.52	0.44	0.43	0.59	0.37
TiO_2	0.99	1.00	0.89	1.12	1.05	0.84	0.71	0.69	0.74	0.77	0.79	0.84	0.74
S(ppm)	443	537	440	234	739	698	294	321	345	454	488	650	214
Totals	97.0	96.0	96.3	99.5	97.9	97.5	96.8	97.9	94.2	98.2	97.5	98.5	99.6

Vesiculation and low sulfur content of submarine volcanic glass have been used as indicators of shallow or subaerial eruption (Moore and Schilling, 1973). The great depth at which many of these samples were collected and the low S content challenges that assumption (see Davis et al., 1991). Vesiculation may be an accurate indicator of subaerial eruption where magmas are mafic and less volatile rich (e.g. Hawaii), but vesicles do not seem to imply shallow or subaerial eruption in island arc settings where volatile content is generally high.

Mineralization and Diagenesis

Minor alteration of clastic grains occurs in every sample and involves the breakdown of volcanic glass and volcanic rock fragments to clay minerals (generally smectites) and (or) palagonite. However, alteration cannot be attributed exclusively to the Mn-oxide hydrothermal fluids. Alteration of sandstones, breccias, and other rocks occurs while they are exposed at the seafloor through halmyrolysis. The alteration in these rocks can be attributed to both halmyrolysis and mineralizing fluids.

Upon first petrographic examination, the replacement of clastic grains by Mn-oxides appears to be common; however, the grains are not replaced but rather coated by Mn-oxides. Manganese oxide coatings create an opaque homogeneous mass in transmitted light (Fig 9).

The alteration of glass and volcanic rock fragments from samples D28-2 and D73-1D can be directly attributed to mineralizing fluids. Sample D28-2 has a dense laminated stratabound layer of Mn-oxide at the base that is overlain by volcanic rock fragments. The most highly altered volcanic rock fragments occur immediately above the stratabound layer. Sample D73-1D has a cross-cutting fracture infilled with dense Mn-oxides. The volcanic-

glass fragments to either side of the fracture are highly altered to a greenish-yellow clay mineral (celadonite?). Away from the fracture the glass is less altered. In both of these samples mineralizing fluids caused more intense alteration near the fluid pathway.

Replacement of mineral grains is rare compared to replacement of foraminifers and radiolarians. Figure 10A illustrates a pyroxene replaced by Mn-oxide from sample D33-2-3, the only sample found to have replaced mineral grains. Figure 10B is a SEM backscatter electron photomicrograph of a foraminifera that is partly replaced by Mn-oxides. Molds of foraminifers and radiolarians are very common. In forming molds the Mn-oxides permeated and preserved the fine structure and ornamentation of the test, producing internal and external casts after dissolution of the tests. Formation of molds is more common in originally calcareous, rather than siliceous tests.

These relatively minor effects of mineralizing fluids on host sediments negate the possibility of high fluid temperatures. In most DPTS's, there is fresh volcanic glass cemented by Mn-oxides. Volcanic glass degrades readily to palagonite or clay minerals under ambient temperatures and pressures on the seafloor, and degradation is enhanced with increased temperatures. If mineralizing fluid temperatures were high (> 150° C), unaltered volcanic glass would be rare.

TEXTURAL STUDIES

Hand sample textures

Manganese oxides are dark-brownish grey to black. Their luster ranges from dull and earthy to metallic. Appendix V gives detailed descriptions of each dredge and the textures of Mn-oxides present. Hand samples are either Mn-oxide-cemented sedimentary rocks or stratabound Mn-oxides. Stratabound Mn-oxides either occur as dense layers within Mn-oxide-cemented sedimentary rocks or were recovered without host sediment.

Manganese oxides in cemented sandstones have several textural varieties: 1) evenly distributed uniform cement, 2) fingers or dendrites of Mn-oxide cement oriented perpendicular to bedding, with poorly cemented sediments between the dendrites, 3) dense layers and lenses within the sandstones and breccias (stratabound layers), and 4) fracture fill within breccias.

The lower surfaces of stratabound Mn-oxide layers commonly are polished, metallic to submetallic, and botryoidal. These layers formed at various stratigraphic intervals, such as bedding planes, fractures, or in intervals of textural contrast. As sediment is cemented, pore space decreases and pore pressures rise. Dense Mn-oxide layers within sandstones may represent the localization and concentration of precipitation from mineralizing fluids as porosity decreased.

Dredges 3, 20, and 28 recovered stratabound Mn-oxides without associated sediment. The stratabound layers consist of intercalated dense Mn-oxides and fibrous porous Mn-oxides; both are associated with X-ray amorphous iron-rich muds presumably of hydrothermal origin. Muds of hydrothermal origin were also recovered with stratabound Mn-oxides in the Lau Basin, South Pacific (Hein et al., 1991). The morphology of samples from dredges 3, 20, and 28 is reminiscent of stockwork veining with the enclosing sediments washed away. These samples may represent near seafloor exhalative deposits precipitated from manganese-rich fluids. They probably formed within hydrothermally precipitated iron-rich muds, possibly shallow mounds, that provided a matrix for deposition of the stratabound Mn-oxides (Hein et al. 1987). It is likely that these mounds are unstable, as indicated by a slump fold in sample D28-4 (Appendix V). The electron microprobe analyses of sample D3-3 supports the interpretation of near seafloor deposition and will be discussed in further detail later.

Microscopic manganese oxide textures

Textural descriptions (Appendix IV) are based on the study of 27 doubly polished thin sections from selected samples. A variety of Mn-oxide morphologies occur: colloform, homogeneous dense layers, laminated dense layers, porous fibrous, and scaly. Within these forms the Mn-oxides have three crystalline textures: crystallites, microcrystallites, and amorphous cryptocrystalline (AC). These textures are similar to those described by Kang (1984) for hydrothermal samples from the West Antilles Volcanic Arc.

Textures are defined principally on the basis of crystallite size differences. Crystallites are accicular needles of Mn-oxides up to 500 μm long and occur in three forms: aligned layers of crystallites, mosaics of crystallites, and radially aligned crystallites (Fig. 11A, B). Microcrystalline Mn-oxides are crystalline but do not have individually distinguishable crystallite forms (Fig. 12). Amorphous cryptocrystalline (AC) Mn-oxides are isotropic in polarized reflected light and distinguishable by differential relief in plane light. The AC oxides appear softer and usually have lower relief than microcrystallites and crystallites. AC oxides may be X-ray amorphous, but occur in areas too small to isolate for X-ray diffraction analysis.

AC oxides have no discernible crystallinity. Microprobe and SEM investigations indicate that they are of similar chemical composition to crystallites and microcrystallites, however they have a much higher water content. The amorphous to cryptocrystalline designation was given to describe the extremely fine-grained texture; however, the true structural and crystallographic characteristics of this phase remain unknown.

The morphology of structures that the three different crystallite sizes occur in are: colloform, scaly, homogeneous dense layers, laminated dense layers, and porous-fibrous layers. Colloform botryoids are composed of alternating laminae of aligned crystallites, microcrystallites, and AC Mn-oxides. Colloform Mn-oxides can be densely packed or have pore space between botryoids. Colloform textures commonly coalesce into layers (Fig. 13). Homogeneous layers are generally microcrystalline. Laminated textures are generally composed of intercalated microcrystalline and crystalline laminae (Fig. 13). Porous, fibrous Mn-oxides consist of elongate fibers that are commonly subparallel and rarely dendritic (Fig. 14). Fibrous porous areas on an outer surface give a sample a "hairy" look. In thin section, fibrous, porous oxides generally are amorphous to cryptocrystalline, although microcrystalline fibers also exist. Scaly Mn-oxides consist of scallops of radially aligned crystallites arranged like shingles or scales (Fig. 15).

The scanning electron microscope was used to elucidate textural relationships in more detail. Porous fibrous Mn-oxides from a fracture surface of sample D3-3 are illustrated in figure 16A. Fibers are subparallel with very irregular surfaces. Broken fibers show a homogeneous internal structure. In contrast, Figure 16B shows a colloform botryoid composed of layers of aligned crystallites.

A fracture surface of sample D44-4 illustrates colloform Mn-oxides overlain by radially aligned crystallites (Fig. 17). The backscattered electron image (Fig. 17A) shows intercalated AC oxides and microcrystalline oxides within the colloform structures. The AC oxides are dark in backscattered electron images because water content is high, thereby decreasing the average atomic weight. The secondary image (Fig. 17B) provides an excellent view of the Mn-oxide crystallites. The upper left corner (Fig. 17B) shows an outer surface of aligned crystallites illustrating their open network.

Discussion of textures and their genetic significance

AC oxides form the cores for radially aligned crystallites and are intercalated with microcystallites or crystallites in colloform and laminated structures (Fig. 18). In many cases AC oxides appear to be the initial phase of Mn-oxide deposition. As deposition continues, the precipitation of Mn-oxides occurs outward from the AC cores or layers.

In the SEM images of Figure 18, laminae of aligned crystallites and AC oxides are illustrated. In the backscattered image (Fig. 18B) crystallites are of a higher mean atomic number (brighter) than the AC oxides. The difference in brightness indicates that areas of AC texture have a chemical composition different from the crystalline areas. SEM-EDX and electron microprobe studies determined this difference in mean atomic number to be due to water content.

Formation of AC Mn-oxides may be due to rapid oxidation and, consequently, rapid precipitation as mineralizing fluids mix with oxygenated pore water. The rapid precipitation resulted in extremely fine grained (cryptocrystalline) material. The crystallite and microcrystalline textures probably represent slower reaction kinetics due to less oxygenated pore waters, fluids with less manganese enrichment, or longer intervals of precipitation.

The waxing and waning of mineralizing fluids (hydrothermal events) interacting with oxygenated pore fluids may account for the occurrence of intercalated AC oxides, microcrystallites, and crystallites within the colloform and laminated Mn-oxides.

CHEMICAL STUDIES

Composition of bulk samples

Chemical analyses by ICP spectrometry were completed on 60 sub-samples of Mn-oxide cemented sandstone, stratabound Mn-oxide, Fe-Mn crusts, and related sediments. These data are separated by deposit type and presented in Appendix VI. Analyses of Mn-oxides cemented sandstones were completed on bulk samples; therefore the chemistry is influenced greatly by the sediment composition (Appendix VI, Section 1). Analyses of stratabound deposits included layers removed from their sandstone and breccia hosts, and stratabound deposits not part of a sandstone or breccia (Appendix VI, Section 2). Appendix VI, Section 3 contains the data from analyses of samples of mixed genetic origin (ferromanganese crusts) and analyses of unusual composition, (e.g. samples from dredge 33 with late stage hematite mineralization).

Mean, median, standard deviation, maximum, and minimum values are given for each set of data in Tables 4, 5, and 6. In general, the elements Si, Fe, Al, Ti, Mg, Ca, Co, Cu, Ni, Pb, As, Cr, Y, and Ce are present in greater amounts in the Mn-oxide cemented sandstones. Greater abundances of Si, Al, Fe, Mg, Ti, Ca, Cr, and Y are due to host rock minerals. These elements are present in concentrations similar to those of the associated igneous rocks (Table 7). Water content increases with increasing manganese content. High total water values (up to 27 weight %) are due to water adsorbed by the Mn-oxide minerals.

Table 7 contains the mean elemental composition of igneous rock samples from the same dredges as the Mn-oxides of this study. Comparison of the trace element concentrations in hydrothermal Mn-oxides with their concentrations in associated igneous rocks reveals that some are hydrothermally concentrated. Enrichment factors for Mn-oxide cemented sediments and stratabound Mn-oxides were calculated as the ratio of the high concentration / the low concentration of the element. Negative factors indicate a depletion of

Table 4. Statistical analysis of manganese oxide cemented sandstone chemistry.

	N	Mean	Median	Min	Max	St .Dev.
Fe %	16	8.56	6.05	1.61	24.90	6.24
Mn	16	13.87	13.35	4.40	27.40	5.04
Si	16	14.82	16.03	6.31	24.17	4.91
Na	16	2.0	2.01	0.99	2.670	0.48
Al	16	4.72	5.80	0.40	7.90	2.22
Ti	16	0.36	0.34	0.06	0.81	0.19
K	16	0.93	0.82	0.36	2.03	0.46
Mg	16	2.36	2.055	1.08	6.6	1.30
P	16	0.1179	0.075	0.029	0.38	0.11
Ca	16	4.418	3.8	0.93	8.5	2.10
H_2O+	16	4.356	3.70	1.80	9.5	2.06
H_2O-	16	3.737	2.85	1.20	10.3	2.29
CO_2	16	0.668	0.07	0.01	5.9	1.59
Mo ppm	15	146.9	140.0	38	380	87.4
Co	16	312	52	18	1400	458
Cu	16	491	215	44	4000	948
Ni	16	446	230	38	1700	513
Pb	10	227	40	20	1100	368
Sr	16	541.2	475.0	210	1200	270.7
V	16	277.6	235.0	81	640	158.2
Zn	16	296.2	275.0	85	560	159.1
As	15	101.7	20.0	9	800	204.4
Ba	16	1136	1000	230	2800	819
Cd	16	6.62	6.00	0.35	22	5.36
Cr	16	29.66	18.50	4	140	34.18
Y	16	38.4	23.5	13	150	40.8
Ce	11	90.7	31.0	10	430	141.4

Table 5. Statistical analysis of ICP chemistry of stratabound deposits.

	N	Mean	Median	Minimum	Maximum	St.Dev.
Fe %	26	1.54	0.665	0.074	6.3	1.888
Mn	26	42.25	44.25	32.40	48.0	4.554
Si	26	2.044	1.305	0.050	7.29	2.235
Na	26	2.461	2.410	1.370	3.56	0.595
Al	26	0.645	0.500	0.10	2.7	0.577
Ti	22	0.053	0.04	0.01	0.14	0.03408
K	26	0.972	0.9500	0.260	1.65	0.3620
Mg	26	1.734	1.815	0.680	2.71	0.577
P	16	0.0907	0.0785	0.0260	0.19	0.0495
Ca	26	1.651	1.60	0.970	2.76	0.3835
H_2O+	26	7.846	7.750	5.50	10.3	1.239
H_2O-	26	7.231	6.900	3.00	20.1	3.100
CO_2	26	0.144	0.060	0.010	1.50	0.3068
Mo ppm	26	593.5	525	230	1300	276.6
Co	22	100.2	68	6.4	470	110.3
Cu	26	235.7	120	13	910	270.9
Ni	26	295.7	185	30	950	268.3
Pb	17	74.5	68	10	150	50.5
Sr	26	502.7	485	260	1100	163.6
V	17	275.2	270	30	770	178.6
Zn	25	2395	260	18	12100	3775
As	26	62.04	49	28	140	29.70
Ba	26	1353	910	450	5000	1196
Cd	23	20.67	13.0	0.50	79	22.41
Cr	19	3.147	2.50	1	7	1.800
Y	19	18.54	17.0	6.9	54	12.02
Ce	7	21.57	17.0	11	41	10.80

Table 6. Statistical analyses of ferromanganese crusts and mixed origin samples.

	N	Mean	Median	Minimum	Maximum	St. Dev.
Fe %	16	8.34	6.55	2.24	19.50	5.00
Mn	16	17.50	15.65	1.06	36.10	10.09
Si	15	12.53	14.73	5.38	20.76	5.22
Na	15	2.013	2.000	1.460	3.120	0.406
Al	16	4.443	4.550	1.640	7.600	1.996
Ti	16	0.3562	0.3300	0.1000	0.8800	0.2289
K	16	1.058	0.930	0.480	1.890	0.450
Mg	16	2.100	2.110	1.020	3.400	0.701
P	15	0.1459	0.1000	0.0390	0.5600	0.1321
Ca	16	3.530	3.150	1.560	6.600	1.620
H_2O+	15	5.547	6.000	1.600	8.400	1.978
H_2O-	15	4.853	4.000	1.200	11.000	3.122
CO_2	15	0.2840	0.1500	0.0200	0.9300	0.324
Mo ppm	14	268.3	225.0	19.0	730.0	235.5
Co	15	374	100	33	2700	688
Cu	16	290.6	170.0	45.0	1300.0	341.4
Ni	16	462	235	54	2300	664
Pb	7	376	55	28	1600	573
Sr	16	550.6	460.0	290.0	1300.0	252.4
V	16	244.2	240.0	24.0	640.0	161.3
Zn	16	448	215	83	3600	850
As	15	72.4	24.0	3.0	320.0	86.7
Ba	16	806	740	290	2200	459
Cd	15	5.49	4.70	0.30	16.00	5.02
Cr	16	22.63	13.50	2.00	85.00	24.23
Y	16	39.7	18.5	9.8	200.0	50.1
Ce	11	140.7	27.0	17.0	830.0	243.7

the element compared to its concentration in igneous rocks, and a positive factor indicates an enrichment of the element in the Mn-oxide deposits. Enrichment factors show that higher contents of Cu, Ni, and Ba in the manganiferous deposits are due to the hydrothermal concentration of these elements. Chromium with a negative enrichment factor is not transported by the hydrothermal fluids whereas, K, Sr, V, and possibly Y are present in concentrations comparable to the associated igneous rocks.

Table 7. Average trace element comparison of Mariana Arc igneous rocks (Lin et al., 1989: and Bloomer et al., 1989) and hydrothermal manganiferous deposits of this study. All analyses are in ppm. The highest abundance of the element is in boldface. Enrichment factors are the ratio of high abundance / low abundance, negative factors indicate a depletion of the element in Mn-oxide deposits compared to its concentration in igneous rocks. A positive factor indicates an enrichment of the element in the Mn-oxide deposits.

	Igneous Rocks	Manganese Sandstones	Enrichment Factor, Sandstones	Stratabound Manganese	Enrichment Factor, Stratabound
K	**10797**	9340	-1.2	9715	-1.1
Sr	**634.6**	541.2	-1.2	502.7	1.3
Ba	443.2	1136	2.6	**1353**	3.1
Ce	40.3	**90.7**	2.3	21.6	-1.9
Y	22.1	**38.4**	1.7	18.5	-0.8
V	267.9	**277.6**	1.0	275.2	1.0
Cr	**79.33**	29.7	-2.7	3.2	-25.2
Ni	33.7	**446**	13.2	295.7	8.8
Cu	118.3	**491**	4.2	235.7	2.0

Manganese is present in greater amounts in the stratabound deposits relative to the Mn-oxide cemented sandstones because it is not diluted by detrital material. Stratabound deposits are also enriched in H_2O^+, H_2O^-, Mo, Zn, and Cd. Concentrations of Mo, Zn, Co, and Cd were not measured for associated igneous rocks of the Mariana Arc. However, the Mn-oxides are enriched in these metals compared to concentrations in igneous rocks of intermediate composition from other areas (Table 8).

Table 8. Range of trace element abundances (in ppm) in manganiferous deposits compared with range of abundances in igneous rocks of intermediate composition.

	Intermediate Igneous[1]	Manganese Sandstones	Enrichment Factor, Sandstone	Stratabound Manganese	Enrichment Factor, Stratabound
Mo	0.7 to 1.0	38 to 380	54 to 380	230 to 1300	329 to 1300
Zn	60 to 90	85 to 560	1.4 to 6.2	18 to 12100	-3.3 to 134
Cd	0.017 to 0.32	0.35 to 22.0	21 to 69	0.50 to 79.0	29 to 247
Co	13 to 28	18 to 1400	1.8 to 50	6.4 to 470.0	-2 to 17

[1]Values from Govett, 1983

Zinc, Co, Cd, and especially Mo may be indicators of hydrothermal activity; however, the wide range in concentration within the deposits indicates that these elements are

hydrothermally concentrated in some samples but not in others. Figure 19 is a scatter plot of Zn vs Mn concentration, all but seven analyses are less than 1,000 ppm Zn. The seven high-Zn analyses are layers from sample D28-1. Zinc is generally expected to be fractionated in hydrothermal systems through concentration in proximal sulfide facies. The high Zn content in D28-1 may be indicative of a relatively more proximal deposit.

Correlation coefficient matrices were calculated for the compositional data from stratabound Mn-oxides and manganiferous sandstones (Tables 9 and 10). The correlations common to both data sets are not surprising; Mn correlates negatively to Si, Si correlates positively with Al and correlates negatively with H_2O^+, and Ce has a strong positive correlation with Co. (Correlations are considered strong when they are above r =0.80 at the 99% confidence level.)

Silicon correlates negatively to Mn and H_2O^+ because water is concentrated in the Mn phase. A positive correlation of Si and Al reflects the aluminosilicate fraction.

Elements from manganiferous sandstones have more statistically significant correlations than do the stratabound Mn-oxide elements (bold faced in Tables 9 and 10). There are many components present in the cemented sandstones such as volcaniclastic sediment, biogenic debris, hydrothermal precipitates, and hydrogenetic precipitates; each component has unique chemical characteristics. Correlation of elements within detrital components increases the number of significant correlations. On the other hand, stratabound deposits have only one major component, the hydrothermal Mn-oxides.

In the stratabound layers, Cu has strong positive correlation with Ni (r= 0.808) and Zn (r= 0.800), and a moderate correlation with Cd (r=0.612) (Table 10), indicating that all four of these elements are products of hydrothermal processes. However, in the Mn-oxide cemented sandstones Cu has a moderate positive correlation only with Ba. This correlation may be indicative of a biogenic source (Bruland, 1983; Hein et al., 1991). In Mn-oxide cemented sandstones, Ni correlates positively with Pb, Y, Ce, Zn, and V. The hydrothermal chemical signatures appear to be masked by other components in the cemented sandstones.

Cobalt is concentrated in some of the manganiferous deposits and not in others, similar to Mo and Zn. Care must be taken when interpreting Co concentration. High Co in ferromanganese crusts is an indication of hydrogenetic enrichment (Hein et al., 1988). Rather than being concentrated hydrothermally, Co content in hydrothermal Mn-oxides may be an indication of seafloor exposure as Co can be concentrated by absorption on to the Mn-oxides. Like cobalt, cerium is concentrated from seawater by oxidation. A negative Ce anomaly is commonly used as an indicator of hydrothermal activity (Fleet, 1983). The correlation of Ce with Co supports the conclusion that in these samples both are concentrated from seawater rather than from hydrothermal fluids.

Molybdenum is present in lower concentrations in the Mn-oxide cemented sedimentary rocks than in the stratabound Mn-oxide deposits (Fig. 20). Stratabound deposits have a wide range of Mo values (230 to 1300 ppm). The reason for this variation in Mo concentration between the hydrothermal systems is currently unexplained. Cobalt and Mo have a moderate positive correlation in the Mn-oxide cemented sandstones, but not in the stratabound deposits. This correlation may indicate that the Mo in the Mn-oxide cemented sandstones is not due to simple hydrothermal concentration; Mo must be present in other components of the cemented sedimentary rocks.

Composition of microscopic textures by electron microprobe analysis

Electron microprobe analyses of crystalline, microcrystalline, and amorphous-cryptocrystalline (AC) Mn-oxides are presented in Tables 11 and 12. Microprobe spot

Table 9. Correlation coefficient matrix for manganese cemented sandstone chemical analyses that are presented in Table 5. Correlations at greater than 99% confidence level are boldface.

	Fe	Mn	Si	Na	Al	Ti	K	Mg
Mn	-0.009							
Si	**-0.630**	**-0.675**						
Na	**-0.786**	0.082	0.500					
Al	-0.591	-0.421	**0.658**	**0.625**				
Ti	0.172	-0.511	0.088	-0.036	0.097			
K	-0.180	0.462	-0.148	0.177	0.107	-0.371		
Mg	-0.281	-0.207	0.293	-0.284	-0.197	-0.006	-0.116	
P	**0.893**	0.063	-0.696	-0.584	-0.494	0.409	-0.083	-0.434
Ca	**-0.638**	-0.178	0.312	0.292	0.374	0.023	-0.216	0.397
H2O+	**0.816**	0.494	**-0.839**	-0.496	-0.595	-0.101	0.104	-0.551
H2O-	0.574	0.259	-0.604	-0.274	-0.379	0.236	-0.065	-0.463
CO2	-0.322	0.399	-0.265	0.290	-0.035	-0.220	-0.064	-0.173
Mo	**0.721**	0.191	-0.481	-0.587	-0.430	-0.366	-0.004	-0.396
Co	**0.909**	0.044	**-0.668**	**-0.645**	-0.521	0.315	-0.197	-0.411
Cu	0.241	-0.046	-0.079	-0.272	-0.090	-0.017	0.055	-0.089
Ni	0.513	-0.081	-0.352	-0.334	-0.304	0.589	-0.153	-0.250
Pb	**0.883**	-0.391	-0.542	**-0.679**	-0.568	**0.773**	-0.573	**-0.757**
Sr	0.444	0.167	-0.604	-0.244	-0.160	0.555	0.185	-0.354
V	0.450	-0.375	-0.197	-0.405	-0.289	**0.869**	-0.369	0.153
Zn	0.335	-0.104	-0.116	-0.191	-0.196	0.525	-0.046	-0.098
As	**0.877**	0.158	-0.614	**-0.651**	-0.528	-0.208	-0.166	-0.360
Ba	0.377	0.306	-0.362	-0.328	-0.182	-0.256	0.201	-0.274
Cd	-0.281	0.227	0.110	0.241	0.025	-0.091	0.770	0.169
Cr	-0.100	-0.364	0.292	-0.428	-0.236	0.050	-0.313	**0.901**
Y	0.526	-0.172	-0.367	-0.231	-0.205	**0.806**	-0.317	-0.364
Ce	**0.866**	-0.238	-0.514	-0.496	-0.548	**0.855**	-0.436	-0.583

	P	Ca	H2O+	H2O-	CO2	Mo	Co	Cu
Ca	-0.578							
H2O+	**0.811**	**-0.685**						
H2O-	**0.750**	-0.571	**0.685**					
CO2	-0.204	**0.627**	-0.025	-0.103				
Mo	0.521	**-0.727**	**0.791**	0.480	-0.166			
Co	**0.955**	-0.586	**0.814**	**0.716**	-0.208	**0.613**		
Cu	0.139	-0.280	0.191	-0.047	-0.174	0.303	0.338	
Ni	**0.685**	-0.451	0.425	0.608	-0.240	0.223	**0.750**	0.581
Pb	**0.956**	-0.409	**0.787**	**0.769**	-0.153	0.259	**0.969**	0.160
Sr	**0.765**	-0.201	0.510	0.592	0.019	0.039	**0.659**	0.061
V	0.609	-0.119	0.118	0.377	-0.294	-0.160	0.561	0.138
Zn	0.414	-0.569	0.259	0.504	-0.453	0.147	0.435	0.419
As	**0.688**	-0.556	**0.831**	0.466	-0.149	**0.802**	**0.715**	0.038
Ba	0.261	-0.581	0.543	0.398	-0.227	**0.646**	0.394	**0.614**
Cd	-0.203	-0.233	-0.161	-0.076	-0.265	-0.274	-0.336	-0.054
Cr	-0.275	0.336	-0.467	-0.406	-0.233	-0.242	-0.179	0.047
Y	**0.784**	-0.306	0.414	0.696	-0.121	0.088	**0.739**	0.110
Ce	**0.969**	-0.381	**0.747**	**0.749**	-0.137	0.079	**0.911**	-0.004

	Ni	Pb	Sr	V	Zn	As	Ba	Cd
Pb	**0.894**							
Sr	**0.637**	**0.838**						
V	**0.731**	**0.906**	0.611					
Zn	**0.766**	0.540	0.329	0.542				
As	0.116	**0.972**	0.180	0.027	0.011			
Ba	0.407	-0.008	0.093	-0.128	0.566	0.378		
Cd	-0.072	-0.526	-0.014	-0.121	0.306	-0.365	0.116	
Cr	-0.078	0.041	-0.328	0.244	-0.057	-0.206	-0.235	-0.040
Y	**0.838**	**0.964**	**0.765**	**0.816**	**0.636**	0.186	0.096	-0.193
Ce	**0.801**	**0.973**	**0.855**	**0.939**	0.509	**0.958**	-0.142	-0.292

	Cr	Y
Y	-0.208	
Ce	-0.220	**0.974**

Table 10. Correlation coefficient matrix for stratabound manganese oxide chemical analyses that are found in Table 6. Correlations at greater than 99 % confidence level are boldface.

	Fe	Mn	Si	Na	Al	Ti	K	Mg
Mn	**-0.792**							
Si	**0.845**	**-0.912**						
Na	0.053	-0.209	0.323					
Al	0.284	**-0.647**	**0.649**	0.131				
Ti	0.335	**-0.538**	**0.598**	-0.127	**0.814**			
K	0.208	-0.069	0.035	**-0.800**	0.063	0.256		
Mg	-0.316	0.186	-0.327	**-0.702**	0.040	0.178	**0.663**	
P	0.060	0.035	-0.105	0.392	-0.354	-0.098	-0.517	-0.212
Ca	-0.182	-0.171	0.208	**0.564**	0.522	0.305	-0.407	-0.277
H2O+	-0.443	0.461	**-0.586**	-0.228	-0.281	-0.282	-0.208	0.202
H2O-	-0.070	-0.219	-0.045	0.245	-0.099	-0.169	-0.480	-0.233
CO2	0.110	-0.352	0.260	-0.127	**0.651**	0.458	0.267	0.235
Mo	0.065	0.179	-0.040	0.212	-0.165	-0.302	-0.145	**-0.574**
Co	0.626	-0.258	0.241	-0.367	-0.067	0.096	0.326	-0.016
Cu	-0.135	0.134	-0.139	-0.197	-0.056	0.154	0.084	0.365
Ni	-0.019	0.071	-0.125	-0.545	0.054	0.291	0.417	0.436
Pb	-0.426	0.506	-0.531	-0.193	-0.375	0.086	-0.152	0.364
Sr	-0.125	0.223	-0.245	**-0.757**	0.044	0.298	**0.663**	0.403
V	-0.412	0.205	-0.322	-0.172	-0.143	-0.124	-0.100	0.342
Zn	-0.321	0.313	-0.343	-0.018	-0.230	0.014	-0.125	0.266
As	0.063	0.103	-0.019	0.238	-0.135	-0.119	-0.265	-0.681
Ba	0.070	0.043	-0.023	**-0.548**	0.080	0.126	0.424	0.178
Cd	-0.297	0.203	-0.270	-0.202	-0.173	0.238	0.068	0.407
Cr	0.388	-0.063	0.031	-0.303	-0.214	0.001	0.306	-0.358
Y	-0.444	0.524	-0.493	-0.530	-0.165	-0.088	0.264	0.318
Ce	0.575	-0.128	0.225	-0.006	-0.036	-0.050	-0.026	-0.291

	P	Ca	H2O+	H2O-	CO2	Mo	Co	Cu
Ca	-0.118							
H2O+	0.286	-0.201						
H2O-	0.535	-0.013	0.131					
CO2	-0.184	0.391	-0.227	-0.155				
Mo	-0.359	0.023	-0.118	-0.167	-0.229			
Co	0.053	-0.423	0.055	-0.123	0.148	0.052		
Cu	0.441	-0.344	0.052	-0.020	-0.154	-0.238	-0.061	
Ni	0.069	-0.403	0.081	-0.161	-0.046	-0.062	0.139	**0.808**
Pb	0.462	-0.424	**0.674**	0.457	-0.256	-0.398	-0.016	0.581
Sr	-0.450	-0.318	0.110	-0.297	0.201	0.020	0.112	-0.032
V	0.389	-0.239	0.224	0.281	-0.151	-0.420	-0.309	0.107
Zn	**0.713**	-0.220	0.211	0.072	-0.139	-0.261	-0.161	**0.800**
As	-0.020	0.210	-0.058	-0.031	-0.182	**0.782**	-0.073	-0.304
Ba	-0.332	-0.395	-0.031	-0.221	0.087	-0.001	0.029	0.001
Cd	0.546	-0.310	0.226	0.038	-0.141	-0.293	-0.138	**0.612**
Cr	-0.013	-0.204	0.119	-0.291	0.024	0.399	**0.571**	-0.369
Y	-0.177	-0.373	0.354	-0.188	-0.186	**0.572**	-0.263	0.240
Ce	-0.424	-0.032	-0.360	0.189	-0.320	0.423	**0.931**	0.085

	Ni	Pb	Sr	V	Zn	As	Ba	Cd
Pb	0.350							
Sr	0.403	0.001						
V	-0.008	**0.644**	0.143					
Zn	0.441	**0.701**	-0.193	0.084				
As	-0.075	-0.373	0.142	-0.186	-0.309			
Ba	0.262	-0.068	**0.691**	0.586	-0.195	0.137		
Cd	0.359	**0.618**	-0.047	0.202	**0.799**	-0.343	-0.064	
Cr	0.026	-0.191	0.401	-0.143	-0.369	**0.639**	0.234	-0.521
Y	0.437	0.178	0.558	0.101	0.162	0.393	0.406	0.220
Ce	0.297	0.049	-0.127	0.208	-0.336	0.108	-0.043	-0.390

	Cr	Y
Y	-0.001	
Ce	0.294	-0.204

Table 11. Electron microprobe analyses of crystalline and microcrystalline manganese oxides. All amounts are in weight %. Sample numbers in left column correspond to numbers on figures 21 through 23.

	Na	Mg	Si	S	Ca	Ti	Mn	Fe	Ni	Cu	Mo	Ba	Pb
D3-3A	1.80	0.19	-		0.26	0.01	22.2	0.02	0.01	-	0.01	-	0.04
D3-3B	1.91	0.25	-	0.03	0.29	-	24.3	0.05	0.01	-	0.02	0.01	0.03
D3-3C	1.94	0.25	-	0.01	0.30	-	24.5	0.04	-	-	0.03	0.02	-
D3-3D	1.86	0.26	-	0.00	0.28	-	25.3	0.04	0.02	-	0.01	-	0.03
D3-3E	2.14	0.34	-	0.02	0.32	-	27.7	0.04	-	-	0.03	0.02	0.04
D3-3H1	1.78	0.21	-	0.02	0.26	-	22.0	0.02	-	-	0.05	-	0.07
D3-3H2	1.80	0.20	-	0.03	0.26	-	21.8	0.02	0.02	-	0.03	-	-
D3-3H3	1.92	0.25	-	-	0.29	-	24.8	0.04	0.02	-	0.01	-	0.07
D3-3H4	1.91	0.24	-	0.02	0.28	0.01	24.6	0.04	-	0.02	0.02	0.01	-
D3-3H5	1.91	0.24	-	0.01	0.28	-	24.5	0.05	0.04	-	0.05	0.03	0.09
D3-3H6	1.84	0.21	-	0.01	0.28	0.02	23.3	0.04	0.00	-	0.02	-	-
D3-3H7	1.80	0.16	-	0.02	0.23	0.01	21.7	0.04	0.02	-	-	0.01	-
D3-3H8	2.02	0.26	-	0.06	0.29	0.01	25.2	0.01	0.02	-	0.01	-	0.13
D3-3G1	2.14	0.65	-	0.04	0.34	0.01	45.6	0.09	0.01	-	0.06	0.17	0.01
D3-3G3	2.76	0.59	-	0.09	0.34	0.01	46.2	0.09	0.04	0.05	0.14	0.10	0.05
D3-3G4	3.14	0.54	-	0.04	0.37	-	47.1	0.09	0.03	0.04	0.08	0.07	0.01
D3-3G6	3.20	0.49	-	0.09	0.35	-	47.5	0.09	0.01	0.05	0.09	0.09	0.04
D3-3G7	2.95	0.53	-	0.07	0.38	-	47.1	0.09	0.03	0.04	0.10	0.06	0.01
D3-3G8	3.09	0.60	-	0.05	0.38	0.006	47.1	0.10	0.04	0.04	0.13	0.09	0.05
D3-3G9	3.18	0.13	-	-	0.17	-	31.8	0.03	0.00	-	0.06	0.02	-
D3-3I	1.14	0.57	0.43	0.21	0.34	-	38.6	0.10	0.04	-	0.10	0.32	0.10
D8-12A	1.42	3.11	0.58	0.10	0.28	0.042	30.9	0.12	0.00	-	0.02	0.07	0.04
D8-12B	1.42	2.78	0.57	0.08	0.30	0.050	31.3	0.26	0.04	-	0.02	0.07	0.09
D812-2	0.99	3.52	0.79	0.21	0.27	0.07	29.5	0.30	0.02	-	0.02	0.03	0.07
D812-5	1.74	3.11	0.32	0.05	0.37	0.03	37.8	0.09	0.02	-	0.02	0.10	0.12
D812-5	1.90	2.72	0.45	0.08	0.37	0.04	37.8	0.11	-	-	0.05	0.14	0.05
D812-5	1.68	2.90	0.72	0.06	0.33	0.02	37.4	0.10	0.05	-	0.01	0.08	-
D812-6	1.50	3.15	0.85	0.05	0.30	0.09	34.3	0.22	0.00	-	0.02	0.37	0.14
D812-6	1.89	3.24	1.65	0.14	0.33	0.16	36.2	0.35	0.08	-	0.03	0.39	0.26
D812-6	1.60	3.25	1.25	0.13	0.33	0.18	38.5	0.27	-	-	0.01	0.83	0.20
D812-8	1.37	3.20	0.65	0.27	0.26	0.03	30.9	0.10	0.01	-	0.01	0.03	0.10
D812-8	1.61	3.64	0.57	0.11	0.30	0.07	35.0	0.13	0.01	0.03	0.01	0.05	0.13
D812-8	1.35	3.26	0.65	0.20	0.27	0.07	31.9	0.11	0.01	-	0.02	0.09	0.01
D812-9	1.48	3.03	0.45	0.11	0.28	0.06	32.6	0.07	0.03	-	0.01	0.08	-
D812-9	1.73	3.31	0.48	0.11	0.29	0.05	34.6	0.09	0.04	-	0.02	0.05	0.05
D812-9	2.05	3.14	0.54	0.16	0.35	0.04	38.5	0.11	0.00	0.01	0.03	0.12	0.08
D812-10	1.74	3.20	1.09	0.21	0.32	0.05	35.2	0.13	0.03	0.01	0.01	0.06	-
D812-10	1.83	3.11	0.82	0.25	0.36	0.09	34.7	0.14	0.01	0.04	0.01	0.06	0.16
D812-10	1.62	2.95	1.32	0.18	0.32	0.16	31.5	0.37	0.07	-	0.01	0.07	0.05
D812-11	1.67	3.35	0.59	0.20	0.33	0.15	35.3	0.15	0.04	-	-	0.10	0.09
D812-11	1.40	3.44	1.06	0.18	0.31	0.18	33.2	0.15	0.03	0.03	0.03	0.06	0.05
D812-11	1.48	3.20	0.81	0.11	0.31	0.16	33.3	0.35	-	-	-	0.03	0.06
D812-12	1.66	3.35	0.92	0.18	0.32	0.17	33.5	0.11	-	-	0.02	0.10	0.13
D812-12	1.66	3.47	0.94	0.07	0.34	0.13	34.2	0.14	0.01	-	0.01	0.06	0.04
D812-12	1.50	3.31	1.55	0.17	0.34	0.11	34.7	0.16	0.00	-	0.01	0.10	-
D73-1C1	2.20	2.21	0.00	0.02	0.34	0.04	39.2	0.11	0.01	-	0.01	0.15	0.04
D731C3	1.67	2.32	0.45	0.03	0.77	0.04	37.1	0.31	0.04	0.02	0.02	0.31	0.02
D731C-4	1.68	3.05	0.28	0.06	0.41	0.07	38.3	0.33	0.04	0.00	0.03	0.39	0.02
D73-1C5A	1.11	3.34	5.00	0.09	0.54	0.29	26.4	3.47	0.08	0.05	-	0.33	0.00
D73-1C5B	0.70	3.56	1.99	0.03	0.27	0.57	25.9	2.83	0.14	0.03	0.01	0.22	-
D73-1CC	1.63	2.63	0.03	0.01	0.25	0.11	42.4	0.37	0.07	0.05	0.03	0.46	0.01
D73-1C5D	1.46	2.58	0.49	0.1	0.27	0.1	42.5	0.44	0.05	0.01	0.03	0.44	0.17
D73-1C5E	1.56	2.80	-	0.04	0.26	0.03	42.2	0.15	-	0.01	0.02	0.64	0.02

Table 15. Continued

	Na	Mg	Si	S	Ca	Ti	Mn	Fe	Ni	Cu	Mo	Ba	Pb
D17-1D6	2.00	2.71	0.49	0.08	0.20	0.06	40.9	0.41	0.04	0.03	0.02	0.66	0.10
D73-1C7	2.09	2.59	0.58	0.01	0.20	0.11	40.9	0.56	0.05	0.01	0.03	0.45	0.10
D73-1C8	1.96	3.00	0.75	0.07	0.21	0.06	41.0	0.28	0.02	0.01	0.01	0.36	0.04
D731C-9	1.51	3.02	0.73	0.04	0.20	0.16	34.4	0.39	-	0.02	0.04	0.35	0.04
D731C-10	1.94	2.38	0.39	0.02	0.23	0.09	42.6	0.25	0.03	-	0.05	0.37	-
D73-1C-11	1.90	3.02	0.62	0.03	0.24	0.1	39.1	0.39	0.03	0.03	0.01	0.34	0.02
D73-1C12	2.12	3.14	0.30	0.13	0.26	0.09	40.4	0.38	0.01	0.02	0.02	0.26	0.10
D72-1C-13	1.91	2.97	0.43	0.1	0.28	-	41.1	0.10	0.02	0.01	0.01	0.23	-
D73-1C-14	2.45	2.03	0.29	0.09	0.38	-	44.1	0.17	0.01	-	0.03	0.22	0.07
D73-1C-15	2.25	1.62	-	0.08	0.35	-	39.2	0.17	0.02	0.02	0.02	0.07	0.01
D73-1C-16	2.51	1.49	-	0.02	0.28	-	35.5	0.10	0.02	-	0.02	0.02	0.08
Average	1.86	2.10	0.80	0.09	0.31	0.09	34.7	0.26	0.03	0.03	0.03	0.18	0.07
Maximum	3.20	3.64	5.00	0.27	0.77	0.57	47.5	3.47	0.14	0.05	0.14	0.83	0.26
Minimum	0.70	0.13	0.00	0.00	0.17	0.01	21.7	0.01	0.00	0.00	0.01	0.01	0.00
St. Dev.	0.50	1.30	0.79	0.07	0.08	0.09	7.3	0.54	0.02	0.02	0.03	0.19	0.05

Table 12. Electron microprobe analyses of AC manganese oxides. All concentrations are in weight %. Sample numbers in left column correspond to numbers on Figures 21 through 23.

	Na	Mg	Si	S	Ca	Ti	Mn	Fe	Ni	Cu	Mo	Ba	Pb
D3-3G2	0.67	0.24	-	0.01	0.07	-	16.39	-	0.04	-	0.01	0.02	-
D8-12C	0.62	1.97	0.38	0.03	0.14	0.05	15.61	0.11	0.010	-	-	0.01	0.04
D8-12D	0.65	1.78	0.42	0.04	0.16	0.07	16.60	0.59	-	-	-	-	0.05
D8-12E	0.50	1.74	0.73	0.01	0.12	0.20	14.00	0.77	-	-	0.01	0.05	0.01
D812E2	0.50	1.61	0.60	0.02	0.12	0.25	14.14	0.60	-	-	0.01	0.09	0.04
D812-7	0.33	1.30	0.22	0.04	0.07	0.04	10.34	0.09	-	-	0.01	-	0.04
D812-7	0.29	1.21	0.31	0.02	0.08	0.06	9.49	0.14	-	-	-	-	-
D812-7	0.42	1.56	0.25	0.03	0.09	0.03	12.17	0.11	0.020	-	-	-	-
D812-13	0.40	1.71	0.25	0.01	0.11	0.05	13.29	0.15	-	-	-	-	0.01
D812-13	0.43	1.94	0.30	0.01	0.12	0.05	15.61	0.25	-	-	0.01	0.01	0.02
D812-13	0.39	1.62	0.25	-	0.12	0.05	13.78	0.37	-	-	-	-	-
D73-1C2	0.82	3.64	3.45	0.04	0.09	0.38	14.14	2.28	0.091	0.11	0.01	0.05	0.074
Average	0.5	1.69	0.65	0.02	0.11	0.11	13.8	0.497	0.040	0.11	0.01	0.038	0.035
Max	0.82	3.64	3.45	0.04	0.16	0.38	16.6	2.277	0.091	0.11	0.01	0.093	0.074
Min	0.29	0.24	0.22	0.01	0.07	0.03	9.495	0.085	0.005	0.11	0.01	0.008	0.006
Std.Dev.	0.16	0.77	0.94	0.01	0.03	0.11	2.232	0.637	0.037	-	-	0.032	0.024

analysis locations are shown in Figures 21, 22A, B and 23. Even at a low sample current of 15 nAmps, the beam burned off volatiles, as evidenced by bubbling of the carbon coating on the DPTS. An attempt to degas the Mn-oxides by leaving the DPTS in the vacuum of the microprobe overnight had little effect. The AC areas released the most volatiles, and in places the microprobe beam left a pit in the AC Mn-oxides. Microcrystalline oxides released volatiles in places, but not as commonly as AC oxides. Crystallite oxides rarely display a noticeable loss of volatiles under the beam.

Microprobe analyses were planned to evaluate chemical differences among the crystalline Mn-oxide phases and the AC phase. Analyses were run on a stratabound sample, (D3-3) (Fig. 21) and two Mn-oxide cemented sandstones (D73-1 and D8-12). Samples were chosen to provide several Mn-oxide morphologies for analysis. Sample D73-1C contains both volcaniclastic and foraminiferal sandstones (Figs. 22A, B). D8-12 has a thin stratabound Mn-oxide layer within the sandstone (Fig. 23). For a detailed description of each DPTS see Appendix IV.

Sample D3-3 has Si concentrations below the detection limit, whereas samples D73-1C and D8-12 have low, but measurable Si (Tables 11 &12). This is expected as D8-12 and D73-1C are Mn-oxide cemented sandstones and D3-3 has only minor amounts of detrital material.

AC oxides have higher amounts of Ti, Fe, and Ni than the crystalline oxides; however, abundances are still under 1%. The remaining elements are enriched in the crystalline phases. The characteristic difference between the two phases is that Mn-oxides in the crystalline phase range from 22 to 47 % whereas in the AC phase it ranges from 9 to 17 %. The large variation in measured Mn content between the two phases is probably due to greater water content and smaller particle size of the AC phase. Small particle size can create more porosity and provides charge imbalances that create a greater capacity for water absorption. Areas of high porosity and hydrous minerals create lower total counts on the microprobe and thus lower measured Mn in the AC Mn-oxides. When all elements of the microprobe analysis are totaled using their most oxidized state and normalized to a 100% on a water-free basis, the normalized manganese content (as MnO_2) of the AC areas is roughly equal to the normalized concentrations in the crystalline areas.

Plots of electron microprobe-measured concentrations of Mg, Ca, and Na versus Mn are presented in Figures 24, 25, and 26. In general, Mg, Ca, and Na increase in concentration with increasing crystallinity. D3-3 crystalline oxides always plot in two groups; the microcrystalline areas are lower in Mn and generally lower in Ca, Mg, and Na than the crystallite areas. The highest Na values are from the crystallites of D3-3. The high Na / Mn ratios of all analyzed D3-3 Mn-oxides indicate mineral-seawater exchange.

A Mg versus Mn plot (Fig. 25) illustrates that D3-3 is lower in Mg than either of the other samples studied. Generally, low Mg is indicative of a proximal hydrothermal deposit. Magnesium is removed readily from hydrothermal fluids during alteration of arc rocks creating Mg silicates (usually clay minerals), thus removing Mg from solution. Mg is enriched in more distal deposits when hydrothermal fluids mix with pore water or seawater (Mottl, 1983). Thus, D3-3 may have been formed closer to the source of the hydrothermal fluids than either D8-12 or D73-1C.

In general the Ca versus Mn plot (Fig. 26) shows a similar trend of increasing concentration with increasing crystallinity. D73-1C has two high Ca values (15 and 16) with the respective probe positions shown on Figure 22B. The sample locations with the high Ca values are in a Mn-oxide cemented foraminiferal sandstone (Fig. 27A) indicates that high Ca values may be due to dissolution of foraminiferal tests.

Elemental concentrations can be indicators of differing conditions during Mn-oxide mineralization. Low Mg content appears to indicate deposition proximal to the hydrothermal source. High Na appears to indicate seafloor or near seafloor deposition. Calcium values probably denote higher availability of calcium within the sediment column, i.e. from foraminiferal sandstones. However, high Na and Ca may also reflect post depositional exposure to seawater and subsequent concentration of these elements by absorption.

DISCUSSION

Model of mineralization

Active volcanic arcs are the hosts for many ore deposit types such as porphyry deposits, skarn deposits, massive sulfide deposits, and many others (Sawkins, 1990). Manganese-oxide mineralization of the Mariana Arc may be produced in several ways. The deposits may be produced epithermally, by low temperature, generally shallow, hydrothermal convection cells within the sedimentary column. Alternatively, these deposits may be the low-temperature, distal precipitates of large hydrothermal systems that deposit sulfides at depth. Each system can produce similar manganiferous deposits and both are quite likely to occur around active submarine volcanos. The chemical variations found in trace elements of these Mn-oxide deposits such as Mo and Zn may relate to depth (or size) of the hydrothermal system.

Sample morphology indicates that the initial stage of mineralization is cementation of sediments by the Mn-oxides. As precipitation continues and porosity of the sediments decreases, the movement of mineralizing fluids becomes confined to fractures and other zones of less resistance within the sediments (such as bedding planes). The concentration of mineralizing fluids along zones of less resistance leads to the precipitation of the thicker stratabound layers within the Mn-oxide cemented sediment.

Generally, Mn-oxide cemented sediments and stratabound Mn-oxides become younger beneath the seafloor/sediment interface (Usui, 1989). The cementation of the sediments first begins near the seafloor/sediment interface. The ascending Mn-rich hydrothermal solutions interact with oxygenated interstitial waters and precipitate Mn-oxides. As the porosity decreases the precipitation occurs deeper in the sediment column creating younger Mn-oxides beneath older ones. This simple model does not explain completely the variety

of cementation textures recovered from the Mariana Arc, but is probably valid as a first approximation.

Although we have no direct evidence of mounds in these areas their existence is postulated from the nature of the samples recovered. Based on the morphology and lithologic associations, stratabound Mn-oxide deposits such as those recovered in dredges 3, 20, and 28 probably formed as the ascending mineralizing fluids arrived at seawater/sediment interface. Hydrothermal muds and associated stratabound Mn-oxides were deposited around the hydrothermal vents forming mound type deposits. Hydrothermal muds were not recovered in great quantities as they wash off the samples when the dredge is brought up through the water column. These deposits are probably similar to Galapagos mounds Mn-oxide deposits. Honnorez et al. (1981) provided a geochemical model Galapagos mound formation that maybe a likely analog of mound formation in the Mariana Islands Arc.

Moore and Vogt (1976) described Mn-oxide deposits from the Galapagos spreading axis with a morphology similar to the stratabound deposits of D3, D20, and D28. These spreading center Mn-oxides also have a similar chemistry to the Mariana Island Arc hydrothermal stratabound Mn-oxides. The processes that creates these low-temperature Mn-oxides deposits do not appear to be limited to one tectonic setting. Similar Mn-oxide deposits have been described adjacent to a submarine fissure offshore of the island of Hawaii (Clague, Schulz, and Hein, unpublished data). We expect additional deposits of this type to exist in other active volcanic systems that will undoubtably be reported as the ocean basins are further explored and sampled.

Further work on this type of hydrothermal Mn-oxides is needed to answer several important questions: What is the specific nature of the amorphous to cryptocrystalline oxides? How do the 10 Å phases relate to the minerals todorokite and buserite? What do the Mn-oxide mineral textures reveal about the chemistry of the mineralizing fluids? In what temperature range is the Mn-oxide deposited? And, what are the stratigraphic and structural relations of the Mn-oxide deposits.

Possible preservation in the geologic record and on-land analogs

The preservation potential of an undissected oceanic volcanic arc is poor. Volcanic arcs can be obducted, subducted, or accreted during closure of back-arc basins or collision of arcs and continents. If tectonic processes do not significantly obliterate the volcaniclastic sedimentary sequence and Mn-oxide accumulations of the arc, then degradational processes (erosion, mass wasting, slumping, etc.) probably will. Furthermore, Hein et al. (1991) showed that stratabound Mn-oxides are significantly altered during uplift and supergene alteration of deposits within the Tonga Arc.

The lateral extent and depth of the Mariana Island Arc deposits is unknown. Although Mn-oxides were recovered along the length of the island arc, the individual deposit maybe fairly small. In addition, later sedimentation above the Mn-oxides can produce redox conditions that remobilize manganese. The Mn-oxide deposits will degrade when pore waters become consistently reducing.

Although the preservation potential for these deposits is not high, the best areas to look for fossil analogs are dissected arcs where vertical exposures of sedimentary sections are good, undissected arcs, and accreted terranes. Likely fossil analogs of Mariana Mn-oxide deposits are: Philippines, Todoro district Hokkaido, Japan; and Mn-oxide deposits of Eua and Tonumea Islands,Tonga (Hein et al., 1991).

Sorem (1956) states that occurrences of manganese are known on practically every large island and on many small islands of the Philippines. Many of these deposits are of such a small extent or of such low grade that large scale mining is not possible. Lewis et al. (1982) interpreted the rocks of the eastern Philippines as an Early Tertiary island arc. Many of the small Mn-oxide deposits of the Philippines may be analogous to those we've described here from the modern Mariana Islands Arc.

CONCLUSIONS

Manganese oxide mineralization has been investigated at several locations in the Mariana Arc. Mineralization is characterized by Mn-oxide-cemented sediments and stratabound layers of Mn-oxides. X-ray diffraction shows that two Mn-oxide phases are present: a 10 Å phase (todorokite and / or buserite) and a 7 Å phase (birnessite). The 10Å phase collapses to a 7Å phase in many samples on exposure to air.

Microscopic textures of the Mn-oxide minerals are defined by morphology and crystallite size. Morphological types include: colloform, homogeneous dense (without pore space), laminated dense layers, porous fibrous, and scaly. Crystallite sizes include: amorphous to cryptocrystalline (AC), microcrystalline, and crystallites. The AC oxides have very high water contents as shown by SEM and electron microprobe studies.

Chemical analyses of the the hydrothermal Mn-oxides show manganese concentrations as high as 48% in stratabound deposits, with an average of 42%. Molybdenum, Zn, and Cd are concentrated in the deposits and are thought to be hydrothermal in origin. Cobalt and Ce in some of the hydrothermal Mn-oxides are concentrated by adsorption from seawater.

ACKNOWLEDGMENTS

We would like to thank Robert Stern, University of Texas at Dallas, and Sherman Bloomer, Brown University, for the opportunity to collect these samples; Lou Calk, U.S. Geological Survey, for his patience and great help with the electron microprobe analyses; Robert Oscarson, U.S. Geological Survey, for SEM support; and Herb Kirchenbaum, U.S. Geological Survey, for the ICP analyses. We thank Randoph Koski, U.S. Geological Survey, for discussions throughout this study and for a helpful review of this report.

REFERENCES

Albee, A.L. and Ray, L., 1970, Correction factors for electron-probe microanalysis of silicates, oxides, carbonates, phosphates and sulfates. Analytical Chemistry, v. 42, p. 1408-1414.

Arrhenius, and Tsai, 1981, Structure, phase transformation, and prebiotic catalysis in marine manganate minerals. Scripps Institute of Oceanography Reference Series 81: p. 1-19.

Bloomer, S. H., Stern, R.J., and Smoot, N. C., 1989a, Physical volcanology of the submarine Mariana and Volcano Arcs. Bulletin of Volcanology, v. 51, p. 210-224.

Bloomer S. H., Stern, R. J., Fisk, E., and Geschwind, C. H., 1989b, Shoshonitic volcanism in the northern Mariana Arc: 1. mineralogic and major and trace element characteristics. Journal of Geophysical Research, v. 94, n. B4, p. 4469-4496.

Bruland, K.W., 1983, Trace elements in seawater. In Riley, J.P., and Chester, R., editors, Chemical Oceanography, v.8, London Academic Press, p. 157-220.

Burns, R. G., and Burns, V. M., 1977, Mineralogy. in Glasby, G. P., editor, Marine Manganese Deposits: v. 15 Elsevier Oceanography Series, New York, Elsevier, p. 185-248.

Burns, R. G., Burns, V. M., and Stockman, H. W., 1983, A review of the todorokite-buserite problem: implications to the mineralogy of marine manganese nodules. American Mineralogist, v. 68, p. 972-980.

Burns, R. G., Burns, V. M., and Stockman, H. W., 1985, The todorokite-buserite problem: further considerations. American Mineralogist, v. 70, p. 205-208.

Chase, T.E., and Menard, H.W. (compilers), 1973, Bathymetric atlas of the North Pacific Ocean. U.S. Naval Oceanographic Office, Washington D.C., Publ. No. 1301-2-3.

Clague, D. A., Schulz, M. S., and Hein, J. R., 1989, Unpublished data from U.S. Geological Survey Cruises F2-88-HW and F11-88-HW.

Cronan, D. S., Glasby, G. P., Moorby, S. A., Thomson, J., Knedler, K. E., and McDougall, J. C., 1982, A submarine hydrothermal manganese deposit from the south-west Pacific island arc. Nature, v. 298, n. 5873, p. 456-458.

Davis, A. S., Clague, D. A., Schulz, M. S., and Hein, J. R., 1991, Low sulfur content in submarine lavas: An unreliable indicator of subaerial eruption. Geology, v. 19, p. 750-753.

Dickinson, W. R., Beard, L. S., Brakenridge, G. R., Erjavec, J. L., Ferguson, R. C., Inman, K. F., Knepp, R. A., Lindberg, F. A., and Ryberg, P. T., 1983, Provenance of North American Phanerozoic sandstones in relation to tectonic setting. Geological Society of America Bulletin. v. 94, p. 222-235.

Fleet, A. J., 1983, Hydrothermal and hydrogenous ferro-manganese deposits: Do they form a continuum? The rare earth evidence,.In Rona, P. A., Bostrom, K., Loubier, L., and Smith, K. L., editors, Hydrothermal Processes at Seafloor Spreading Centers. NATO Conference Series: New York, Plenum Press, v. 12, p. 535-555.

Giovanoli, R. 1985, A review of the todorokite-buserite problem: implications to the mineralogy of marine manganese nodules: discussion. American Mineralogist, v. 70, p. 202-204.

Govett, G. J. S., 1983, Rock geochemistry in mineral exploration. In Govett, G. J. S., editor, Handbook of Exploration Geochemistry: New York, Elsevier Scientific Publishing, v. Vol. 3,

Guilbert, J. M., and Park, C. F., 1986, The Geology of Ore Deposits. New York, W. H. Freeman and Company,

Hein, J.R., Schulz, M. S., and Kang, J.K., 1991, Insular and submarine ferromanganese mineralization of the Tonga-Lau region. Marine Mining, v. 9, no.3 , p. 305-354.

Hein, J. R., Schulz, M.S., and Gein, L.A., 1990, Central Pacific cobalt-rich ferromanganese crusts: historical perspective and regional variability. In Keating, B. and Bolton, B., editors, Geology and offshore mineral resources of the central Pacific basin. Circum-Pacific Council for Energy and Mineral Resources, Earth Science Series v. 15, p. 261-283.

Hein, J. R., Schwab, W. C., and Davis, A. S., 1988, Cobalt- and platinum-rich ferromanganese crusts and associated substrate rocks from the Marshall Islands. Marine Geology, v. 78, p. pp. 255-283.

Hein, J. R., Fleishman, C. L., Morgenson, L. A., Bloomer, S. H., and Stern, R. J., 1987, Submarine ferromanganese deposits from the Mariana and Volcano volcanic arcs, west Pacific. U.S. Geological Survey Open File Report 87-281.

Honnorez, J., Von Herzen, R.P., Barrett, T.J., Becker, K., Bender, M.L., Borella, P.E., Hubberten, H-W., Jones, S.C., Karato, S., Laverne, C., Levi, S., Migdisov, A.A., Moorby, S.A., Schrader, E. L., Hydrothermal mounds and young ocean crust of the Galapagos: Preliminary Deep Sea Drilling results, Leg 70. Geological Society of America Bulletin, Part I, v. 92, p. 457-472.

Hussong, D. M., and Uyeda, S., 1982, Tectonic processes and the history of the Mariana Arc: A synthesis of the results of deep sea drilling project Leg 60. In Hussong, Donald M. and others, editors, Initial Reports of the Deep Sea Drilling Project, Leg 60: Washington D.C., U.S. Government Printing Office, v. 60, p. 909-929.

Kang, J.-K., and Hein, J.R., 1988, Textural characteristics of hydrogenetic and hydrothermal Fe-Mn crusts. EOS, Transactions of the American Geophysical Union, v.69, p. 1271.

Kang, J.-K. and Kosakevitch, A., 1984, Etude textural des encroutements ferro-manganesiferes de l'est Caraibe. Orleans, France, Bureau de Recherches Geologiques et Minieres, Service Geologique National.

Kirchenbaum, H., Manheim, F. T., Aruscavage, P. J., and Lane-Bostwick, C. M., 1989, Chemical Analysis of Ocean Floor Manganese Crusts. In Schindler, K. S., editor: Research on Mineral Resources 1989 Program and Abstracts. 5th Annual V.E. McKelvey Forum: U.S. Geological Survey Circular 1035, p. 39-40.

Koski, R. A., Hein, J. R., Bouse, R. M., and Sliney, R. E., 1985, Composition and origin of ferrromanganese crusts from Tonga Platform, Southwest Pacific. In Scholl, D. W., and Vallier, T. L., editors, Geology and offshore resources of Pacific Island Arcs Lau-Tonga Region: Houston, Texas, Circum-Pacific Council for Energy and Mineral Resources, Vol. 2, p. 179-186.

Lewis, S. D., Hayes, D. E., and Mrozowski, C. L., 1982, The origin of the West Philippine Basin by inter-arc spreading. In Balce, G. R., and Zanoria, A. S., editors, Geology and tectonics of the Luzon-Marianas region: Philippine SEATAR Committee Special Publication No. 1, p. 31-51.

Lin, P.-N., Stern, R. J., and Bloomer, S. H., 1989, Shoshonitic volcanism in the northern Mariana Arc: 2. large-ion lithophile and rare earth element abundances: evidence for the source of incompatible element enrichments in intraoceanic arcs. Journal of Geophysical Research, v. 94, p. 4497-4514.

Moorby, S. A., Cronan, D. S., and Glasby, G. P., 1984, Geochemistry of hydrothermal Mn-oxide deposits from the S.W. Pacific island arc. Geochimica et Cosmochimica Acta, v. 48, p. 433-441.

Moore, J. G., and Schilling, J.-G., 1973, Vesicles, water, and sulfur in Reykjanes Ridge basalts. Contributions in Mineralogy and Petrology, v. 41, p. 105-118.

Moore, W. S., and Vogt, P. R., 1976, Hydrothermal manganese crusts from two sites near the Galapagos spreading axis. Earth and Planetary Science Letters, v. 29, p. 349-356.

Mottl, M. J., 1983, Metabasalts, axial hot springs, and the structure of hydrothermal systems at mid-ocean ridges. Geological Society of America Bulletin, v. 94, p. 161-180.

Ostwald, J., and Dubrawski, J.V., 1987, An X-ray diffraction investigation of a Marine 10Å manganate. Mineralogical Magazine, v.51, p. 463-466.

Sawkins, F. J., 1990, Metal Deposits and Their Relation to Plate Tectonics. Second Edition: Springer-Verlag, New York.

Scott, R. B., Rona, P. A., McGregor, B. A., and Scott, M. R., September 27, 1974, The TAG Hydrothermal Field. Nature, v. 251.

Sorem, R. K., 1956, Geology of three major manganese districts of the Philippines. Proceedings of the Pacific Science Congress, v. II-A, p. 661-668.

Turner, S., Siegel, M. D., and Buseck, P. R., 1982, Structural features of todorokite intergrowths in manganese nodules. Nature, v. 296, p.841-843.

Usui, A., Mellin, T. A., Nohara, M., and Yuasa, M., 1989, Structural stability of marine 10 Å manganates from the Ogasawara (Bonin) Arc: implication for low-temperature hydrothermal activity. Marine Geology, v. 86, p. 41-56.

Usui, A., Yuasa, M., Yokota, S., Nohara, M., Nishimura, A., and Murakami, F., 1986, Submarine hydrothermal manganese deposits from the Ogasawara (Bonin) Arc, off the Japan Islands. Marine Geology, v. 73, p. 311-322.

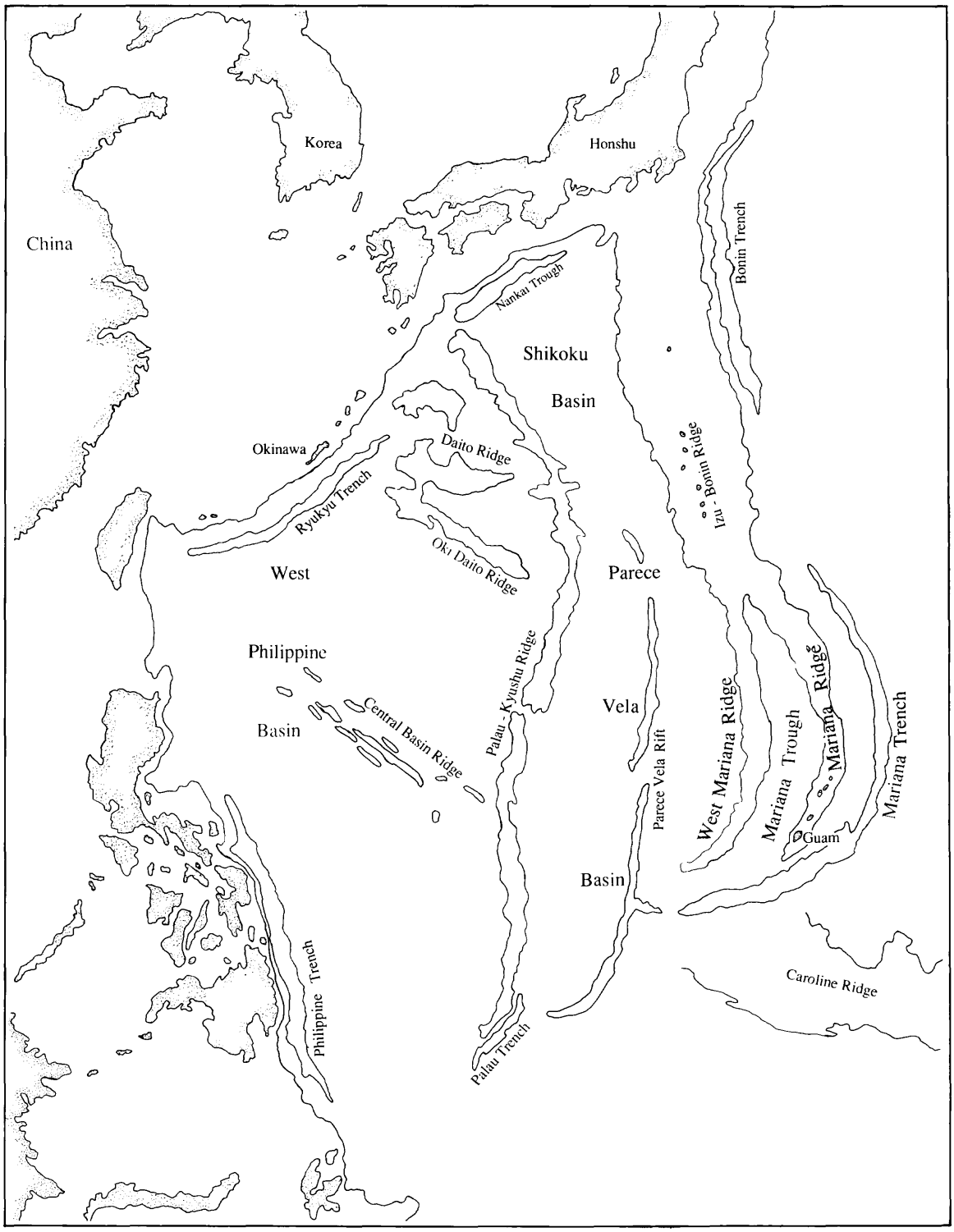

Figure 1. Map of the west Pacific with location of physiographic features, after Hussong and Uyeda (1982). The samples of this study are from the Mariana Ridge.

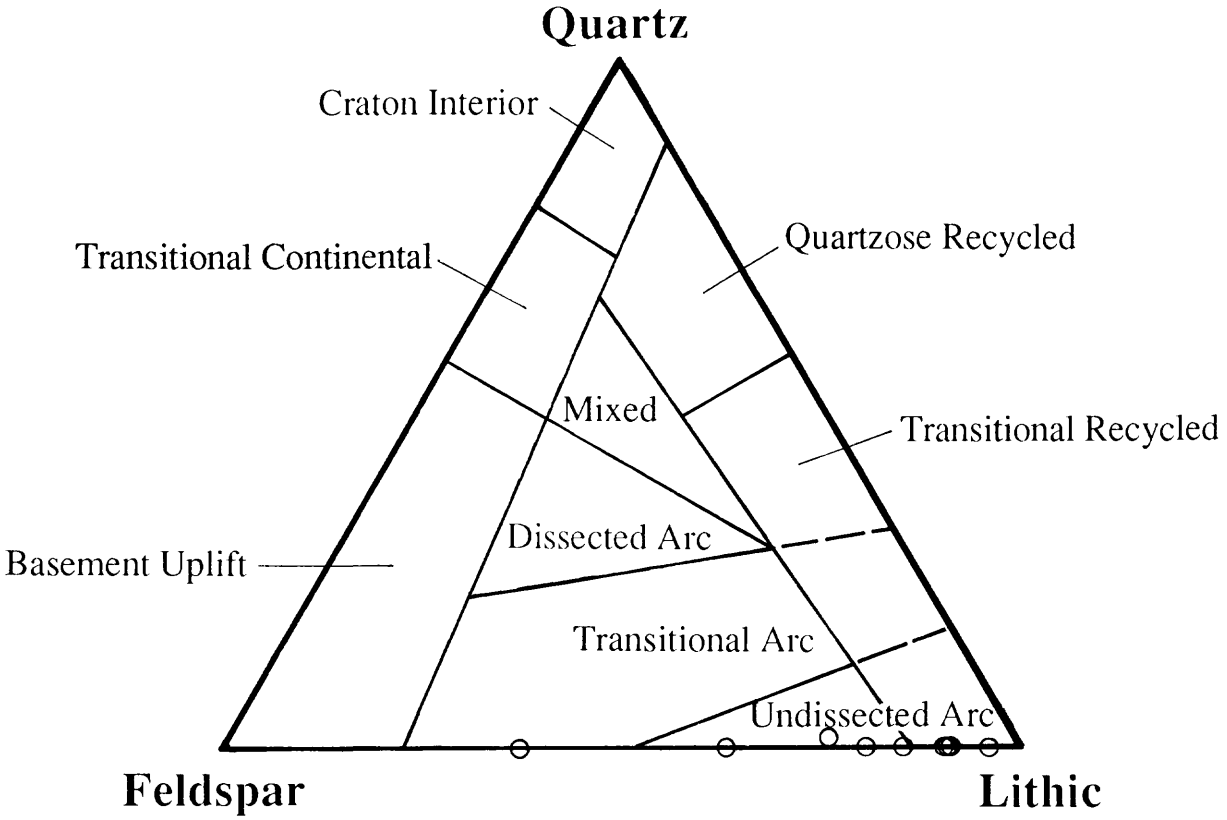

Figure 2. Point counted samples plotted on a ternary diagram with provenance fields of Dickinson et al. (1983).

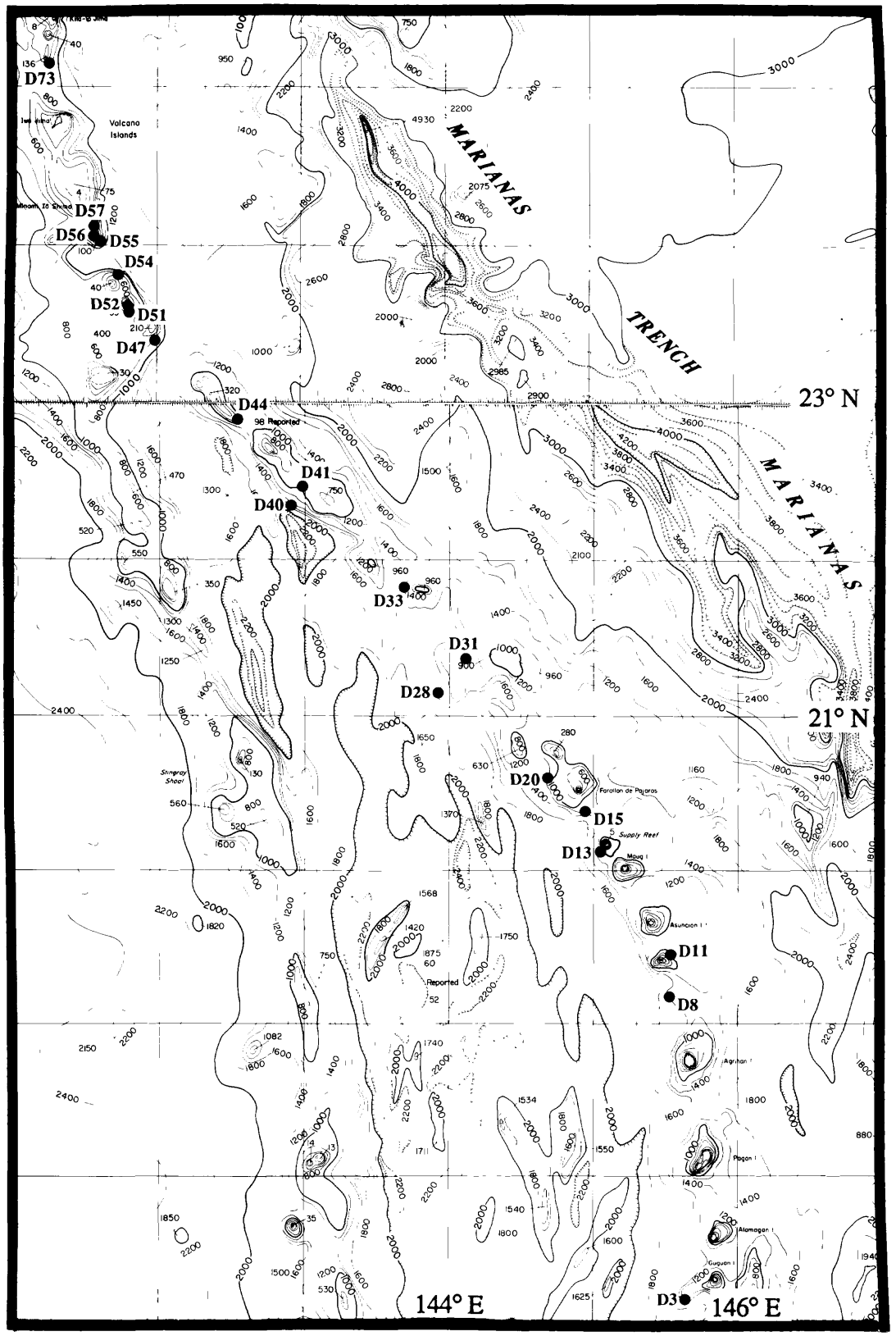

Figure 3. Bathymetric map of the Mariana Arc and Trench showing dredge locations (From Chase and Menard, 1973).

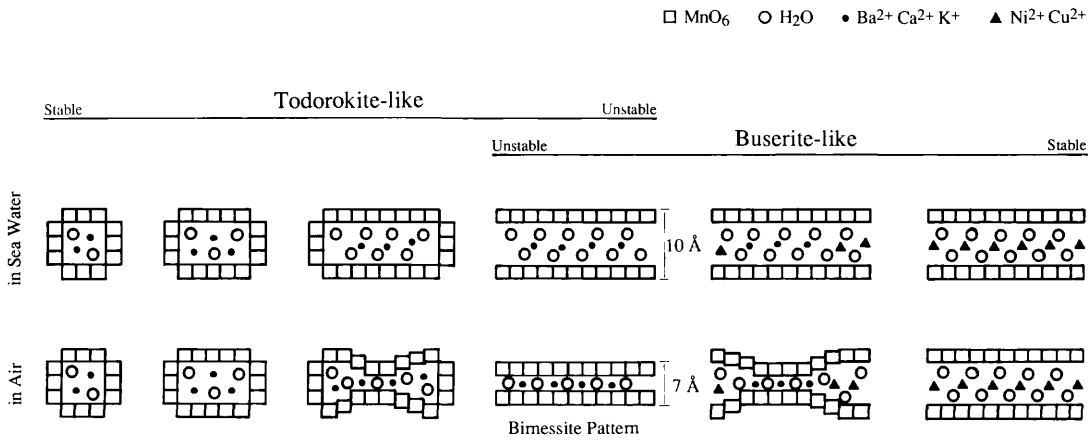

Figure 4. Collapse of 10 Å phase Mn-oxide to 7 Å phase Mn-oxide showing increased stability with increasing cations (after Usui et al., 1989).

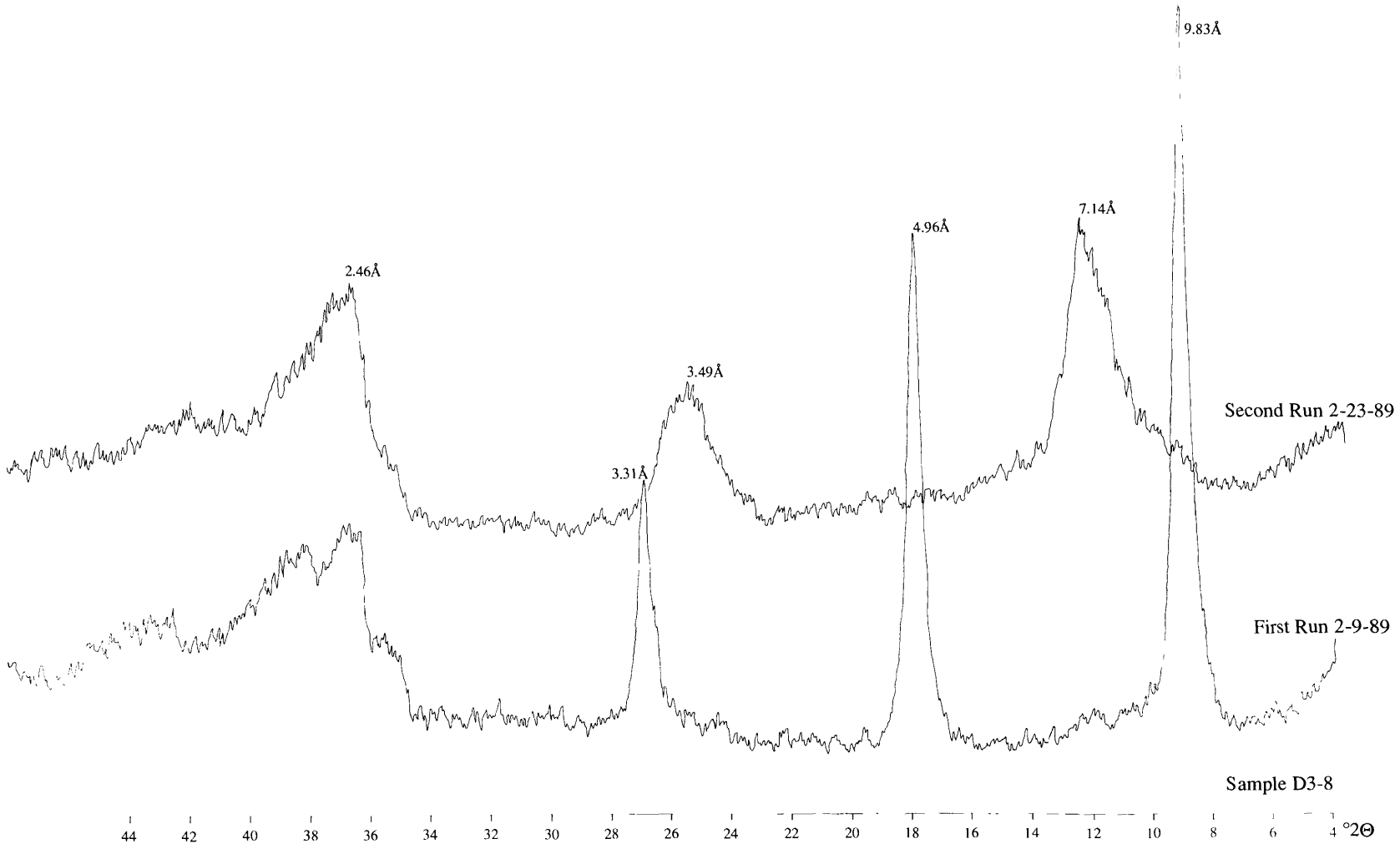

Figure 5. X-ray diffractograms of sample number D3-8 documenting complete transformation of the 10 Å phase to the 7 Å phase on exposure to air over a period of 2 weeks.

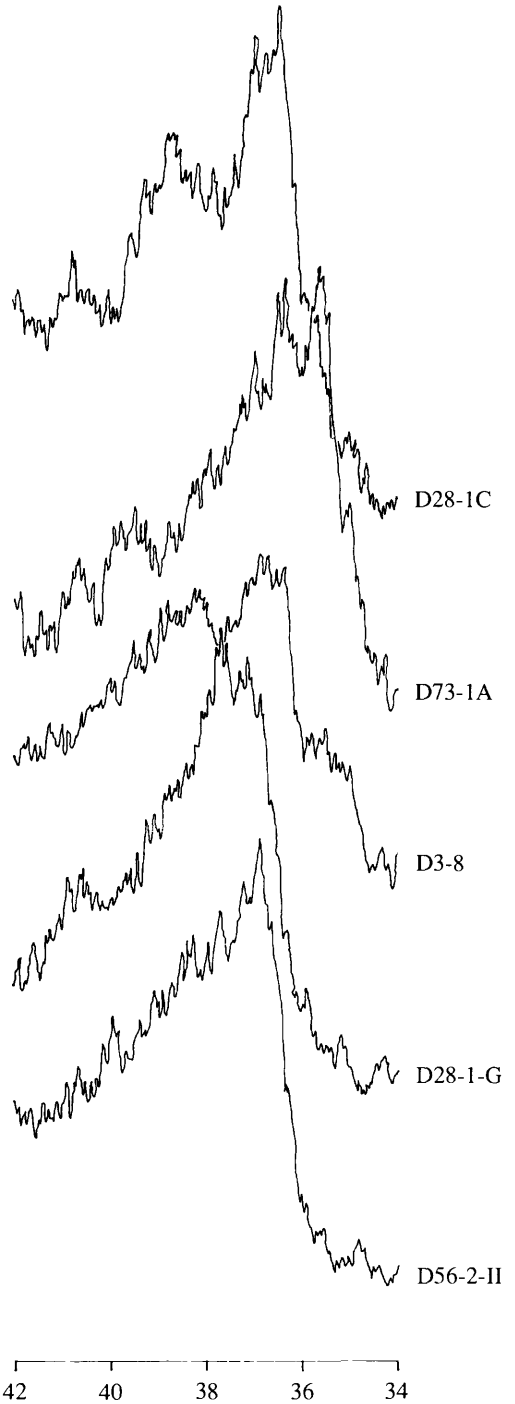

Figure 6. Comparison of X-ray diffraction peaks at 36° 2θ. D73-1A, D28-1C, and D3-8 have double peaks. Note the shifting of the peak location from ~35 ° to ~37° 2θ. Relationship of these changes to the crystallography and mineralogy of Mn- oxide phases present has yet to be determined.

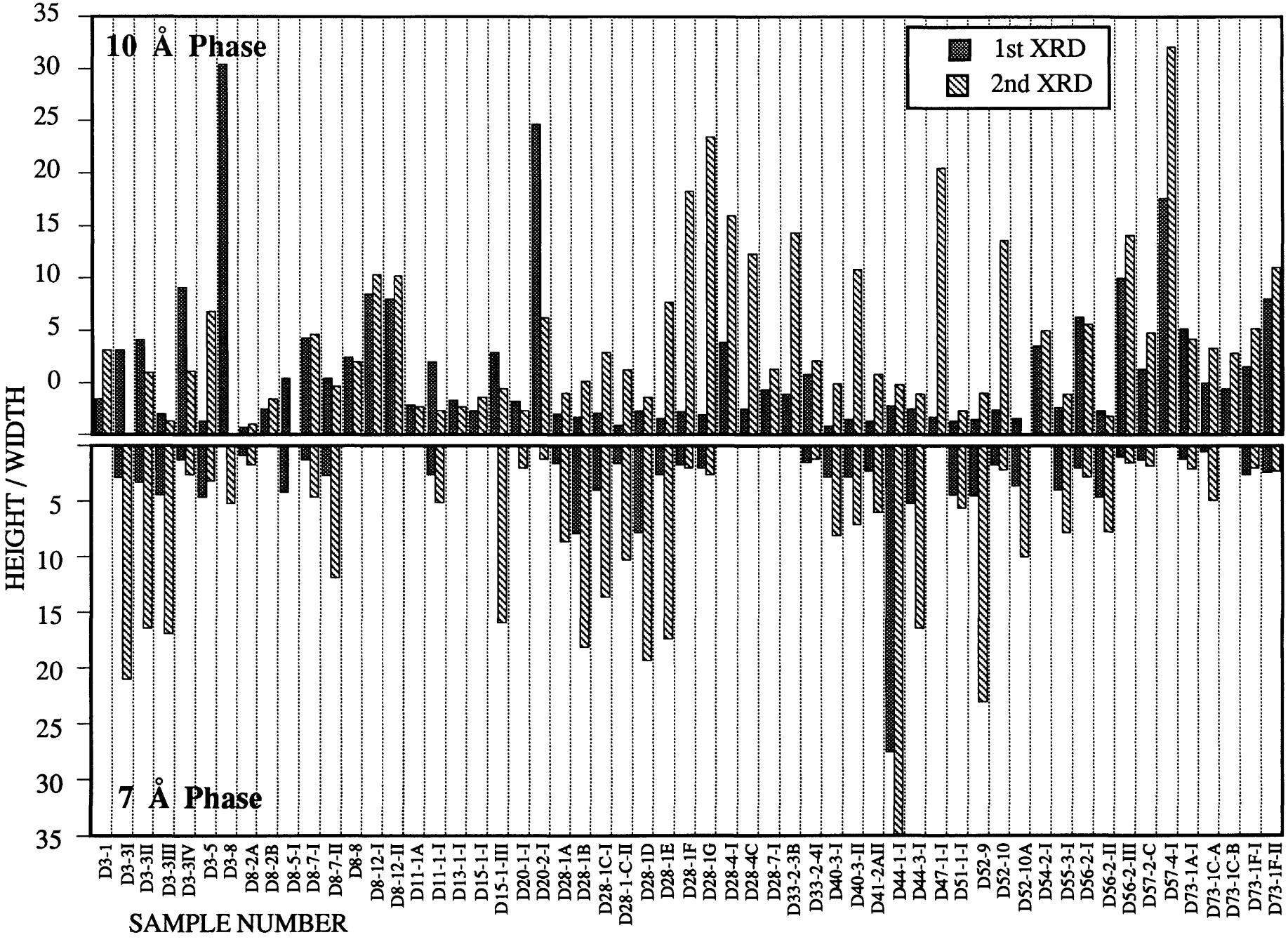

Figure 7. Bar graph of the crystallinity index (X-ray peak width at half height) in Appendix 2. Samples D3-3I, D3-8, completely transformed to a 7Å phase.

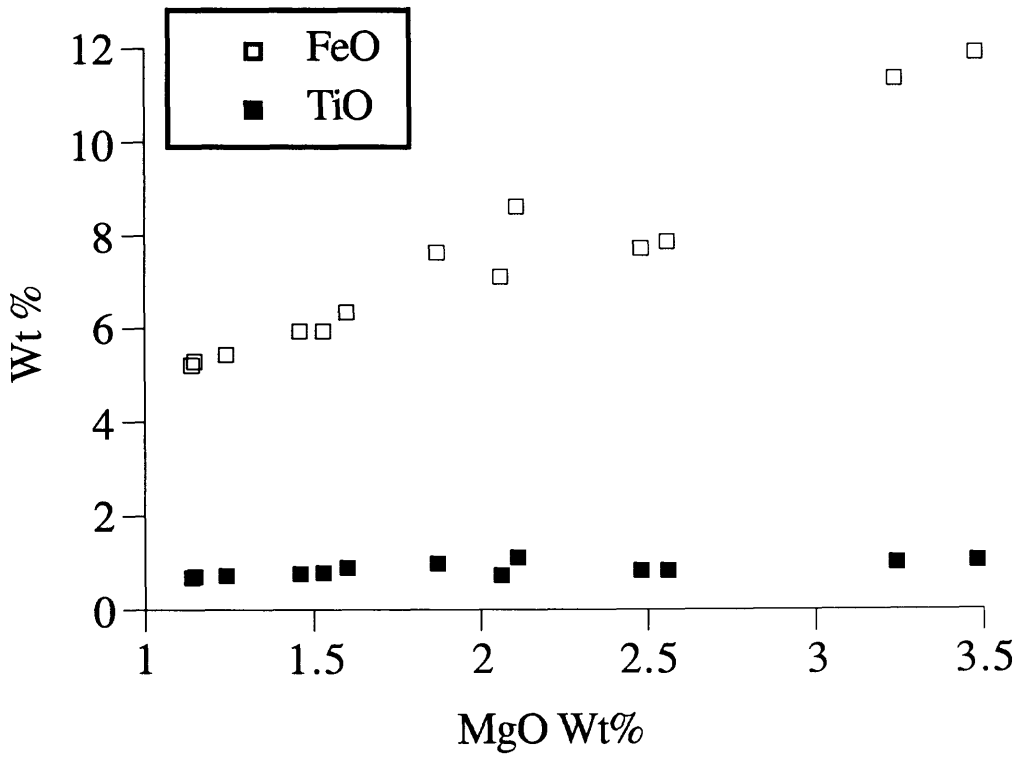

Figure 8. Scatter plot of electron microprobe chemistry of volcanic glasses from sandstones D73-1D and D73-1A. The linear trends of FeO and TiO relative to MgO are related to the fractionation of the parent magma over time. These glass fragments are from the same parental magma, but have erupted over time (fractionated). The clastic debris from successive eruptions have been deposited together.

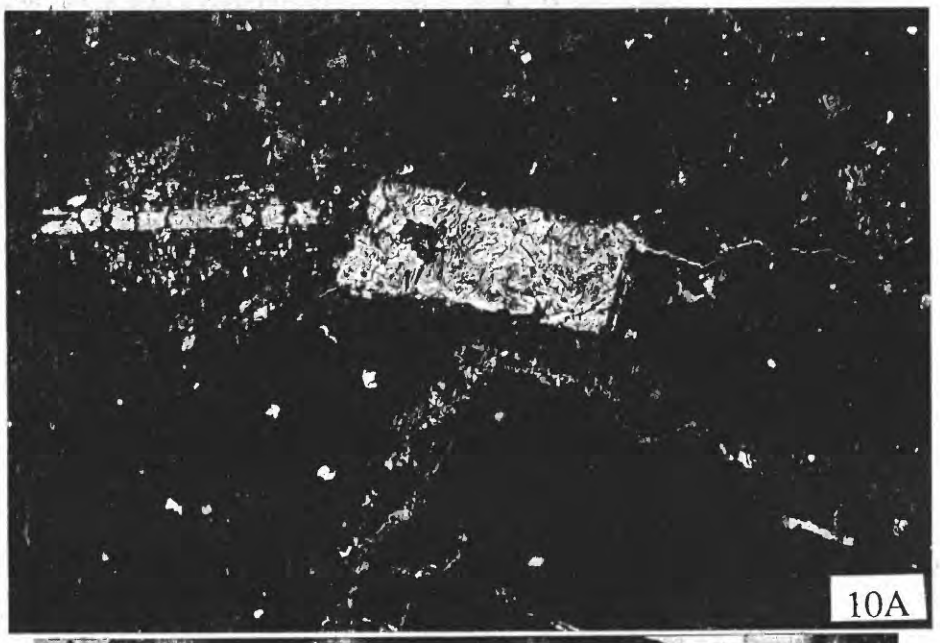

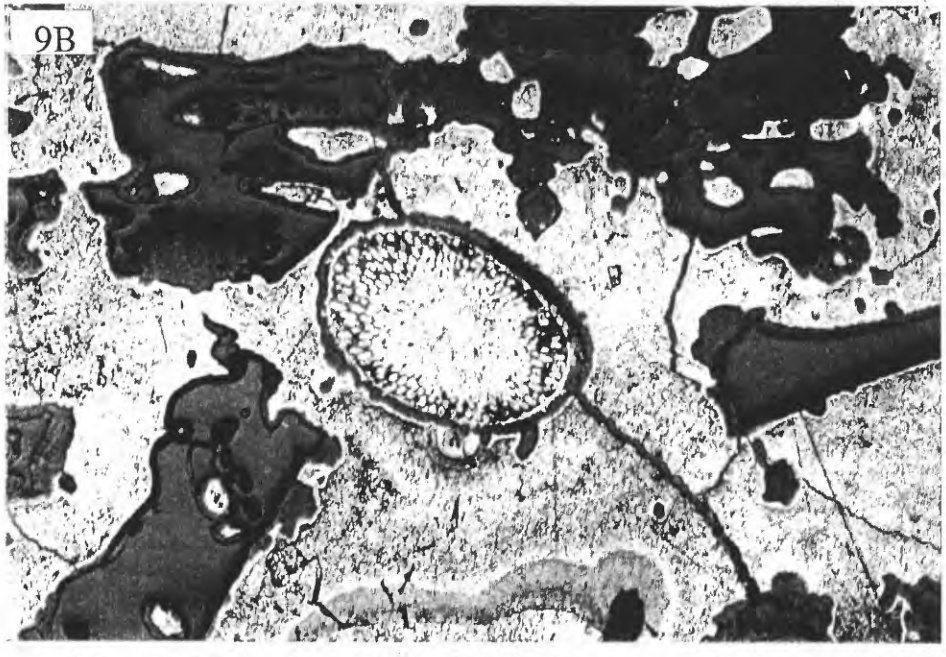

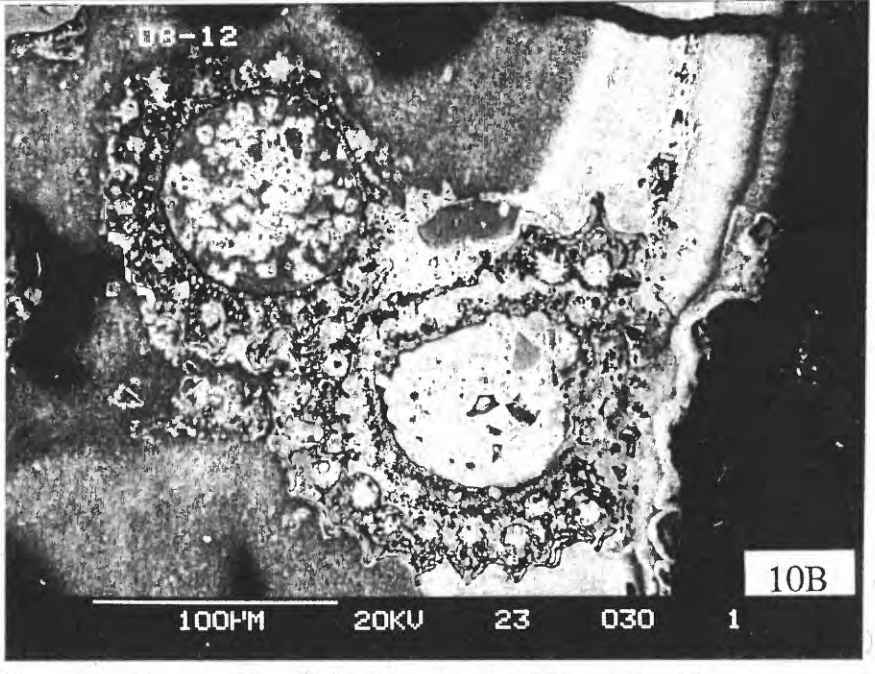

Figure 9. Photomicrographs of Mn-oxide-cemented sandstone D73-1D illustrating the coating of clastic grains by Mn-oxides (short dimension represents 360μm). At the center is a radiolarian completed coated by Mn-oxides. Other clasts are unaltered glass fragments that transmit light in spots because of Mn-oxide coatings. Cementing Mn-oxides are microcrystalline to crystalline with a colloform structure of AC Mn-oxides at the bottom center. **A.** is reflected and transmitted light, **B** is reflected light.

Figure 10 **A.** Photomicrograph of a pyroxene grain replaced by Mn-oxides, within an altered volcanic rock fragment from sample D33-2-3. Short dimension of the photograph represents 715 μm. **B.** SEM photomicrograph with backscattered electron imaging of a partly replaced foraminifera of polished section D8-12. This foraminifera is located in a stratabound layer of Mn-oxides. Note that the Mn-oxides have penetrated the foraminiferal test. Calcite may still be present in several areas, but is highly etched.

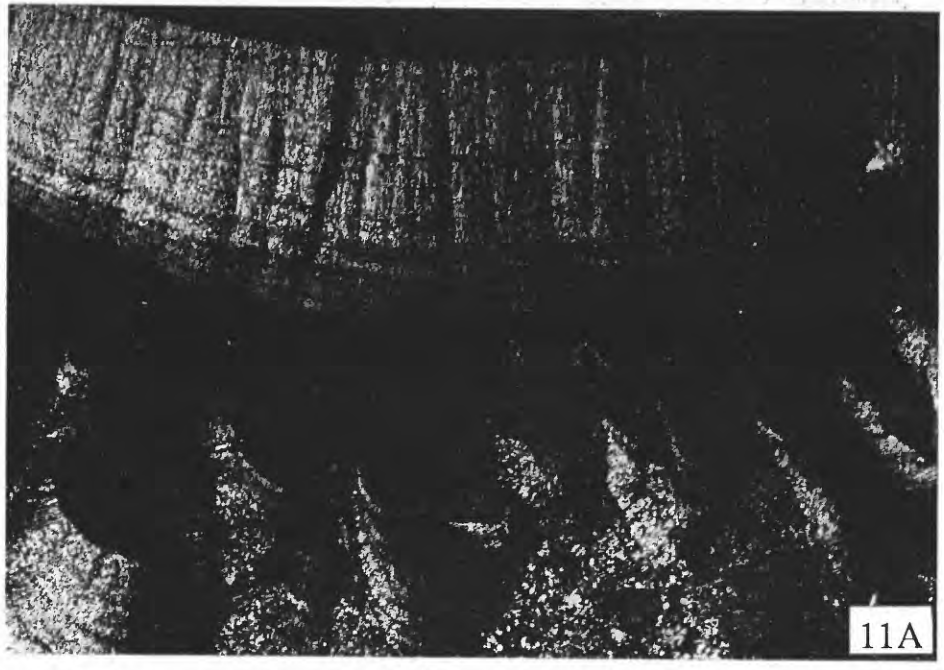

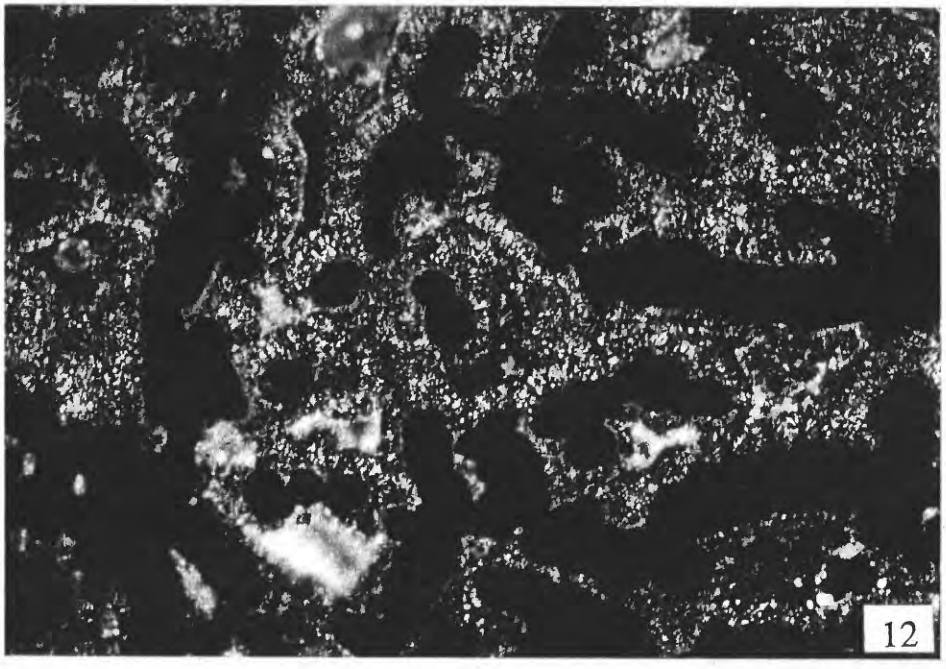

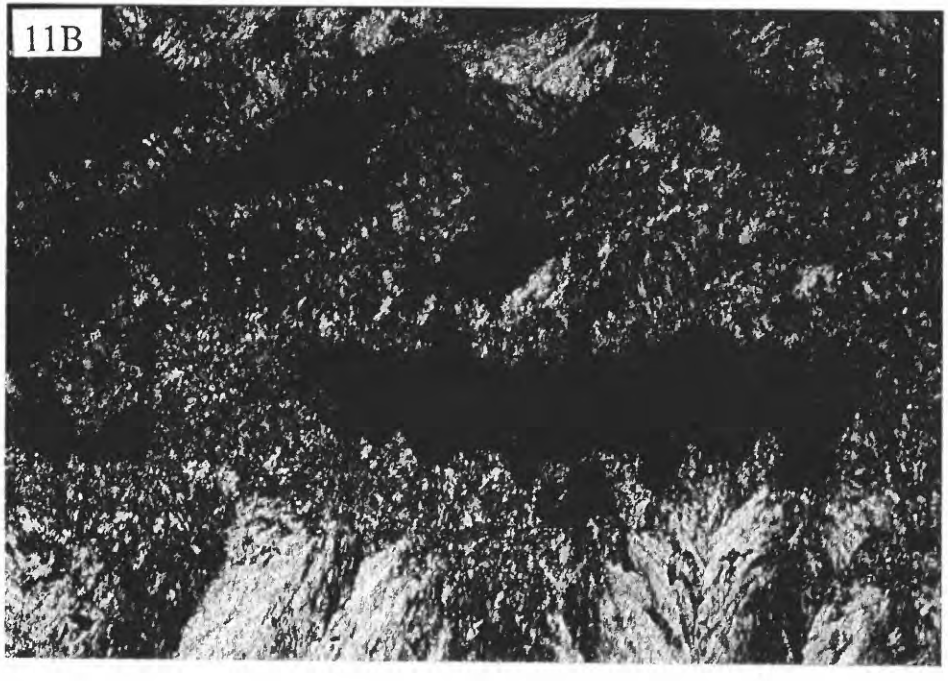

Figure 11 **A**. Photomicrograph of D28-2 illustrating a layer of aligned crystallites with botryoidal colloform AC oxides below. As mineralization continued botryoids of AC oxides were overgrown by radially aligned crystallites. The textural change reflects a changing environment, and/or a waxing and waning of mineralizing fluids. Growth orientation is into the sediment away from the seafloor. Short dimension of the photograph represents 715μm. **B**. Photomicrograph of mosaicked crystallites from sample D3-3. Crystallites are nucleating on AC cores. The top of photo has larger radially aligned crystallites. Short distance on the photograph represents 360μm.

Figure 12. Photomicrograph of crystallites and microcrystalline Mn-oxides around cores and fibers of AC oxides (sample D28-6). Short distance on the photograph represents 360μm.

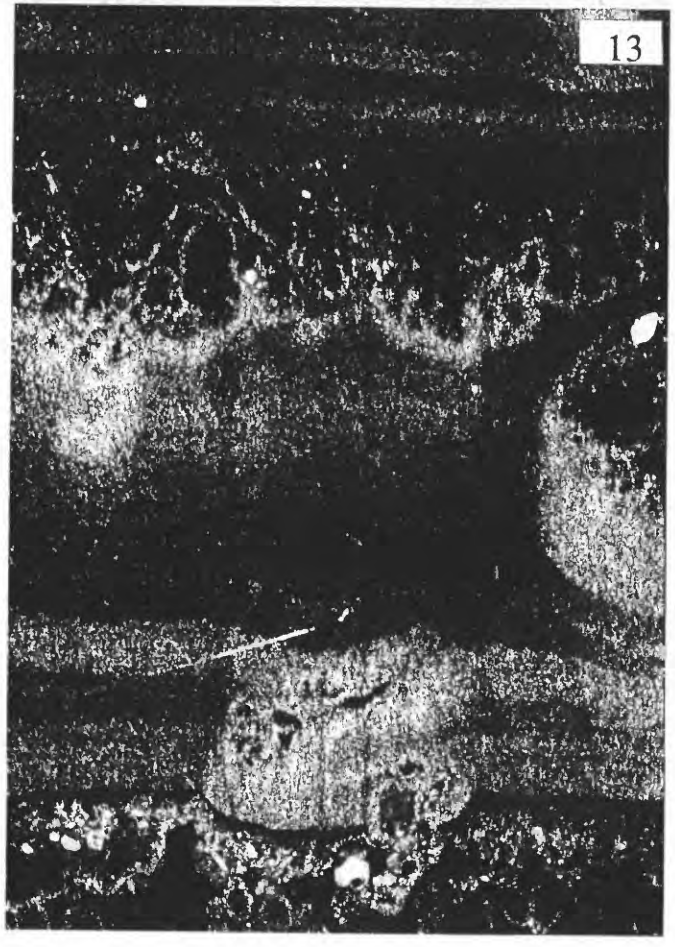

Figure 13. Photomicrograph of alternating layers of botryoidal colloform and laminated dense Mn-oxides in polarized reflected light (sample D20-1). Laminae are alternating aligned crystallites and microcrystalline Mn-oxides. Colloform textures are AC Mn-oxides Short dimension of the photograph represents 716 μm.

Figure 14. Photomicrograph of alternating porous fibrous layers and dense laminae (D3-3); in reflected and transmitted light. Short dimension of the photograph represents 715 μm.

Figure 15. Photomicrograph of scaly texture (sample D28-2). Short dimension of the photograph represents 715 μm.

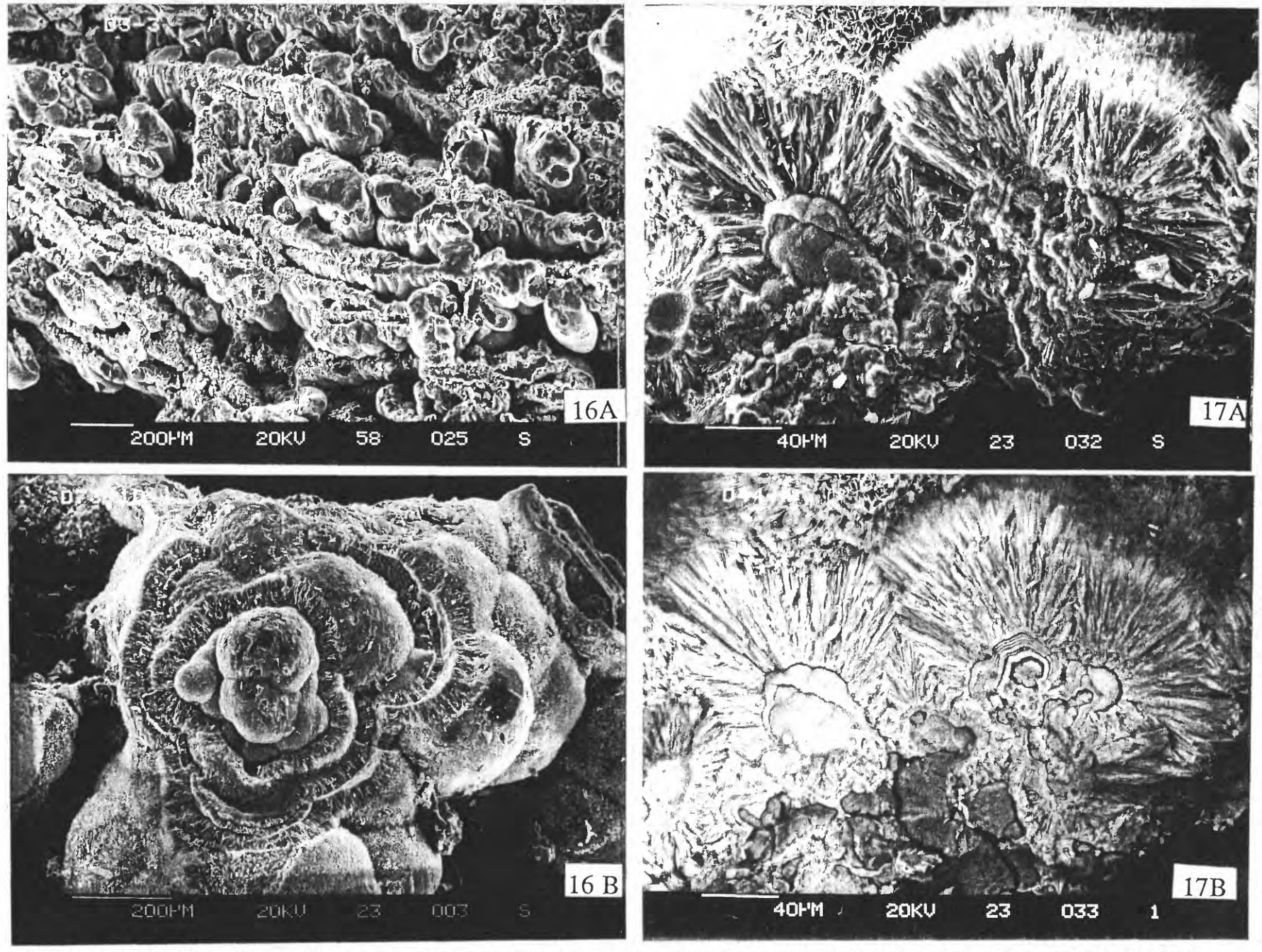

Figure 16 **A.** SEM photomicrograph of porous fibrous texture from a fracture surface of D3-3. **B.** SEM photomicrograph of colloform texture from a fracture surface of D73-1D.

Figure 17. SEM photomicrographs of radially aligned crystallites above colloform laminated Mn-oxides (fracture surface of D44-4). **A.** Secondary electron image illustrates the texture better. **B.**Backscattered electron image illustrates differences in mean atomic number; lower mean atomic number is darker. The dark laminations in the colloform cores are higher in water content than the bright laminae.

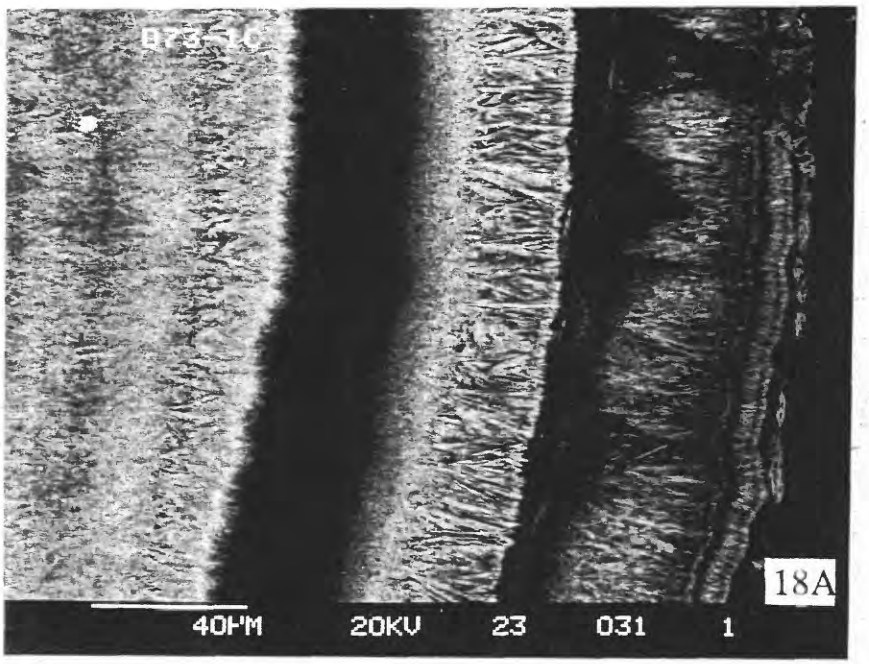

Figure 18. SEM photomicrographs of a DPTS from sample D73-1C illustrating laminae of aligned crystallites and AC oxides. **A**. Backscattered electron image, the AC layer is nearly black because of the high water content. **B**. Secondary electron image illustrates the surface texture of the layers.

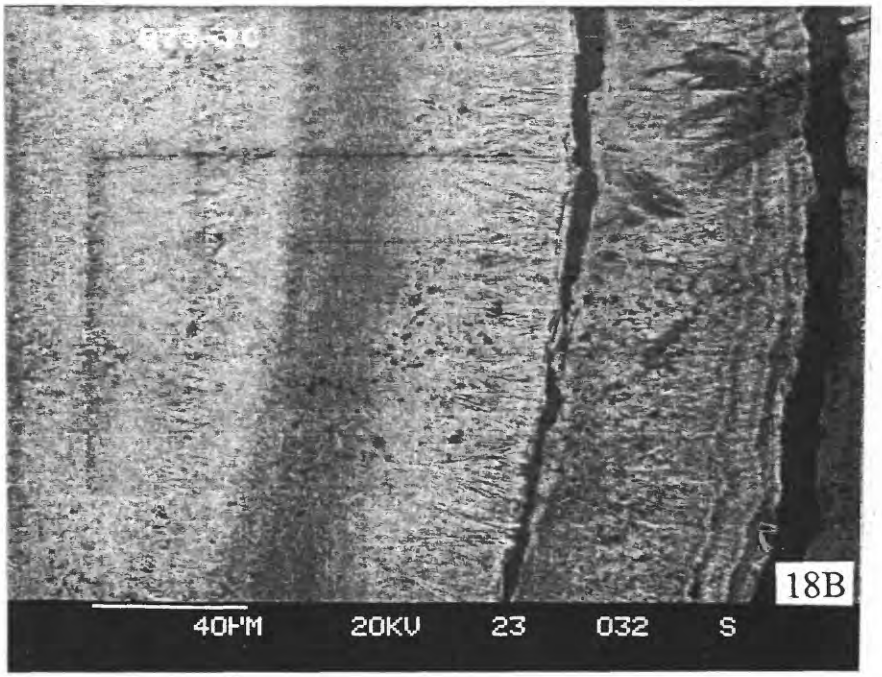

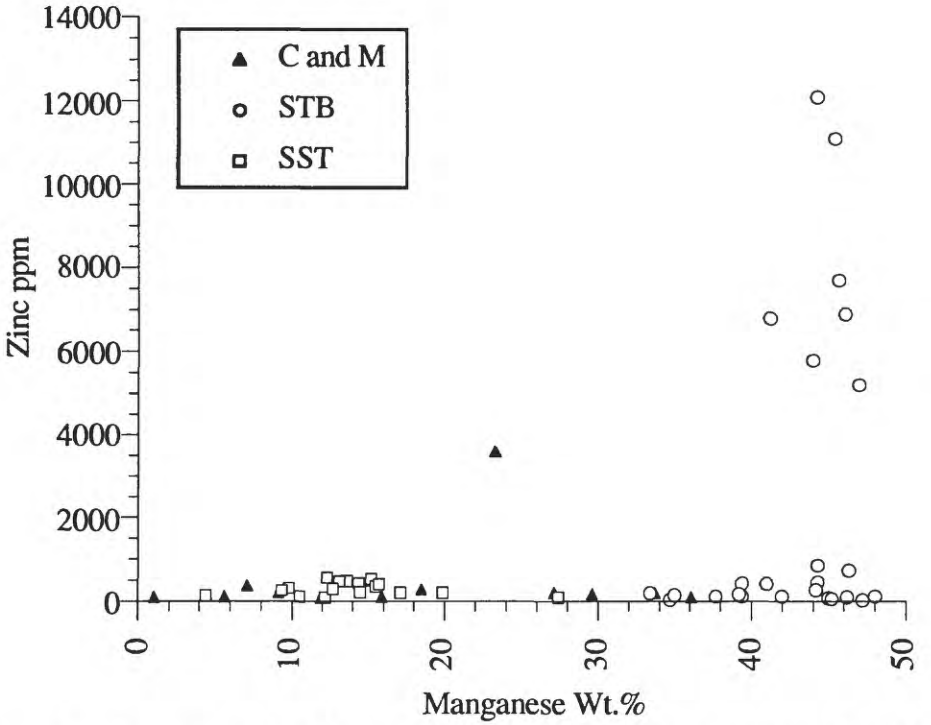

Figure 19. Scatter plot of Mn versus Zn. SST = Mn-oxide cemented sandstones, STB = stratabound Mn-oxides, and C and M = crusts and mixed origin deposits. The seven high Zn values are from layers of sample D28-1.

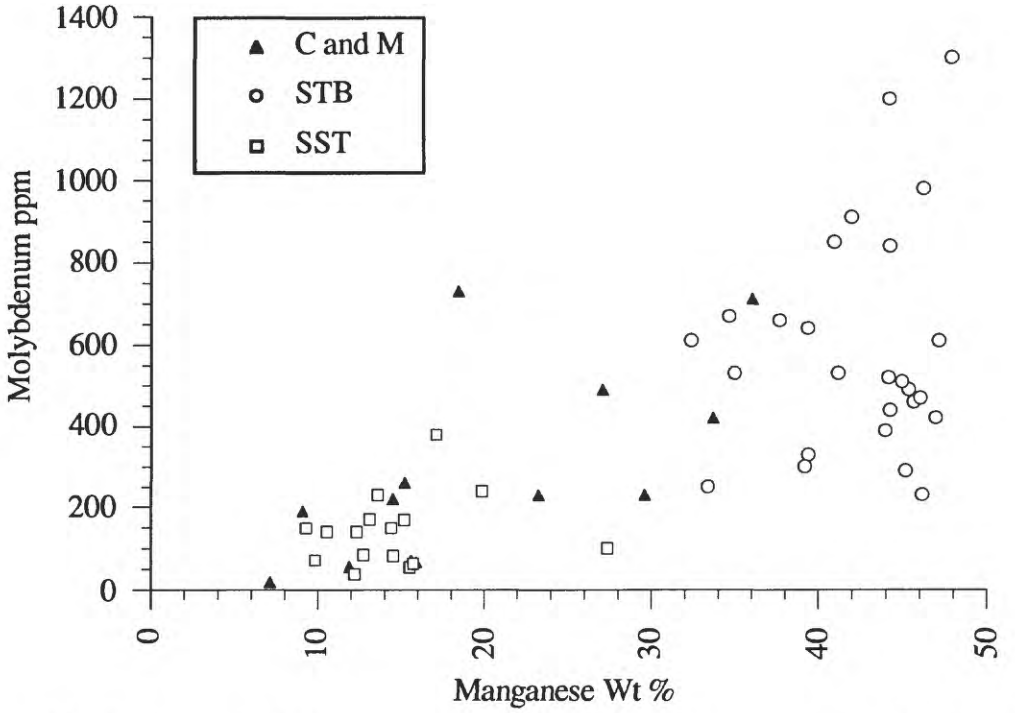

Figure 20. Scatter plot of Mn versus Mo. SST = Mn-oxide cemented sandstones, STB = stratabound Mn-oxides, and C and M = crusts and mixed origin deposits.

Figure 21. Photomicrograph mosaic of DPTS D8-12 with microprobe analysis points located. Scale bar represents 0.5 mm.

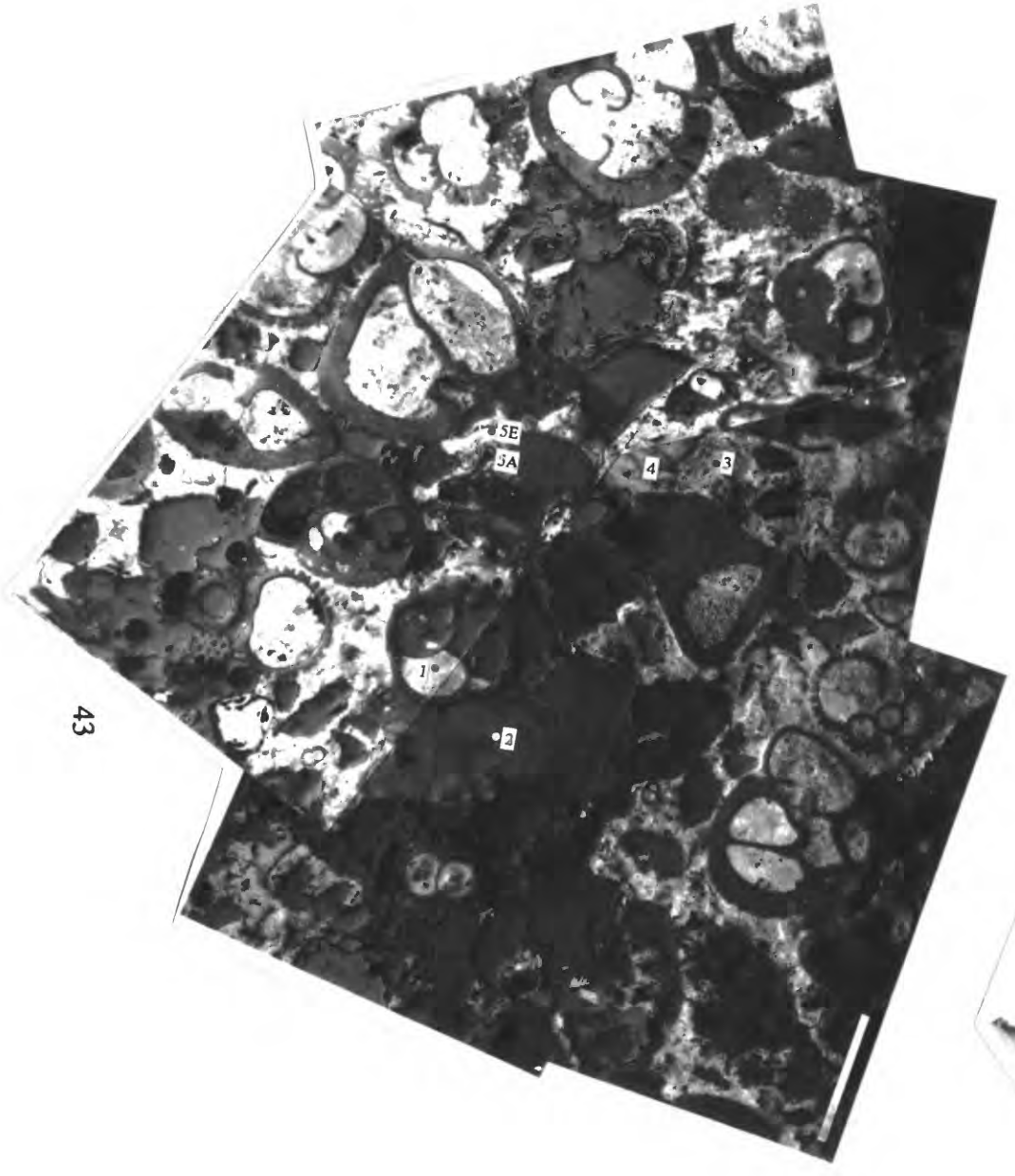

Figure 22A. Photomicrograph mosaic of DPTS D73-1C with microprobe analysis points located. Scale bar represents 0.5 mm.

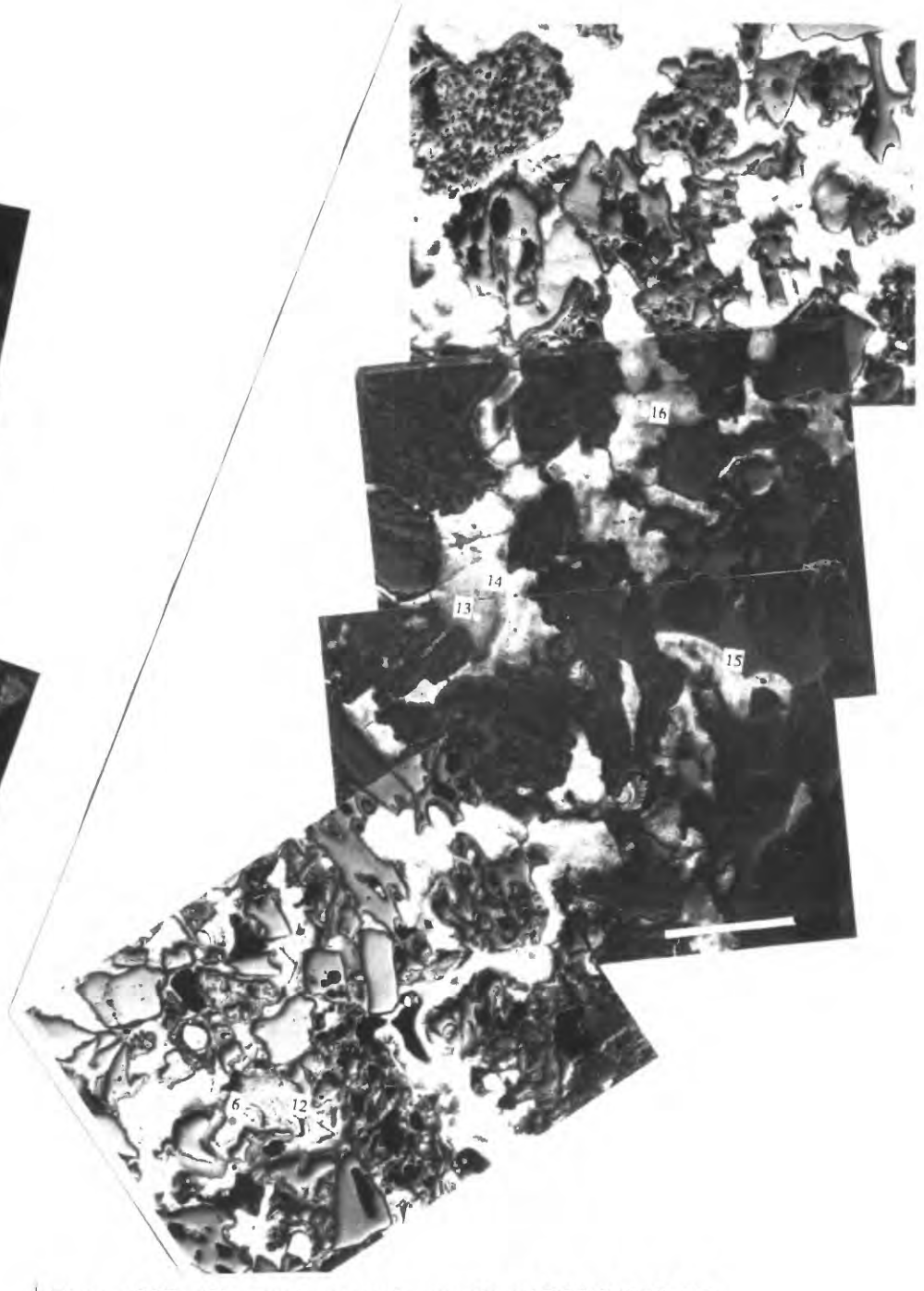

Figure 22B. Photomicrograph mosaic of DPTS D73-1C with microprobe analysis points located. Scale bar represents 0.5 mm.

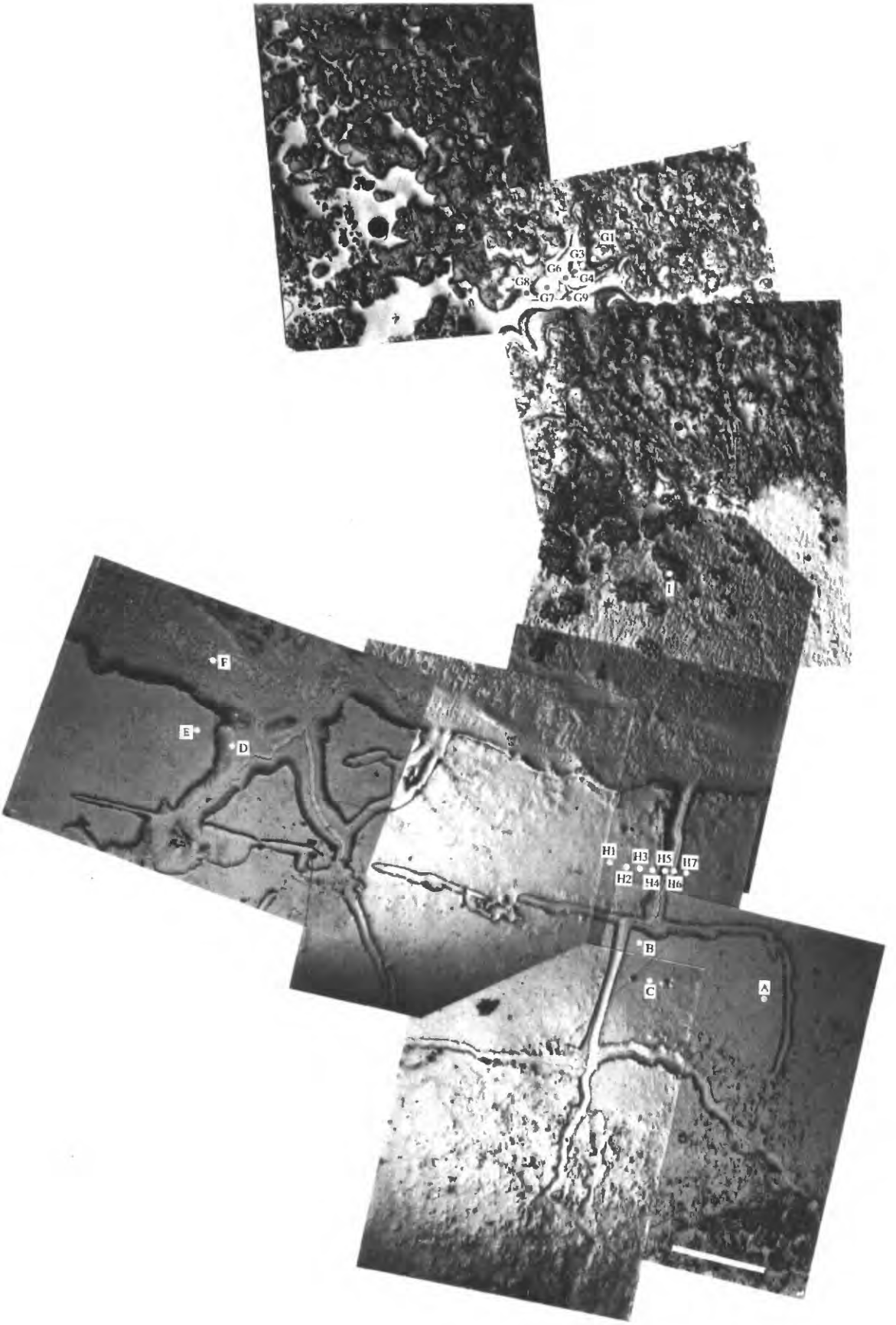

Figure 23. Photomicrograph mosaic of DPTS D3-3 with microprobe analysis points located. Scale bar represents 0.5 mm.

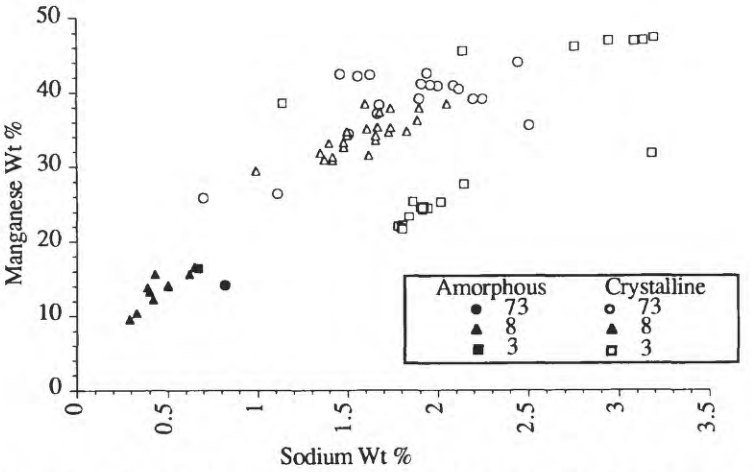

Figure 24. Scatter plot of Mn versus Na from electron microprobe analyses. Amorphous refers to areas of AC texture and crystalline refers to areas of crystalline texture. 3, 8, and 73 are dredge numbers.

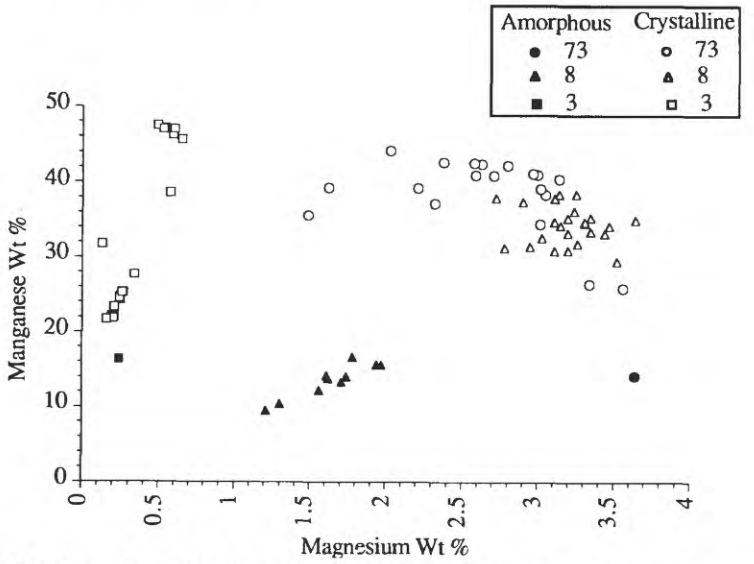

Figure 25. Scatter plot of Mn versus Mg from electron microprobe analyses. Amorphous = areas of AC texture and crystalline = areas of crystalline texture. 3, 8, and 73 are dredge numbers.

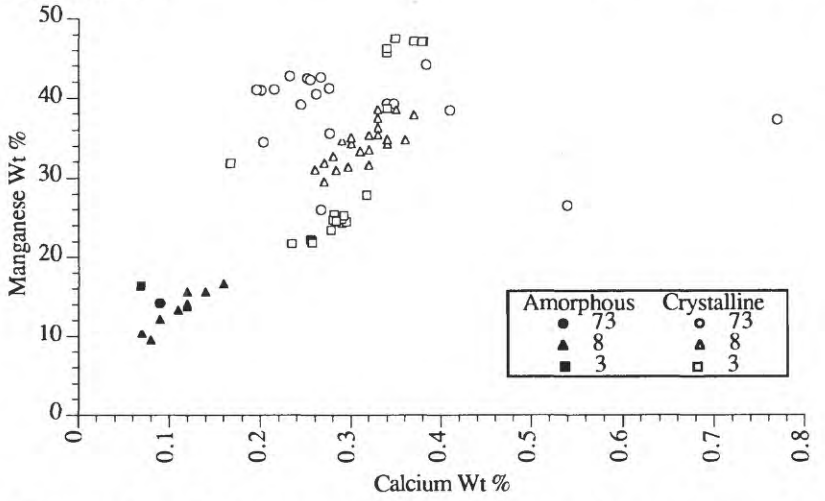

Figure 26. Scatter plot of Mn versus Ca from electron microprobe analyses. Amorphous = areas of AC texture and crystalline = areas of crystalline texture. 3, 8, and 73 are dredge numbers.

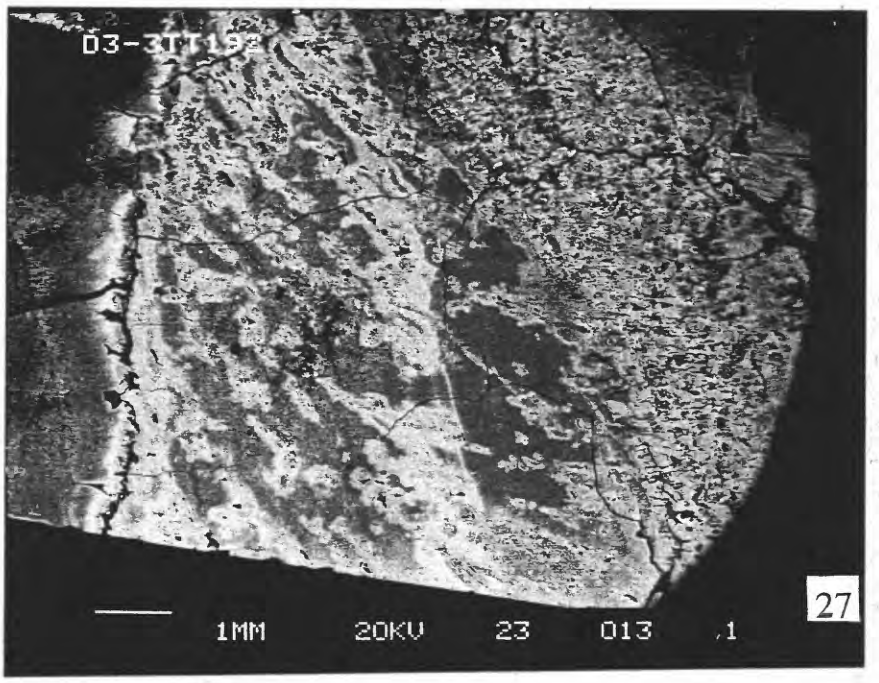

Figure 27. SEM photomicrograph of DPTS D3-3. At the center is a dense Mn-oxide layer that is microcrystalline (gray) with areas of radially aligned crystallites (white). The right side is a porous fibrous textured area.

Figure 28. A photomicrograph of DPTS D8-5 in plane reflected light. Short dimension of the photograph represents 1430 μm. Three phases of mineralization occur in this layer (from right to left) 1) colloform deposition, 2) dendritic fibers developing back into colloform, 3) microcrystalline fill of the previous phases.

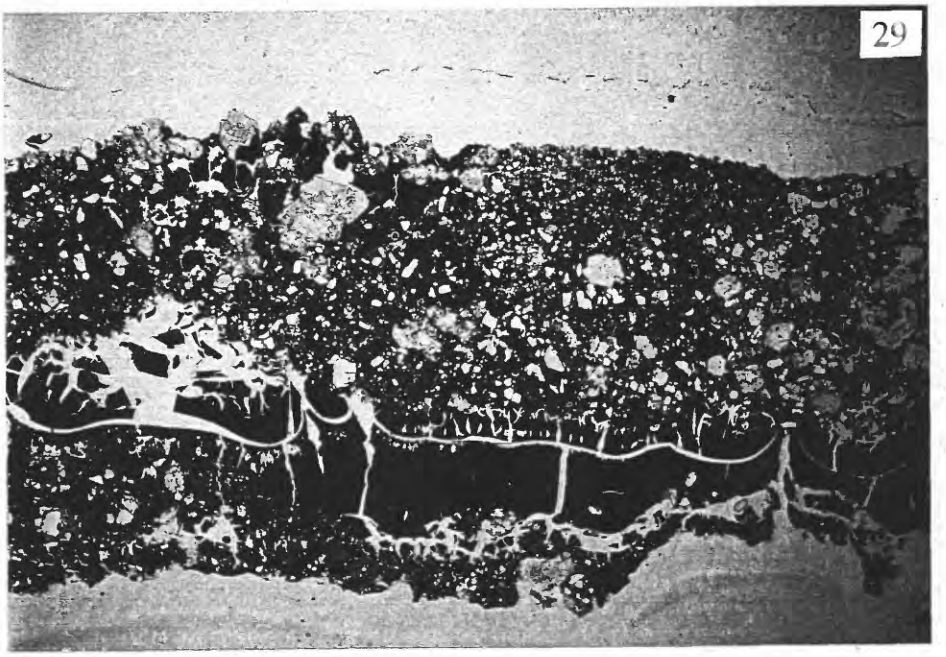

Figure 29. Photograph of DPTS D11-1, short dimension represents 25 mm. Note the desiccation of the stratabound layer, the curvilinear cracks follow laminae of Mn-oxides. The very desiccated layer is mainly an AC Mn-oxide layer.

Figure 30. Photomicrograph of DPTS D20-1 in polarized reflected light. The short dimension represents 140 μm. This is a perpendicular cut to fibrous porous Mn-oxides. The cores are AC oxides with radially aligned crystallites surrounding them.

Figure 31. Photograph of DPTS D28-4. The short dimension represents 25 mm. This photograph illustrates a fold or slump of the intercalated fibrous and dense layers.

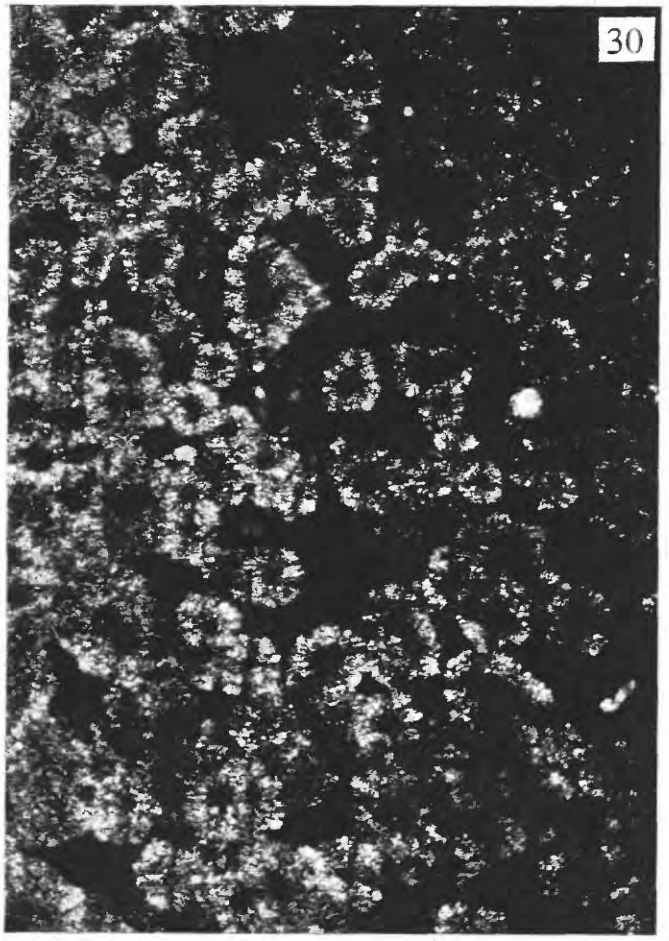

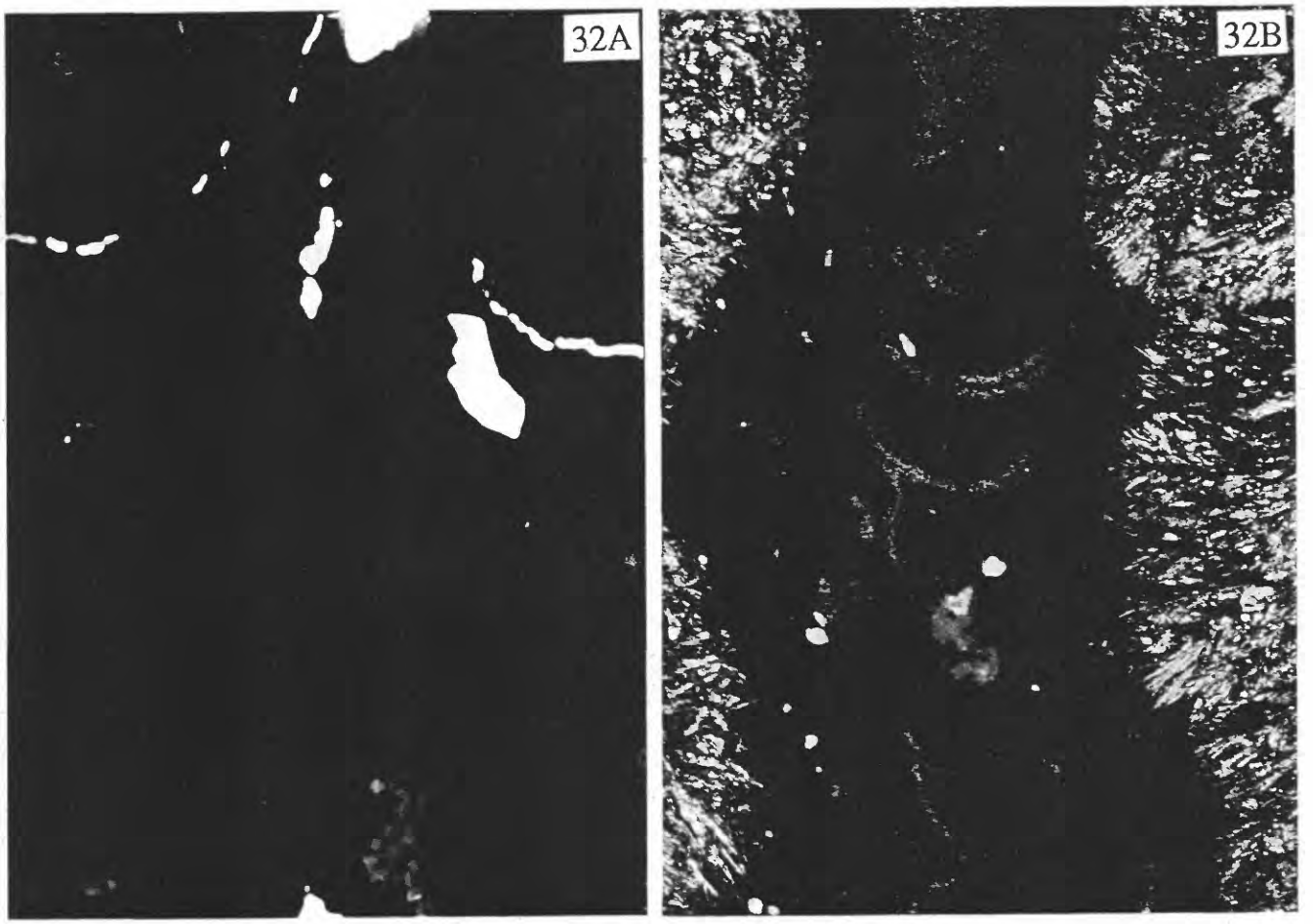

Figure 32 **A**. Photomicrograph of hematite "halos" from DPTS D33-2-3 in transmitted light. The short dimension represents 1100μm. **B**. Photomicrograph of the center part of 32A, in polarized reflected light. The hematite occurs in the black featureless areas. The microcrystalline Mn-oxides between the hematite indicates that Mn-oxide precipitation continued after deposition of the hematite. Short dimension represents 360μm.

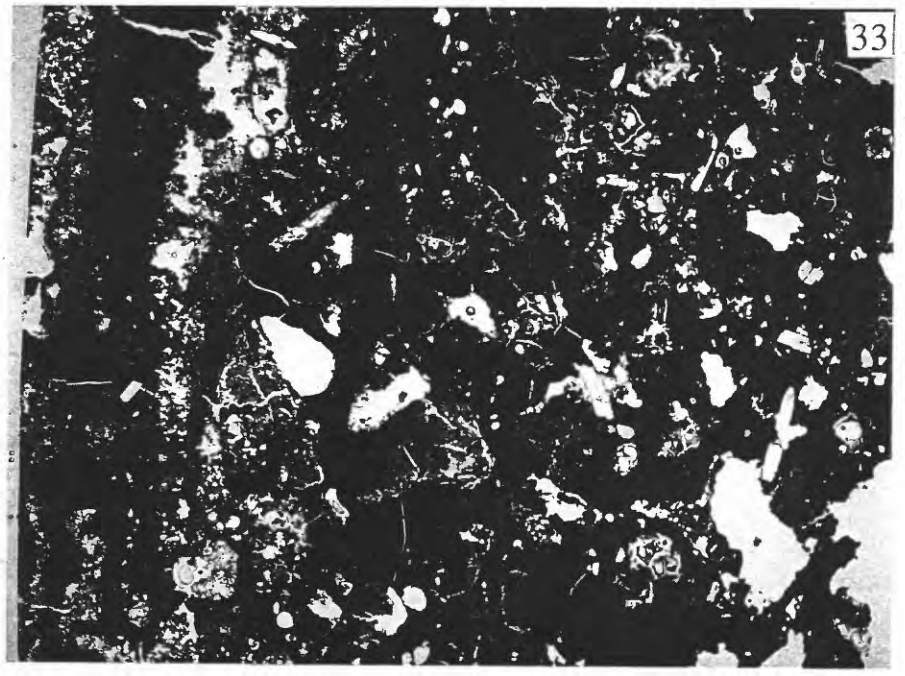

Figure 33. Photograph of DPTS D52-5, Short dimension represents 25 mm. Clasts are supported by the Mn-oxide cement and presumably are alteration products (clay minerals) of volcanic glass. Some clasts were lost (plucked) during the process of making the DPTS.

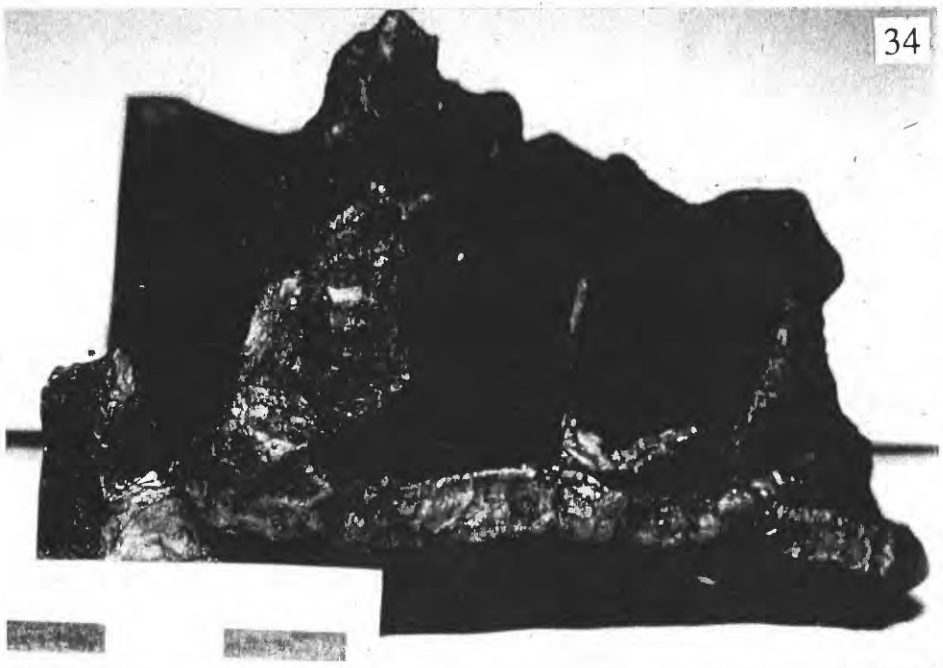

Figure 34. Photograph of sample D3-1, a stratabound Mn-oxide. Note the stockwork-like morphology, the filamentous black coating of the cavernous areas, and the Fe-rich sediment staining the sample.

Figure 35. Photograph of hand sample D41-1, a Mn-cemented volcaniclastic breccia. A thin stratabound layer of Mn-oxides runs through the sample.

Figure 36. Photograph of sample D52-4, a stratabound Mn-oxide.

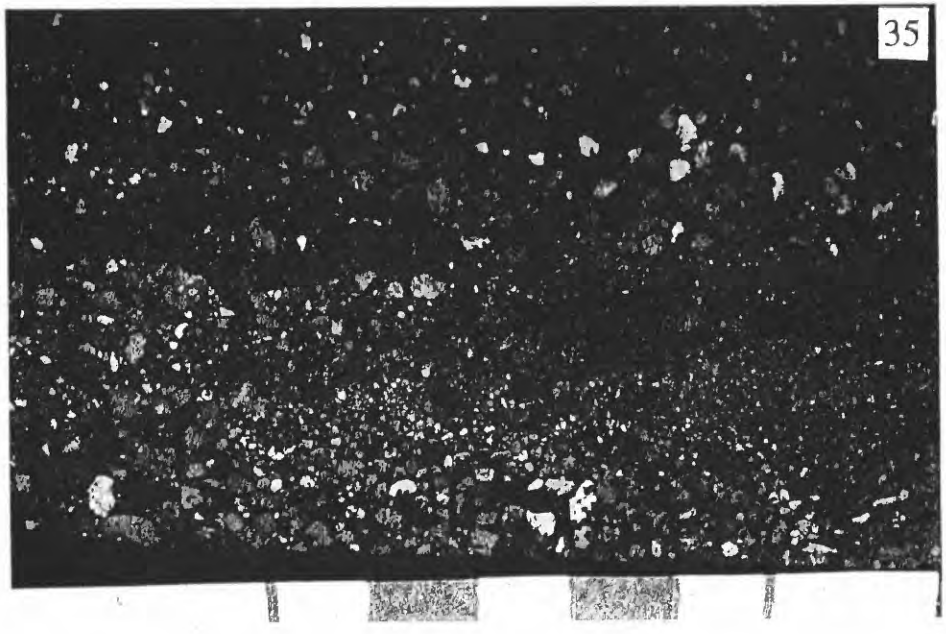

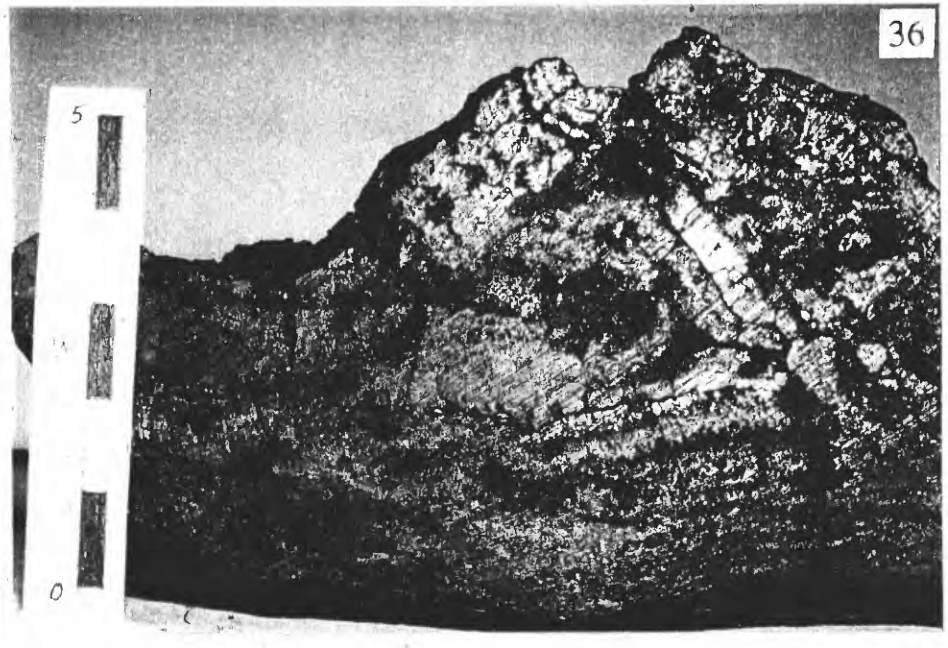

Appendix I

Microprobe Standards Used And Electron Microprobe Detection Errors

The electron microprobe used is an ARL SEMQ with 6 fixed channels and 3 variable channels this machine is housed at the U.S. Geological Survey, Menlo Park facilities. Fixed channels include the elements Na, Mg, Si, Ca, Ti, and Fe. Na and Mg are standardized on GSC glass standard with SiO2 as the low background standard and NiO as the high background standard. Si was standardized on GSC glass with MgO as the low background standard and NiO as the high background standard. Ca was standardized on GSC glass with synthetic spinel as the low background and NiO as the high background. Ti was standardized on TiO2 with SiO2 as the low background and NiO as the high background. Fe was standardized on Fe2O3 with SiO2 as the low background and NiO as the high background.

Variable spectrometers were set up with Mn, Ni, and Cu on channel one with a LiF crystal, using Kα lines. Mo, and Ba were on channel two with an ADP crystal, using Lα lines. S and Pb were on channel three with a ADP crystal, using the Kα for S and the Mα line for Pb. Sulfur was standardized on barite with NiO as high background. Manganese was standardized on a synthetic Mn_2O_3 standard, with NiO as high background. Nickel was standardized on NiO with Fe_2O_3 as high background. Copper was standardized on copper metal with Fe_2O_3 as high background. Molybdenum was standardized on Mo metal standard with Ag as high background. Barium was standardized on barite with NiO as high background. Lead was standardized on PbS with Au as high background. Low background for all elements on the variable channels was SiO_2.

The following are the averaged errors of detection in weight percent for each element analyzed by electron microprobe.

Na	0.043
Mg	0.068
Si	0.034
S	0.033
Ca	0.021
Ti	0.078
Mn	0.376
Fe	0.202
Ni	0.038
Cu	0.210
Mo	0.021
Ba	0.028
Pb	0.084

APPENDIX II

X-ray diffraction peak positions from all diffractograms are presented here. 10 Å peaks are those associated with the 10 Å phase, 7 Å peaks are those associated with the 7 Å phase, Vernadite and V1, V2 are the peaks generally associated with vernadite. The V1, V2, etc. are the position of double peaks when two are present. Plag = plagioclase, pyrox = pyroxene, qtz = quartz, calc = calcite, smec = smectite, ill = illite, olvn = olivine, and tr = trace amount. The * indicates that it is the second diffractogram of the same sample. Second diffractograms were done for the crystallinity study.

In several samples, halite occurs in the second diffractogram and is absent in the first. Presumably this is due to dehydration of adsorbed water from the sample.

For best results manganese oxide samples were run at 2 degrees 2 theta per inch, with a time constant of 10, and a range of 100.

Sample	10Å	10Å	10Å	10Å	10Å	10Å	7Å	7Å	7Å	7Å	Vernadite	V1	V2	Vernadite	V3	V4	Other Minerals
D3-1	9.4	18	26.7								35.4-36	36.5	37.1	63-66.4	63.4	65.6	-
*	9.3	18	26.6								36.6			63-66.6	63.6	65.7	-
D3-3I	9.1	17.9					12.1	25			36.2-40.5	36.7		65-67	66		-
*							12.4	25.2	41.1	51.6	36-39.8	36.3	38.8	65.4			Halite
D3-3II	9.2	17.9	26.8				12.2	24.9			36-45	36.8	39	63.4-66.6	65.8		-
*	9.2	17.8					12.4	25			36 - 40.2	36.4		63-66.8	65.6		Halite
D3-3III	9.5	18					12.4	25			35.2-40	36.8		65-68	65.9		-
*	9	18		42	50.8		12.4	25.2			35.4-39	36.6		63-67	65.4		-
D3-3IV	9.3	18	27.0		50		12.5?				34.6-37.4	36.5		62.8-66.8	63.7	65.9	-
*	9.3	18.1	26.4		50		12.4	24.7			35.8-39	36.5		63-67	63.5	65.8	-
D3-3V	9.1	17.8															-
D3-5	10.3	19	27.8								35.6			64.4-67.6	64.8	66.9	-
*	9.2	18	26.7								36.5			62.9-67.3	63.7	65.7	-
D3-8	9.1	17.9	26.9	42.5							35-40	36.6	38.2	63-67	63.7	65.9	-
*							12.4	25.5	42	50.4	36 - 38.8	36.6		63.1-66.4	63.7	65.9	-
D8-1-I	9.4	19					12.4	?			?			65.8			Plag,Pyrox
D8-2A	9.1	18.4					12.3				Broad Peak						Calc,Plag
*	9.1	18.4					12.3										-
D8-2B	9.2	18.2									35.8-37.4	36.9		65.9			Calc,Plag
*	9.2	18.4									35.6-38.2	36.9		66			-
D8-5-I	9.2	18.3	26.5				12.2	24.6			36.7			65.9			Plag,Calc,Pyrite
*	9.2	18.4					12.4	24.6			36.5			65.8			*
D8-7-I	9.2	18.2					12.4	24.8			36.7				65.6	66.1	Plag,Pyrox,Qtz
*	9.2	18.2					12.4				37			65.8			*
D8-7-II	9.4	18.6					12.2	25^			36.9			65.8			Plag, Qtz
*	9.2	18.2					12.3	25.2			36.4			65.4			*
D8-8	9.3	18.4	27.6								37.6			66.1			-
*	9.3	18.4	27.5	41	45.9	46.1					37.5			65.8			-
D8-12-I	9.2	18.2	26.7								35.4-38	35.8		65 - 66			Plag,Calc, Pyrox
*	9.2	18.3	26.6								35.8			65.8			*
D8-12-II	9.2	18.3									35-38	36.9		65 - 66.4			Plag,Pyrox,Qtz
*	9.2	18.3		42.3	51.9	56.5					35.2-37	35.8		65.9			*
D8-12-III									Mn indicated only by chemistry								Plag,Calc,Qtz
D8-20-I											36.5			65.8			Plag, Apatite
D8-20-II																	Plag,Pyrox
D8-20-III																	Plag,Pyrox,Smect
D11-1-I	9.1	18.1					12^				36 - 38			65.4 - 66.3			Plag,Calc,Pyrox,Qtz
*	9.4	18.2					12.4				36			65.9			*
D11-1A	9.1	18.1									35-36.6	peak interference					Plag,Pyrox
*	9.1	18									35-36						Plag, Pyrox
D11-2AI	9.1	18.1									35-37	peak interference					Plag,Pyrox,Calc,Qtz

Sample	10Å	10Å	10Å	10Å	10Å	10Å	7Å	7Å	7Å	7Å	Vernadite	V1	V2	Vernadite	V3	V4	Other Minerals
D11-2B-I																	Plag, Pyrox
D13-1-I	9.1	18.3															Plag,Pyrox,Qtz
*	9.2	18.2															*
D13-1-II																	Plag,Pyrox,Qtz
D15-1-I	9.2	18.3									34.6-38.2	peak interference		68.2?			Plag, Pyrox,Qtz
*	9.1	18.4									35.8			66			*
D15-1-II																	Plagioclase
D15-1-III	9.1	18	26.8								34.8 to 39	35.9		65.6 to 66.2			Plag,Pyroxene
*	9.2	18.2					12	24.6			34.8 to 38	35.8		65.7			*
D15-2-I																	Plag,Pyrox,Qtz
D20-1-I	9.2	18	27.8								35-39.8	36.7		62.8 - 66.2	65.8		-
*	9.2	18					12.4	25.6			34.8-38.4	36.6		62.8 - 66.2	65.7		-
D20-2-I	9.1	18.1	26.9								34.6-40.4	36.3		62.2 - 67.6	5.9 & 63.7		Plagioclase
*	9.1	18.1	26.8				11.6	25.8			35.8-38	36.4					*
D28-1A	9.8	18.1					12.4	25.5			35-37.8	36.6	37.2	65.8			Plag,Pyrox,Qtz
*	9.3	18					12.4	25.3			35.6-38	36.6		65.6			-
D28-1B	10	18					12.4	25.2	45	53.6	36.4-40.2	36.8		65.9			-
*	9.3	18					12.4	25			36-39.8	36.6	38.6	65.5			tr Halite
D28-1C-I	10	18					12.4	25.2			36.2-37.2	36.6	38.8	65.6			Quartz
*	9.1	17.9					12.3	25.1			36-39.8	36.4	38.7	65.4			*
D28-1C-II	10	17.9					12.3	25.2	46	53	36.3-39.7	36.8	39.5	65.8			-
*	9.4	18					12.3	25.2	44.5	53	36-39.8	36.6	38.9	65.8			-
D28-1D	10.4	18					12.4	25.2	45	53	36.4-39.7	36.7	39.1	65.9			Quartz
*	9.6	18.3					12.4	25.1	44.5	53.2	36.2-39.6	36.5	38.5	65.8			*
D28-1E	9.6	18.4					12.4	25.2	45	53	36.2-39.8	36.9	38.6	65.9			-
*	9.2	18.3					12.4	25.2	44.9	53	36-39.8	36.6	38.7	65.4			-
D28-1F	9	18.1	26.7								36.1-39	36.9		66			-
*	9.2	18.2					12	24.6		53	36.2-39.4	37.2		65.8			-
D28-1G	9.2	18.5					12.6	26	46	52.8	36.4-39.3	37.7		66			-
*	9.3	18.4					12	25.3	46	53	36.2-39.4	37.4		65.8			-
D28-1H																	Qtz, Ill, Smec, Chlorite
D28-2-I											35.8-37.8	36.8		65 - 66.1			Plag,Qtz
D28-2-II							12.5	25.1	44.7	53	36.4-40	36.7	38.7	65.8			-
D28-2-III	9.2^	18^					12.4	25.4			37			66			Plag,Qtz,Pyrox,Apatite
D28-3-I											35.8-37.8	36.6		65 - 66.1			Qtz,Plag
D28-4-I	9.4	18.6		46.0	53						36-39	37.5		65.1 - 66.8			-
*	9.2	18.5	28.0	46	52	60					36-39	37.5		65.7			-
D28-4C	9.3	18.7		46	52.4	60.1					37.5			66.2			-
*	9.2	18.4	28.0	46	52	59.8					36-39	37.3		66			-
D28-4D	9.4	18.6		46	52.6	60					37.7			65.9			-
*	9.2	18.6	27.8	45.5	52.4						36-39	37.4		65.9			-

Sample	10Å	10Å	10Å	10Å	10Å	10Å	7Å	7Å	7Å	7Å	Vernadite	V1	V2	Vernadite	V3	V4	Other Minerals
D28-5-I	9.2	18.4					12.2	25.1			36.2-38.2	36.9		65 - 66.2			Plag, Qtz
D28 -6-I	9.3	18.4					12.3	25			36.4-40	37		65.2 - 67	65.9		Plag,Calc,Qtz
D28-7-I	9.4	18.6									36.4-38.6	37.1		65.6 - 66.4			Plag, Pyrox,Calc,Qtz,Ill
*	9.2	18.7									37.2			66			*
D31-1-I	9.2	18.5									36.6			66			Plag,Pyrox,Quartz
*	9.2	18.5			56.5	63.8					35.8			66			*
D33-2-1-I	9.2	18.2					12.4	25.4			36.2-37.6	36.8		65.7			Plag
D33-2-1A	9.3	18.3					12.5	25.1									Goethite,Plag,Smec
D33-2-1B	9.2	18					12.5	25									Goethite
D33-2-2											36?						Goethite
D33-2-3-I											34.2-35.4			66.1			Plag,Qtz,Pyrox,Smec
D33-2-3B	9.2	18.6		45.6	52.4						36-39.2	37.3		65 - 67.4	65.9		-
*	9.2	18.4		45.5	53.2		11.9				36-38.8	37.2	37.5	65.6			-
D33-2-4I																	Goethite
*	9.2	18.4					12.3				36			65.8			*
D33-2-4II																	Plag,Pyrox,Smec
D33-2-4III							12.2										Plag,Goeth,Smec,Qtz
D40-3-I	9.2	18.2					12.3	25.1			36			66			Plag,Pyrox,Halite
*	9.1	18.4					12.4	24.7			35.8			65.8			*
D40-3-II	9.3	18.2					12.4	24.5			35.6-38.2	36.6		65.8			Plag,Pyrox,Qtz
*	9.1	18.2					12.3	25.5			35-37.2	35.8		65.6			*
D41-2AI		18.2					12.6	25		53	36.2-40	37.3		65 - 67.6	65.8		-
D41-2AII	9.4	18.6					12.4				36.6-40	36.9		66.1			Plag,Qtz,Pyrox
*	9.2	18.2					12.4				36.6			65.8			*
D41-2B-I	9.3						12.5	25.1			36.2-41	36.8		66			Plag,Qtz,Smec
D41-3AI							12.4	25.1	44	53.4	36.4-40.6	36.9	37	66			-
D44-1-I	9.2	18.3	19.8				12.6	25.3			35.6-36.6	36	37.2	65.7			Smectite, Plag
*	9.1	18.2					12.4	25.2	40.8	52.1	35.6-37.8	35.6	36	65.8			*
D44-3-I	9.3	18.1					12.4	25.2			35.7-40	36.6	38.2	66			Qtz,Plag,Pyrox
*	9.1	18.2					12.3	25.2	42.2	52.1	35.6-39.6	36.5		65.6			*
D44-4-I	9.2	18.3					12.6	25.2			36 - 39.8	36.8		65.9			Halite,Plag,Qtz
D44-6-I																	Plag,Pyrox,Olvn
D47-1-I	9.3	18.3^	32.0	42.6							35 - 39.9	36.6	37.2				Plag,Qtz,Pyrox
*	9.2	18.3									35-38.6	35.8					*
D47-2-I	9.3	18.3									36.2 - 38	36.6		66			Plag,Pyrox
D47-2-II	9.5	18.2									36^			66^			Plag,Pyrox
*	9.2	18.1									36.3			66			*
D47-2III	9.2	18.2									37			66.3^			Plag,Pyrox
D47-2-IV	9.3	18.3									36^			66.9^			Plag,Pyrox,Qtz
D51-1-I	10	18.6					12.3	25^			36.4 - 40	36.8	38.1	66			Plag,Pyrox,Qtz,Calc
*	9.8	18.4					12.2	25.6			36.4			65.8			*

Sample	10Å	10Å	10Å	10Å	10Å	10Å	7Å	7Å	7Å	7Å	Vernadite	V1	V2	Vernadite	V3	V4	Other Minerals
D52-4-I	9.2	18.4					12.4	24.5 ^			36.4 - 40	36.8		65.8			Plag,Pyrox,Apat?,Qtz
D52-4-II	9.4	18.6					12.4	25			36.1 - 40.1	36.8	38.4	65.9			-
D52-4-III							12.4	25.1			36.4 - 39.8	36.8	38.8	65.8			Plag
D52-5-I	9.2	18.2					12.4	25.3									Plag,Ill
D52-9	9.2	18.4					12.3	25.2	44.2	53	36.2 - 40.4	36.8		66			-
*	9.2	18.4					12.4	25.2	44.4	52.5							-
D52-9-I	9.3	18.4					12.4	25			36.3 - 39.8	36.8		65.7			Plag
D52-10	9.4	18.4	26.3			63.4	12.4	25			35 - 40	37		66			-
*	9.2	18.3	26.2			63.2	12	25.4			35.6-39.4	37.2		66			-
D52-10A	9.6						12.4	25.3			36.2 - 40	36.8	38.9				-
D52-10AII							12.3	25			36.2 - 39.8	37	39				Halite
D54-2-I	9.3	18.4									36 - 38.4	36.7		65.8			Plag,Pyrox,Qtz
*	9.2	18.4									36.4			66			-
D54-2-IA																	Plag,Ill
D55-3-I	9.2	18.5					12.5	24.6			37			66			Plag,Pyrox
*	9.2	18.4					12.4	25			36.4			66			*
D55-4-I							12.4	25			36.2 - 39.8	36.8	38.8	66			Halite
D56-1-I	9.6	18.5					12.1				36.4 - 38	36.7		65.9			Plag,Pyrox
D56-1-II																	Plag,Pyrox,Smectite
D56-2-I	9.2	18.2					12.1				36?			65.7			Calc,Plag,Qtz
*	9	18.1					12.2	25.6			37			64.4-65.8	64.7	65.5	*
D56-2-II	9.5	18.5					12	25.2			36.2 - 39.6	36.9		65.9			Qtz
*	9.3	18.7					12.3	25.2			36-39.6	36.5		65.7			*
D56-2-III	9.2	18.3									36.4 - 37	36.7		65.7			Calc,Plag
*	9.1	18.1									37			64.2-65.8	64.5	65.4	*
D56-4	9.4	18.2									36.2 - 41.6	37		66			-
*	9.2	18.3					12.1	25.2			36 -38.8	36.7		65.8			-
D57-2I	9.2	18.4					12.2				36.8	36.8		65.9			Plag, Pyrox, Smec
D57-2A	9	18.3									36.5	36.5					Smec,Plag,Pyrox
D57-2B	9.2	18.3	28.0				12				37	37		66			Smectite
D57-2C	9.3	18.6					12.3				37.3			66.2			Plag
*	9.2	18.4					12.4	25.2			37.5			65.8			*
D57-4-I	9.3	18.4			53.5						37.4			65.9			Plag, Qtz
*	9.1	18.4			53.5		12.4	25			36.5			65.5			*
D73-1A-I	9.2	18.2			51.6	56.6	12.6				36.4-37.6	36.8		65.8			Plag, Pyrox
*	9.2	18.4			51.4	64.3	12.3				35-37.4	35.6	36.3	66.1			*
D73-1C-A	9.1	18.1			53.3		12.2	25.3			37			65.8			Smectite, Plag, Calcite
*	9.1	18.2		42.4	53.5		12.3	25.4			35.8-38	36.7		66			*
D73-1C-B	9.2	18.3			51.5						36.1-38	peak interferenc		65.8			Calcite, Plag
*	9.2	18.4			51.5						36			65.6			*
D73-1D	9.1	18.4															Plag, Smectite,Pyrox

Sample	10Å	10Å	10Å	10Å	10Å	10Å	7Å	7Å	7Å	7Å	Vernadite	V1	V2	Vernadite	V3	V4	Other Minerals
D73-1F-I	9.4	18..6		40.6	52.7		12.2	25.6			36-39.2	37.6		66			Halite
*	9.2	18.4		40.7	52.4		12.4	25.6			36-38.8	37.3		66			*
D73-1F-II	9.4	18.4					11.8	25.6			36.2-39	36.9		65.9			
*	9.3	18.4		40.3	52.5		12	25.6			35.6-39	37.2		65.5			Halite
D73-2-1											36.9			65.9			
Average	9.3	18.3	33.5	48.7	52.1	59.4	12.3	25.2	44.1	52.7	36.7	36.7	38.2	65.8	64.9	65.9	
Maximum	10.4	19	32	46	56.5	64.3	12.6	26	46	53.6	37.7	37.7	39.5	66.2	66	66.9	
Miniumum	9	17.8	19.8	40.3	45.9	46.1	11.6	24.5	40.8	50.4	35.6	35.6	36	65.4	63.4	65.4	
Std. Dev.	0.23	0.22	8.47	4.68	1.87	5.18	0.17	0.29	1.63	0.73	0.56	0.42	0.90	0.17	1.01	0.40	

APPENDIX III

Peak height and height /width at half height measurements of 10 Å and 7Å d-spacings. An asterix indicates the second X-ray run of the sample.

Sample	Peak Height 10Å	Height/ Width 10Å	Peak Height 7 Å	Height/ Width 7Å	Morphology
D3-1	27.0	3.4	-	-	stratabound
*	69.0	8.1	-	-	
D3-3I	36.3	8.1	31.5	2.9	stratabound
*			[1]126.0	21.0	
D3-3II	41.0	9.1	24.5	3.3	stratabound
	30.0	6.0	82.0	16.4	
D3-3III	16.0	2.0	31.0	4.4	fibrous stratabound
*	19.5	1.3	[1]110.0	16.9	
D3-3IV	63.5	14.1	9.0	1.3	fibrous stratabound
*	52.0	6.1	24.5	2.6	
D3-5	11.5	1.3	15.5	4.6	stratabound
*	71.0	11.8	25.5	3.2	
D3-8	[1]124.0	35.4	-	-	stratabound
*	-	-	49.0	5.2	
D8-2A	5.0	0.7	9.0	0.9	Foraminiferal iron-rich layer
*	7.0	1.0	12.5	1.7	
D8-2B	17.5	2.5	-	-	Mn sandstone
*	22.0	3.4	-	-	
D8-5-I	35.0	5.4	33.8	4.2	Mn sandstone
*	51.0	10.2	82.0	14.9	
D8-7-I	37.0	9.3	12.0	1.3	Mn sandstone
*	43.0	9.6	30.0	4.6	
D8-7-II	27.0	5.4	28.0	2.7	dense Mn layer w/in sandstone
*	28.0	4.6	80.0	11.9	
D8-8	37.0	7.4	-	-	dense Mn layer w/in sandstone
*	35.0	7.0	-	-	
D8-12-I	54.0	13.5	-	-	Mn sandstone w/ dense layers
*	76.5	15.3	-	-	
D8-12-II	52.0	13.0	-	-	Mn sandstone w/ dense layers

Appendix III. Continued.

Sample	Peak Height 10Å	Height/ Width 10Å	Peak Height 7 Å	Height/ Width 7Å	Morphology
*	64.5	15.2	-	-	
D11-1A	11.8	2.9	-	-	Mn sandstone w/ dense layers
*	12.0	2.7	-	-	
D11-1-I	35.0	7.0	15.5	2.6	Mn Sandstone
*	17.0	2.3	35.5	5.1	
D13-1-I	13.0	3.3	-	-	Mn sandstone w/ dense layers
*	13.5	2.7	-	-	Minor Birn. not measured
D15-1-I	10.5	2.3	-	-	Mn sandstone
*	18.0	3.6	-	-	
D15-1-III	39.5	7.9	-	-	Mn sandstone w/ dense layers
*	40.0	4.4	17.5	15.9	
D20-1-I	24.5	3.2	-	-	stratabound
*	18.0	2.3	25.5	2.0	
D20-2-I	89.0	29.7	-	-	stratabound
*	67.0	11.2	17.0	1.2	
D28-1A	8.0	2.0	15.0	1.6	Fe-Mn crust
*	32.0	4.0	69.0	8.6	
D28-1B	10.0	1.7	55.0	7.9	stratabound
*	43.0	5.1	[1]145.0	18.1	
D28-1C-I	8.5	2.1	24.0	4.0	stratabound
*	55.0	7.9	[1]102.0	13.6	
D28-1C-II	9.0	0.9	18.0	1.6	stratabound
*	62.0	6.2	92.5	10.3	
D28-1D	18.0	2.3	62.0	7.8	stratabound
*	36.0	3.6	154.0	19.3	
D28-1E	14.3	1.6	28.5	2.6	stratabound
*	70.0	12.7	[1]122.0	17.4	
D28-1F	10.0	2.2	8.5	1.7	stratabound
*	[1]128.0	23.3	21.5	2.0	
D28-1G	6.5	1.9	11.0	2.0	stratabound
*	[1]114.0	28.5	23.0	2.6	

Appendix III. Continued.

Sample	Peak Height 10Å	Height/ Width 10Å	Peak Height 7 Å	Height/ Width 7Å	Morphology
D28-4-I	40.0	8.9	-	-	stratabound
*	84.0	21.0	-	-	
D28-4C	12.5	2.5	-	-	dense stratabound
*	69.0	17.3	-	-	
D28-7-I	26.0	4.3	-	-	Mn breccia w/ dense layers
*	44.0	6.3	-	-	
D33-2-3B	15.5	3.9	-	-	Mn breccia w/ dense layers
*	87.0	19.3	-	-	
D33-2-4I	17.5	5.8	6.0	1.5	Mn breccia
*	28.5	7.1	7.0	1.2	
D40-3-I	5.0	0.8	21.0	2.8	Mn breccia
*	27.0	4.9	54.0	8.1	
D40-3-II	9.0	1.5	18.0	2.8	Mn breccia
*	63.0	15.8	50.0	7.1	
D41-2AII	5.0	1.3	16.0	2.3	Mn breccia w/ dense layers
*	29.0	5.8	39.0	6.0	
D44-1-I	14.0	2.8	[1]110.0	27.5	Mn sandstone
*	24.0	4.8	[1]144.0	36.0	
D44-3-I	5.0	2.5	31.0	5.2	Mn breccia
*	29.5	3.9	90.0	16.4	
D47-1-I	13.5	1.7	-	-	Mn breccia
*	[1]102.0	25.5	-	-	
D51-1-I	17.0	1.3	40.0	4.4	stratabound
*	25.0	2.3	56.0	5.6	
D52-9	6.0	1.5	36.0	4.5	stratabound
*	32.0	4.0	[1]138.0	23.0	
D52-10	12.0	2.4	10.0	1.7	stratabound
*	93.0	18.6	24.0	2.2	
D52-10A	12.5	1.6	39.5	3.6	stratabound
*	-	-	80.0	10.0	
D54-2-I	34.0	8.5	-	-	Mn sandstone

Appendix III. Continued.

Sample	Peak Height 10Å	Height/ Width 10Å	Peak Height 7 Å	Height/ Width 7Å	Morphology
*	50.0	10.0	-	-	
D55-3-I	18.5	2.6	28.0	4.0	Mn sandstone
*	25.0	3.9	47.0	7.8	
D56-2-I	45.0	11.3	16.0	2.0	stratabound
*	53.0	10.6	29.0	2.8	
D56-2-II	18.0	2.3	46.0	4.6	stratabound
*	25.0	1.8	69.0	7.7	
D56-2-III	60.0	15.0	9.0	1.0	Mn sandstone
*	86.0	19.1	14.5	1.5	birnessite barely present
D57-2-C	25.0	6.3	10.0	1.3	Mn sandstone
*	29.5	9.8	14.5	1.8	
D57-4-I	79.0	22.6	-	-	Mn sandstone
*	130.0	37.1	-	-	
D73-1A-I	46.0	10.2	7.0	1.2	Mn sandstone
*	50.5	9.2	15.0	2.1	
D73-1C-A	20.0	5.0	3.5	0.5	Mn sandstone - volcaniclastic
*	29.0	8.3	34.0	4.9	
D73-1C-B	20.0	4.4	-	-	Mn sandstone - Foramniferal
*	31.0	7.8	-	-	
D73-1F-I	35.5	6.5	17.0	2.6	Stratabound
*	51.0	10.2	17.0	2.0	
D73-1F-II	65.0	13.0	17.0	2.4	Stratabound
*	80.0	16.0	23.0	2.3	
Average	38.2	7.9	42.4	6.4	
Maximum	[1]130.0	37.1	[1]154.0	36.0	
Minimum	5.0	0.7	3.5	0.5	
Std. Dev.	28.6	7.4	38.1	6.9	

[1] Height of peaks off scale were calculated by extending sides until they intesected.

APPENDIX IV

This appendix contains detailed descriptions of the doubly polished thin sections. All colors of manganese oxides are reflected light, anisotropic colors.

D3-3

This doubly polished thin section (DPTS) consists of dense manganese oxide layers (up to 3 mm thick), alternating with layers of fibrous, porous manganese oxides. Clastic material is uncommon; the clastic material that is present consists of volcanic rock fragments, plagioclase and pyroxene grains. Clastic debris is fine-grained, angular to subangular, and dispersed in the porous, fibrous manganese oxide. The interstices are lined by fibrous, porous manganese oxides. Three manganese-oxide morphologies occur: dense (without pore space), fibrous porous, and colloform botryoidal. These textures are composed of three crystalline types: 1) crystallites; 2) microcrystallites; and 3) amorphous to cryptocrystalline (AC). Crystallites are bluish-white, whereas microcrystallite areas are greenish-yellow. Dense areas are either homogeneously microcrystalline or a mixed crystalline texture. Colloform areas are composed of intercalated layers of aligned crystallites, microcrystallites, and AC layers. In general, fibrous, porous structures are internally composed of AC manganese oxides, although microcrystallites are not uncommon.
The largest dense layer is mostly microcrystalline. It has cross-cutting fractures that are filled with microcrystalline manganese oxides. These fractures appear to have been fluid conduits. This layer also has mosaics of aligned crystallites that radiate from linear AC cores. The AC cores are probably analogous to fibrous porous textures, and the crystallite mosaics represent a later phase of deposition. Aligned crystallites cross this dense layer and overprint the pre-existing microcrystalline texture (Fig. 27).
The contact between dense layers and fibrous porous layers can be sharp or gradational. The sharp contact probably represents a time of nondeposition of oxides, whereas the gradational contact may represent changing conditions through evolution of the mineralizing fluid during one depositional event.

D8-5

This sample includes manganese oxide layers (up to 4 mm thick) within a fine-grained, poorly sorted, manganese-oxide cemented, volcaniclastic sandstone. Foraminiferal tests are present as either molds in the manganese oxide cement or are completely replaced by the manganese oxides. Rarely is the original calcite of the foraminiferal test present. The predominant clastic material is volcanic rock fragments, although mineral grains and fresh glass are also present (see Table 3 for point counts). The most abundant minerals grains are plagioclase and pyroxene; opaque detrital grains are also present in minor amounts. Plagioclase and pyroxene grains commonly are zoned and/or twinned.
The manganese oxide cement is a mosaic of aligned crystallites usually radiating out from clastic grain boundaries. In pore spaces and areas where the cementing fluids were less restricted, manganese oxides have a colloform or laminated morphology. Amorphous to cryptocrystalline (AC) manganese oxides occur as layers within colloform structures and as fibrous structures. AC manganese oxides are bluish; all others are greenish-yellow.
The thickest manganese oxide layer extends across the DPTS and represents several episodes of mineralization. The initial mineralization occurred as colloform layers coating detrital grains. These colloform structures are, for the most part, AC manganese oxides; the colloform nature is apparent because of a thin laminae of microcrystalline manganese oxides. The botryoids created by the initial mineralization are the loci for the next phase of mineralization. Fibrous, dendritic AC manganese oxides extend out from the colloform botryoids into what at the time must have been open space (Fig. 28). The final phase of mineralization was the filling of the pore space around and between colloform botryoids and the fibrous dendritic oxides. The pore-filling manganese

oxides consist of aligned crystallites that commonly radiate out from the earlier formed manganese oxides. This final phase of mineralization did not completely fill all the pore space.
AC manganese oxides contrast sharply with crystalline manganese oxides in polarized light. The crystalline oxides have a greater hardness than AC manganese oxides, and thus, in plane reflected light they occur with a small positive relief.

D8-12
A fine-grained, iron-rich foraminiferal sandstone overlies a medium- to coarse-grained manganese-oxide-cemented volcaniclastic sandstone. The manganese oxide cemented sandstone is poorly sorted, although there may be crude size grading; mineral grains (plagioclase and pyroxene) and foraminifers are concentrated in a layer across the center of the DPTS. The clastic grains of the manganese-oxide-cemented sandstone are predominantly volcanic rock fragments, mineral grains, foraminifers, and glass fragments. Some (10%) of the volcanic rock fragments and glass fragments are altered.
The iron-rich, foraminiferal sandstone is predominantly fine-grained, but is poorly sorted, with coarse grains making up about 5% of the total. The majority of the clasts are whole and fragmented foraminifers and radiolaria; however, small angular mineral fragments (plagioclase and quartz) are also abundant. Agglutenated foraminifers are less common.
The manganese oxide-cemented sandstone is cemented uniformly but contains a dense layer (up to 3 mm thick) of manganese oxide within the layer of finer-grained mineral fragments and foraminifers. This probably represented a zone of weakness or greater porosity in the sediment.
The manganese oxides are microcrystalline with laminae of aligned crystallites occurring along margins of botryoids and along margins of dense layers. Microcrystalline manganese oxides and the majority of aligned crystallites are greenish-yellow in color. There are a few areas of aligned crystallites with a bluish color.
The thick manganese oxide layer consists of 3 sublayers: laminae of AC oxides with a desiccation crack sandwiched between laminae of aligned crystallites. These layers are contiguous, the texture indicates that they were deposited consecutively, one upon the other (Fig. 23).
Replaced foraminifers and radiolaria are present in moderate amounts, and a majority of these are concentrated along the margins of the dense manganese oxide layer.

D11-1
This specimen is poorly sorted, foraminiferal, manganese-oxide cemented, volcaniclastic sandstone. The clastic grains are predominantly volcanic rock fragments; they are angular and fresh. Microcrystalline manganese oxides are greenish-yellow. Crystallites reflect a bluish color. The manganese oxides cementing the sandstones are generally microcrystalline, but have larger aligned crystallites in layers of colloform botryoids. Crystallites are also larger along edges of open spaces.
A dense layer of manganese oxide, up to 5 mm thick, crosses the entire DPTS and cracked while drying. This layer consists of manganese-oxide laminae of aligned crystallites enclosing laminae of microcrystalline manganese oxides. Major desiccation cracks follow the curvilinear internal laminae of the manganese oxides. The inner microcrystalline laminae cracked in a regular boxwork pattern (Fig. 29).

D20-1
This DPTS contains a small lens of manganese-oxide-cemented volcaniclastic sediment enclosed in fibrous porous and dense layers of manganese oxides. Megascopically, the manganese oxide morphology is similar to D3-3, with intercalated dense and fibrous porous laminae forming intersecting layers. The clastic grains are fresh glass, volcaniclastic rock fragments, and mineral grains. The glass is unaltered and highly vesicular. Mineral grains include pyroxene, amphibole, quartz, and plagioclase. The grains are poorly sorted, and angular to rounded. A pumice pebble dominates the sediment lens. This DPTS was not point counted because of the paucity of detrital debris.

Manganese oxides are chiefly microcrystalline, although aligned crystallites and AC manganese oxides are common. Manganese oxides are greenish-yellow, with a few exceptions of aligned crystallites that are bluish. Textures include; colloform botryoidal, dense (without pore space), and fibrous porous.
As in sample D3-3, fibrous porous manganese oxides and dense manganese oxides are intercalated. The fibrous porous manganese oxides are overgrown with colloform layers of aligned crystallites that coalesce to form some of the dense layers.
The AC manganese oxides occur in three ways: as the cores of botryoidal and colloform manganese oxides; as fibrous dendritic structures within microcrystalline manganese oxides; and as the loci of deposition for aligned crystallites. An interesting texture occurs where elongate fibers of AC manganese oxides are coated by and cemented with aligned crystallites. The initial phase of mineralization throughout most of this section is in the form of fibrous dendritic strands of AC manganese oxides. Figure 30 is a view perpendicular to fibrous AC growth displaying a cross section of spherical radiating aligned crystallites.

D28-2
This sample is a coarse-grained manganese-oxide-cemented sandstone composed of volcanic and hydrothermal clastic debris. The cement-supported clastic grains are predominantly volcanic rock fragments, barite, and polycrystalline quartz. Altered volcanic rock fragments, fine-grained mud, and greenish-gold smectite of indeterminate origin are common. Less common are altered clasts of volcanic glass and altered mineral grains. There is a thick (8 mm), megascopically laminated manganese oxide layer at the base of this sample. Thin ferromanganese crusts occur on both ends (5 mm thick on one end and 2 mm thick on the other) of the section. Crusts on opposite sides of a sample indicate that it was part of a talus deposit during formation of at least the second crust. Hydrothermal oxides just below the crust are partly eroded.
Presumably, the barite and polycrystalline quartz are from the same hydrothermal source. They are concentrated with mineral grains in the middle of the DPTS. Volcanic rock fragments are more common above and below this layer. The delicate shape of some barite clasts indicates that they have not been transported long distances. Barite was not at chemical equilibrium in its most recent environment, as the clasts are etched.
The manganese oxides are green-gold and steel blue-gray. Manganese oxides are scaly (scallops of radially aligned crystallites), colloform, and laminated. The majority of the manganese oxides are microcrystallites and aligned crystallites. AC manganese oxides occur either as laminae within colloform textures or as the nucleating cores of colloform botryoids.
Scaly texture of manganese oxides occurs at the base of this sample. This texture is created by bands or layers of radial aligned crystallites. In some places the nuclei of the radial crystallites are detrital grains. The scales grade into the laminated texture composed of aligned crystallites in the thick manganese oxide layer.
Volcanic rock fragments just above the thick manganese oxide layer are altered to an iron-rich, orange clay mineral. This alteration is confined to the side of the clasts that faces the thick manganese oxide layer. This preferential alteration is probably due to the movement of mineralizing fluids along a zone of least resistance (present location of thick manganese oxide layer) which altered the near side of the adjacent clasts or deposited hydrothermal clay minerals on the clasts.
This sample appears to have been disrupted or deformed during mineralization. Colloform manganese oxide that formed along the edge of a large pyroxene grain was lifted away from the lath and cemented by microcrystalline manganese oxide. In another area, the manganese oxide botryoids are broken and recemented.

D28-4
This DPTS consists of intercalated, dense manganese oxide layers and fibrous, porous manganese oxide layers. The layers are in the hinge zone of an isoclinal fold or slump (Fig. 31). Microscopically, the slump broke colloform structures and produced minor deformation of dense, manganese oxide layers. There is a ferromanganese crust (about 4 mm thick) coating the upper

surface of the sample. Colloform hydrothermal manganese oxide is broken and slightly eroded below the ferromanganese crust.
Fine-grained sediment is present in some cavities of the fibrous porous oxides. The amount of detritus increases with depth below the ferromanganese crust. At the base, elongate manganese oxide fibers occur in a fine-grained sediment.
In general manganese oxides are dark gold-yellow. However, crystallites tend to be a steel-blue color, and in this section the finer crystallites have a dark gold color. Manganese oxides are predominantly colloform, although fibrous and dense (without pore space) layers are also common. Manganese oxide is predominantly microcrystalline, but crystallites and AC oxides are also common. The AC manganese oxides generally form the cores of colloform structures, cores of fibrous dendrites, and laminae within colloform structures. Dense manganese oxide layers were produced in places by the coalescence of colloform botryoids. In other places the dense layers are microcrystalline with isolated AC botryoids. Here the coalesced domain boundaries of the botryoids are ghosts. A fracture crosscutting dense layers of manganese oxides is partly infilled by AC and microcrystalline manganese oxides.

D28-6
This specimen is a foraminiferal sandy-siltstone in contact with hydrothermal manganese oxides. A thin (< 1mm thick) ferromanganese crust occurs between the hydrothermal manganese oxides and the siltstone. A ferromanganese crust about 5 mm thick occurs above the siltstone.
The siltstone has a fine-grained, pale-orange matrix. Sand grains are angular to euhedral mineral grains, volcanic rock fragments, and foraminifers. Clasts are matrix supported. Foraminifers and radiolarians are dissolved, and their molds are commonly iron stained. Rarely, there is minor calcareous or silicious material left in the molds. Volcanic rock fragments are generally subrounded and range from highly altered to fresh . A few fine-grained, detrital barite clasts occur. However, the majority of the mineral grains are pyroxene and plagioclase. Clastic material is rare in the hydrothermal manganese oxides.
The manganese oxides below the siltstone have several morphologies: colloform, fibrous porous, dense homogeneous, and dense laminated. These structures are composed of microcrystallites, crystallites, or AC oxides. The larger aligned crystallites are steel blue whereas the smaller crystallites are greenish-yellow. Microcrystallites are orange to greenish-orange or orangish-yellow.
Fibrous AC structures represent the initial mineralization in part of the DPTS. Here, aligned crystallites coat the fibrous AC oxide structures, but do not completely fill pores, leaving a porous network. In other areas, colloform structures have cores of AC oxides that are beneath intercalated laminae of crystallites, AC oxides, and microcrystallites.

D33-2-3
A manganese-oxide-cemented, medium to coarse-grained, volcaniclastic sandstone comprises the matrix of a volcaniclastic breccia. Two overlapping DPTS were cut through this sample. The majority of the clasts are volcanic rock fragments and mineral grains. Volcanic glass and clasts of fine-grained, iron-rich mud are present in minor amounts (see Table 3 for point count). One breccia clast is a highly altered volcanic rock fragment with replaced and partly replaced mineral grains along its outer margin (Fig. 10). Radiolarians and agglutinated foraminifers are present in minor amounts. Calcareous foraminifers have been dissolved and/or replaced; their initial abundance is not known. About half of the mineral grains and volcanic rock fragments are altered. Unaltered grains are common as are clasts of fresh volcanic glass. Mineral grains include plagioclase and pyroxene with minor quartz.
The manganese oxide crystallinity is diverse in comparison with other DPTS's of this study. Crystallites are larger than in any other DPTS, and the microcrystalline areas are finer. Crystallites are generally steel blue and rarely gold-yellow. Generally, microcrystalline manganese oxides are greenish-gold, but in some areas they are bluish. Manganese oxides either have a colloform botryoidal morphology or are dense-homogeneous. Manganese oxides occur as aligned crystallites, although microcrystalline and AC manganese oxides are also common. The

manganese-oxide cement between the closely spaced mineral grains is a mosaic of crystallites. The areas within larger pore spaces have colloform morphology. Colloform manganese oxides are alternating aligned crystallite, AC oxide, and microcrystallite layers.
An interesting feature of this sample is a hematite layer that coats manganese oxide botryoids. Hematite is bright red in plane transmitted light. Iron mineralization is late stage. Manganese oxide mineralization continued after hematite deposition (see Fig. 32).

D52-5

A manganese oxide impregnates an altered foraminiferal, volcaniclastic breccia. The major clasts are composed of yellowish-green claystone floating in manganese oxides (Fig.33). Sand size clasts of volcanic rock fragments and mineral grains are present, but not abundant. The clasts are cement supported. Mineral grains are plagioclase and pyroxene. Agglutinated foraminifers are a minor constituent. Altered tests of calcareous foraminifers are common.
The yellowish-green claystone is probably altered volcanic glass and volcanic rock fragments. It is crystalline with anisotropy indicative of a clay mineral. In many areas manganese oxides are dispersed in the fine-grained material. The clasts of mudstone have desiccation cracks and probably contracted during the process of post-recovery drying.
There is a megascopically laminated, dense layer of manganese oxides at the top of this section (up to 4 mm thick). Microscopically, this layer is made up of two layers of aligned crystallites separated by a thin colloform layer of AC oxides.
The microcrystalline manganese oxides of this section are copper-yellow in color. Most crystallites are steel blue; however, some are a greenish-yellow. The structure of the manganese oxides is somewhat unusual; around most of the detrital grains (including the clasts of yellowish-green mudstone) a halo of finely laminated colloform manganese oxides occurs. This halo is reminiscent of ferromanganese micronodules. The halos appear to have been the initial phase of mineralization. This was followed by deposition of aligned crystallites around and between many of the detrital grains, creating a mosaic texture in some areas. Finally, the interstitial areas were filled with microcrystalline manganese oxide cement.
AC manganese oxide occurs as thin colloform layers in the halo areas around clasts, and as layers or patches within the microcrystalline manganese oxides. Unlike most of the DPTS in this study, this thin section has no fibrous porous mineralization or remnants of such mineralization.

D73-1A

This sample was cut into two overlapping DPTS. It is a coarse-grained manganese-oxide cemented volcaniclastic sandstone. The detrital grains are volcanic glass and volcanic rock fragments with minor amounts of mineral grains and foraminifers (see Table 3 for point count). Altered and unaltered volcanic rock fragments are present. The glass fragments are pale-green or pale-brown in color, vesicular, and unaltered. Vesicles in the glass range from circular to elongate and from very abundant to rare. There are several clasts of flow banded glass. The sediment is moderately well sorted. The clasts are angular to subrounded. There is a finer-grained layer about half way through the sample that is almost entirely mineral fragments. This layer perhaps represents a change in an eruptive event. The manganese oxide cementation was not complete, and a great deal of porosity remains.
The manganese oxides are mainly microcrystalline and homogeneous in texture. Colloform structures are common around detrital grains, but most pore space is filled by microcrystallites. Crystallites are less common. The microcrystalline areas are golden yellow, and the crystallites are a steel blue color. Cores of colloform structures are generally AC manganese oxides. AC manganese oxides are also present as layers within the colloform structures. Crystallites occur aligned along the margins of manganese mineralization, where the manganese oxides were in contact with pore space.

D73-1C

This sample was cut into two overlapping DPTS. It is a manganese-oxide-cemented volcaniclastic sandstone underlying a foraminiferal sandstone. Point counts of both sandstones are available in Table 3.

The main detrital component of the volcaniclastic sandstone is volcanic glass, although volcanic rock fragments and mineral grains are common. Glass fragments are altered around their perimeters to a greenish-yellow clay mineral that X-ray diffraction analysis determines to be a smectite .

The foraminiferal sandstone includes euhedral and broken grains of pyroxene, plagioclase, and amphibole. Other detrital clasts include volcanic glass, radiolarians, and minor volcanic rock fragments. Original calcareous and siliceous tests remain for the majority of the microfossils. In a few microfossils, manganese oxides began to fill the fine structures of the tests. The mineralization of the foraminiferal sandstone occurs as dendritic areas of manganese-oxide-cemented sandstone adjacent to uncemented pockets of sandstone between the dendrites.

The manganese-oxide mineralization of the sandstone decreases with depth in the sample. The foraminiferal sandstone has the greatest amount of manganese oxide mineralization; the lower part of the volcaniclastic sandstone is porous with little cement. There are two manganese oxide layers (about 2 mm thick); one above the foraminiferal sandstone and one at the bottom of the volcaniclastic sandstone. These layers are both colloform. The manganese oxide cement is generally a mosaic of aligned crystallites. Colloform structures are rare within the cemented sandstones. Dense areas of microcrystalline manganese oxides are more common. Aligned crystallites are generally blue, but can be golden yellow. Microcrystalline areas are golden yellow to bluish-gold.

D73-1D

This sample was cut into two overlapping DPTS. It is a graded, manganese-oxide-cemented, pyroclastic sandstone. The lower part is coarse-grained with numerous broken and euhedral mineral grains. It also contains volcaniclastic rock fragments. As the grain size fines upward, the abundance of the volcanic rock fragments and mineral grains diminishes. The upper part of the bed consists largely of clasts of volcanic glass. This sample represents an eruptive deposit, as do the other samples of this dredge.

Two manganese oxide veins crosscut the sandstone, and the mineralizing fluids have affected the sediments around these layers. Volcanic glass fragments of the upper part of the sandstone are rimmed by greenish-yellow smectite rinds. The abundance of the smectite increases near the layers of manganese oxides. The thickest layer of manganese oxide is the center of an alteration band that is illustrated in Figure 10. Smectite rinds decrease in size toward the bottom of the section. Manganese oxide cement is sparse at the bottom of the section; where present, it occurs as a mosaic of aligned crystallites. As the cement becomes more pervasive upward, colloform structures become more common. The thick layers of manganese oxides formed initially as colloform structures that evolved into aligned crystallite laminae. Aligned crystallites are orange-yellow and blue, microcrystalline areas are greenish-bluish orange.

APPENDIX V

The lithologic descriptions of host rocks for the manganese oxide mineralization, and the morphology of the hydrothermal manganese oxide in hand samples for each of the nineteen dredges studied are presented in this appendix. The abbreviation after the dredge location indicate its province, CIP = central island province, NSP = northern seamount province.

DREDGE THREE, Southwest Guguan Ridge - CIP

Water Depth: 2,975-2,860 m. Total weight of manganiferous samples: 3 kg.

Dredge three is composed entirely of stratabound hydrothermal manganese oxide deposits. The samples are up to cobble size. Samples have surfaces that are usually granular to porous, but several have distinctive areas of fibrous porous manganese oxides. The porous texture also occurs in concavities of some samples (Fig. 34). In cross section most samples have the fibrous, porous texture intercalated with dense, dark-gray to metallic gray manganese layers. The thickness of each layer is variable (from 2 to 7 mm). Commonly layers will pinch out within the hand sample. The fibrous porous layers are never thicker than 5 mm; however, dense layers can be thicker. Layering is not necessarily planar, but more commonly layers are curvilinear or undulatory. The outer morphology mimics the curves of the internal layering. Several samples have manganese oxides perpendicular or at an angle to bedding reminiscent of stockwork with the matrix washed away. An ochre yellow to red mud was found in pockets on several samples and as a stain on most samples.

DREDGE EIGHT, Poyo Seamount - CIP

Water Depth: 2,880-2,200 m. Total weight of manganiferous samples: 36 kg.

Dredge eight is predominantly manganese-oxide-cemented volcaniclastic sandstones. The sandstones are medium-to coarse-grained with rare pebble-sized clasts. In general, they are poorly sorted with angular to subangular clasts. The sandstones are not uniformly cemented and can be very friable. Several samples contain foraminifers. Coarse pumice clasts (< 10 mm) occur in samples D8-17, D8-16, and D8-23.

The manganese oxide mineralization of this dredge has several morphologies: 1) sandstone cement, 2) dense gray or gray-brown in places submetallic, stratabound layers within the manganese oxide cemented sandstone, 3) dense dendrites within the manganese oxide cemented sandstones, 4) pale gray-brown, very porous, layers of pure manganese oxide. The dense manganese oxide layers within the sandstones in many places appear to occur along bedding planes. Samples tend to break apart just below these dense layers revealing in some samples, metallic botryoids of dense manganese oxide. D8-8 has dense, metallic, manganese oxide layers with linear flow structures (very elongated botryoids) as well as more typical botryoidal structures. This suggests that the manganese-rich rich fluids are able to migrate along bedding planes or fractures, depositing the thicker, dense, stratabound layers. The linear, elongated textures are due perhaps to the movement of fluids in a confined but open space.

The dendritic structures within the manganese oxide sandstones are areas where manganese oxide cement is more dense. Sandstone between the dendrites is more friable, and in one sample (D8-27) the area between dendrites contains little or no manganese oxide cement. The light gray-brown mounds of manganese oxide (4 above) occur on the tops or bottoms of the hand samples. Their porous fabric makes these layers structurally weak. It is likely that these layers also represent bedding-plane deposits that retained a more porous fabric than the dense manganese oxide layers of this dredge.

Samples D8-2, D8-12, and D8-22 each have a layer of iron-rich, fine-grained foraminiferal silty-sandstone. These iron-rich beds have little manganese oxide cementation. The contact between the iron-rich layer and the manganiferous sandstone is sharp.

DREDGE ELEVEN, Cheref Seamount - CIP

Water Depth: 1,380-894 m. Total weight of manganiferous samples: < 3 kg.

Dredge 11 consists of manganiferous volcaniclastic sandstones and breccias. Detrital clasts are subangular to angular, poorly sorted, fine to pebble sized. The manganese oxides have two morphologies: 1) cement for sediments, and 2) dense, gray submetallic to metallic layers within the sandstones. The dense manganese oxide layers have botryoidal surfaces (colloform in cross-section). Some of the dense layers have a metallic luster with a surface that is smooth and polished (giving the sample the look of native mercury)

DREDGE THIRTEEN, Supply Reef - CIP

Water Depth: 1,650-1,060 m. Total weight of manganiferous samples: < 1kg.

The few samples from this locality are small (up to 4 cm in length) tabular pieces (none are thicker than 8 mm) of manganese-oxide-cemented sandstone. The sandstone is predominantly fine grained, but poorly sorted with coarse sand and accumulations of pebbles on some fragments. The manganese oxide cement is black. Approximately half of the samples contain thin layers of dense submetallic manganese oxides.

DREDGE FIFTEEN, Ahyi Seamount - CIP

Water Depth: 1930-1120 m. Total weight of manganiferous samples: < 1 kg.

Dredge 15 consists of two samples of volcaniclastic breccia. The breccia is poorly sorted and crudely graded. The manganese oxide cement does not extend fully through the samples but is limited to a finer-grained layer on the bottom of the sample. Sample D15-1 is a manganese-oxide-cemented volcaniclastic sandstone (about 2 cm) below an iron-rich volcaniclastic breccia containing minor manganese oxides (4 cm). Above the iron-rich breccia layer is a thin (4 mm) layer of dense submetallic manganese oxide.

DREDGE TWENTY, Northwest Uracas - CIP

Water Depth: 1,640-1,510 m. Total weight of manganiferous samples: 7 kg.

Dredge 20 recovered stratabound hydrothermal manganese oxide deposits. Samples are similar in morphology to those recovered in dredge three. Dense manganese oxide layers are intercalated with layers of porous, fibrous (dendritic) manganese oxides. The manganese oxide layering is curvilinear. Fibrous, dendritic manganese oxides also occur on the outer surfaces of the samples. Several pieces are reminiscent of stockwork with the matrix washed away. In several samples, manganese oxides cement the base of pumice pebbles and cobbles, but does not completely cover them.

DREDGE TWENTY EIGHT, Cross Chain - NSP

Water Depth: 1,715-1,350 m. Total weight of manganiferous samples: 5.7 kg.

Dredge 28 recovered stratabound hydrothermal manganese oxides, manganiferous sandstone, breccia, and ferromanganese crusts. Ferromanganese crusts coat all of these samples on several sides which may indicate that they were dredged from a talus slope. Samples of non-mineralized substrate rock with ferromanganese crusts are also present in this dredge.

Sample D28-1 is unusual, with pebbles of pumice beneath dense hydrothermal manganese oxide (up to 80 mm thick). This sample has 6 distinct hydrothermal manganese oxide layers defined by variations in color, luster, and texture, plus a ferromanganese crust up to 5 mm thick. The dense layers in this sample vary from brown to dark gray and form two hemi-spherical masses.

D28-4 has alternating porous, fibrous layers and dense layers (similar to samples in dredges 3 and 20). The unusual aspect of this sample is that the layers double back on themselves, as if they were folded. This might have been created when the manganese oxides filled two intersecting fractures; or it might actually be a fold that is the result soft sediment deformation.

DREDGE THIRTY ONE, Eifuku Seamount - NSP

Water Depth: 1,715-1,500 m. Total weight of manganiferous samples: 130 grams.

Dredge 31 consists of small tabular pieces of manganiferous sandstone. The sandstone is fine-grained and friable. Manganese oxide cement is brownish black.

DREDGE THIRTY THREE, Kasuga Seamount - NSP
Water Depth: 1,170-600 m. Total weight of manganiferous samples: 2.7 kg.
Dredge 33 consists of altered iron-rich volcaniclastic breccia with manganese oxide cement and/or fracture fill. The manganese oxide morphology of these samples is, in general, dense submetallic manganese oxides cementing breccia clasts and filling fractures between clasts. In sample D33-2-3, manganese oxides form cement together with sand-size clasts as a matrix between larger cobble-sized breccia clasts. In samples D33-2-1 and D33-2-2, manganese oxides are disseminated and occur as stratabound layers in iron-rich fine-grained sediment.

DREDGE FORTY, Syoyo Seamount - NSP
Water Depth: 1,635-1,390 m. Total weight of manganiferous samples: 2.5 kg.
Dredge 40 consists of manganese-oxide-cemented volcaniclastic breccia. The majority of the clasts are pumice, with some volcaniclastic rock fragments. Clast size varies from sand to cobbles. Samples are well cemented. The manganese oxide cement is black to gray black, and there are small (up to 1 cm) lenses of dense manganese oxides within the cemented breccias. The manganese oxide cement fills some pumice vesicles, and manganese oxide stains many of the pumice clasts. Sample D40-3 is layered, 2 cm of poorly sorted manganese-oxide-cemented sandstone occurs above the manganese-oxide-cemented breccia layer. The sandstone layer has a 1 mm thick hydrogenous crust on top.

DREDGE FORTY ONE, Northwest Syoyo Ridge - NSP
Water Depth: 1,230-600 m. Total weight of manganiferous samples: 3.4 kg.
Dredge 41 consists of manganese-oxide-cemented volcaniclastic breccia, mineralized fine-grained sediment, and stratabound manganese oxide. The breccias are generally altered, iron-rich, with poor to moderate sorting (Fig. 35). The manganese oxides are grayish black to chocolate brown, some with a submetallic luster. The manganese oxides have four morphologies; 1) dense, stratabound layers, 2) porous fibrous, 3) cement for breccia, and 4) manganese oxide cement of fine-grained sediments (muds). Cemented, fine-grained sediments (4 above) can contain wavy elongate lenses, vesicles or pores within dense areas of manganese oxides, and areas of uniformly dense manganese oxides. Sample D41-1B may be inversely graded and has a thin (< 2 mm) hydrogenous crust on three sides. Samples D41-3A, -3B, and -3C have lenses of altered volcaniclastic breccia with a sandstone matrix; the manganese oxide mineralization occurred around these lenses.

DREDGE FORTY FOUR, Small seamount Northwest of Syoyo Ridge - NSP
Water Depth: 2,000-1,760 m. Total weight of manganiferous samples: 1.4 kg.
Dredge 44 consists of manganese oxide cementation in fine-grained sediment and volcaniclastic breccia. In sample D44-1 fine-grained clastic material is predominantly iron-rich mud. Manganese oxides appear to have impregnated the soft sediment; individual clasts (pods) of mud float in the manganese oxides. D44-3 is a poorly-sorted volcaniclastic breccia with manganese oxide cement. Manganese oxides occur in dense layers along what may have been bedding planes. Sample D44-4 consists of small pumice pebbles that have been permeated with manganese oxides.

DREDGE FORTY SEVEN, Ko-Hiyoshi Seamount - NSP
Water Depth: 2,030-1,600 m. Total weight of manganiferous samples: 2.56 kg.
Dredge 47 consists of sandy, manganiferous volcaniclastic breccia. Manganese oxide cement is black to grey black. Thin, stratabound layers with metallic luster occur in D47-1. Sample D47-2 has graded beds, possibly representing a turbidite.

DREDGE FIFTY ONE, Central Hiyoshi Knoll - NSP
Water Depth: 1,400-1,060 m. Total weight of manganiferous samples: 579 grams.

Dredge fifty one recovered two samples of manganiferous sandstone. The sandstone in D51-1 has layers of dense stratabound manganese oxides, 3 to 12 mm thick, that are discontinuous. Manganese oxides are brown black to gray black. D51-2 has a brownish-black bed of well cemented manganiferous sandstone up to 20 mm thick with a chocolate-brown, porous fibrous layer similar to those described in dredge eight.

DREDGE FIFTY TWO, Central Hiyoshi Knoll - NSP

Water Depth: 1,105-647 m. Total weight of manganiferous samples: 17.7 kg.

Dredge fifty two recovered manganese oxide cemented sandstones and stratabound manganese oxides. The manganese oxides of this dredge range from chocolate gray-brown to gray-black, with dull to metallic lusters. Many of these samples contain pockets and lenses of iron-rich, fine-grained sediments and have textures similar to those found in dredges 41 and 44. The large quantity of manganiferous material recovered in this dredge gives us a better look at these textures.

The manganese oxides have four morphologies: 1) dense uniform stratabound layers, 2) porous dense layers and lenses with incorporated clasts of fine-grained sediments, 3) porous fibrous layers, and 4) sandstone cement. Every sample has several dense uniform layers (1 above); the thickness of these layers varies, they commonly pinch out, and bottoms of dense layers may have botryoidal surfaces with metallic to submetallic luster or very smooth glassy surfaces. The morphology of sample D52-4 shows that the hydraulic pressure from the manganese oxide mineralization may have wedged apart the host sediment (Fig. 36). Sample D52-9 has bivalve impressions in the manganese oxides. Approximately half of the samples recovered have iron-rich muds incorporated in the hydrothermal manganese oxides.

DREDGE FIFTY-FOUR, North Hiyoshi Seamount - NSP

Water Depth: 1,640-1,250 m. Total weight of manganiferous samples: 3.8 kg.

Dredge fifty-four recovered manganiferous sandstone and breccia. Manganese oxide morphology is as a sandstone cement and has dense yellow-grey to grey stratabound layers. The sandstones of this dredge are foraminiferal; in general they are fine- to medium-grained, and well sorted. In sample D54-1 the sandstone overlies porphyritic basalt. The breccias consist of subrounded clasts of siltstones and altered volcanic rock fragments. The siltstones are permeated by manganese oxides.

DREDGE FIFTY-FIVE, Fukutoku Seamount - NSP

Water Depth: 1,780-1,070 m. Total weight of manganiferous samples: 9 kg.

Dredge fifty-five recovered manganiferous sandstone. The manganese oxide has four morphologies: 1) sandstone cement, 2) dense dendrites within the manganese-oxide-cemented sandstones, 3) porous fibrous layers, and 4) dense homogeneous layers. The sandstones contain foraminifers and are medium grained and moderately sorted. The dense dendritic structures are areas of more complete cementation within the sandstone; as in dredge 8, some of these samples have uncemented pockets between the dendrites. Sample D55-6 has a bivalve imprint in the manganese oxides. Layers of dense manganese oxides alternate with porous fibrous layers in several samples. Stratabound layers cover one side of several samples with polished botryoidal surfaces. The dense manganese oxide layer on the bottom of D55-1 has desiccation or cooling fractures in columns of hexagonal form, like columnar jointing in basalt.

DREDGE FIFTY-SIX, Fukutoku Seamount - NSP

Water Depth: 1,500-1,250 m. Total weight of manganiferous samples: 12 kg.

Dredge fifty-six recovered manganese oxide cemented sandstones, cemented breccias, and mudstone with some manganese oxide staining. D56-1 is a bioturbated mudstone with a ferromanganese crust above and a thin hydrothermal manganese oxide layer below; the manganese oxides permeate from above and below into the mudstone. D56-8 is a matrix-supported volcaniclastic breccia with a mudstone matrix. This sample has a very thin ferromanganese crust (2 mm) above the breccia and a thin hydrothermal layer below. The lower hydrothermal manganese oxide has permeated into the mudstone.

Manganese oxides of this dredge range in color from brown gray to dark gray and in luster from dull to metallic. The manganese oxides have four different morphologies: 1) ferromanganese crust, 2) sandstone and breccia cement, 3) dense dendrites within the manganese oxide cemented sandstones, and 4) dense homogeneous layers. Sample D56-4 has a dense metallic hydrothermal layer with a botryoidal texture; this layer fractures along the edges of the botryoids in a manner similar to columnar basalt (i.e. a honeycomb pattern) as in dredge 55. The dense, dendritic structures within the manganese oxide cemented sandstones are similar to those in dredges 8 and 55; the areas between these structures have little or no manganese oxide cement.

DREDGE FIFTY-SEVEN, Fukutoku Seamount - NSP

Water Depth: 1,730-930 m. Total weight of manganiferous samples: 7 kg.

Dredge 57 recovered manganese-oxide-cemented sandstone and breccia. The manganese oxides of this dredge have two morphologies; cement of sandstone and breccia, and dense homogeneous fracture fill and layers. The breccias recovered here are layered, iron-rich siltstone and mudstone clasts. The brecciation of these sediments may have been caused by the mineralization. Sample D57-2 has a disrupted bed of laminated, iron-rich mudstone that appears to have been fragmented by the mineralization.

DREDGE SEVENTY THREE, Kito-Io Jima - NSP

Water Depth: 1,620-1,240 m. Total weight of manganiferous samples: 10 kg.

Dredge 73 recovered manganese-oxide-cemented sandstone and ferromanganese crusts. The sandstones of this dredge vary from medium-to coarse-grained and are moderately sorted, with minor foraminifers. The sandstones are a greenish-gray and friable. Layers of dense manganese oxides occur within the sandstones, probably along bedding planes or weak areas of the sandstone.

Manganese oxides have four morphologies: 1) cement in sandstone, 2) dense stratabound layers, 3) dense dendritic cement of sandstone (as in dredges 8, 55, and 56), and 4) ferromanganese crusts. Sample D73-1C has a foraminiferal sand above a green volcaniclastic sand. The mineralization in the foraminiferal sand consists of dense manganese oxide dendrites with poorly cemented sandstone between dendrites as in dredges 8, 55, and 56.

Appendix VI

Section 1. Chemical Analyses by ICP spectroscopy of selected manganiferous sandstones.

	D08-1	D08-12-A	D08-12-B	D08-5-A	D13-1-A	D28-7-A	D33-2-2
Fe %	8.1	12.3	5.7	16.8	4.7	17.4	24.9
Mn	9.80	13.60	4.40	12.30	12.20	13.10	17.10
Si	17.58	14.03	19.59	10.43	18.42	8.32	6.31
Na	1.28	1.62	2.11	1.65	2.45	1.69	0.99
Al	0.40	4.10	7.90	3.60	6.90	2.70	1.11
Ti	0.41	0.29	0.44	0.81	0.35	0.67	0.06
K	0.41	1.14	0.56	0.63	0.36	0.58	0.82
Mg	6.6	2.00	1.80	1.61	2.22	1.08	1.17
P	0.043	0.140	0.064	0.300	0.029	0.380	0.290
Ca	6.20	2.70	8.50	3.30	6.30	2.59	0.93
H_2O^+	1.8	5.4	1.9	6.3	2.4	7.0	9.5
H_2O^-	1.5	2.6	2.3	4.7	1.2	10.3	5.9
CO_2	0.01	0.05	3.14	0.18	0.43	0.31	0.08
LOI[1]	-	-	-	-	-	-	18.1
Mo ppm	73	230	< 5	140	38	170	380
Co	50	740	18	930	27	1400	1100
Cu	210	4000	120	580	220	420	350
Ni	320	1400	130	1200	38	1700	130
Pb	< 50	300	< 50	650	< 50	1100	< 50
Sr	210	540	410	1000	300	1200	470
V	460	310	260	580	250	640	140
Zn	310	480	140	560	85	470	210
As	10	90	13	180	< 2.0	230	800
Ba	250	2800	260	1100	230	1100	2200
Cd	8.4	6.2	1.70	5.8	0.35	2.30	1.30
Cr	140	35	21	20	39	12	9.8
Y	16	39	38	130	17	150	21
Ce	< 10	53	< 10	310	< 10	430	< 60
Lithology							

Appendix VI, Section 1, Manganiferous sandstones. Continued

	D40-3-A	D40-3-B	D40-3-C	D54-2	D55-3	D56-1-B	D56-2
Fe %	3.9	4.4	5.2	6.5	4.4	5.3	1.61
Mn	9.30	14.40	15.20	14.50	15.50	15.70	27.40
Si	24.17	18.19	15.61	14.82	16.46	14.73	6.87
Na	2.67	2.37	2.06	1.96	2.45	2.20	2.45
Al	5.90	6.00	5.90	6.10	5.90	6.10	2.65
Ti	0.36	0.32	0.33	0.43	0.30	0.35	0.13
K	0.66	0.82	0.79	1.49	2.03	1.65	1.09
Mg	1.41	2.26	2.61	3.2	1.99	2.43	1.89
P	0.040	0.037	0.047	0.100	0.089	0.120	0.048
Ca	3.30	3.50	3.90	5.10	3.70	4.60	7.70
H_2O^+	3.5	3.1	4.2	3.9	3.5	6.0	5.4
H_2O^-	2.4	5.3	5.4	2.9	2.8	2.7	3.4
CO_2	0.25	0.06	0.05	0.03	0.02	0.59	5.90
LOI	8.0	11.6	12.8	20.6	-	-	-
Mo	150	150	170	83	55	64	100
Co	33	53	72	33	20	61	40
Cu	170	350	520	200	130	210	44
Ni	220	450	490	170	240	340	73
Pb	< 50	52	57	23	28	55	20
Sr	250	310	390	800	630	680	620
V	140	170	220	310	190	240	81
Zn	260	430	530	220	350	400	85
As	9.0	16	22	14	18	24	20
Ba	670	1500	2800	1000	1100	660	910
Cd	4.4	8.3	9.2	9.6	22	14	4.2
Cr	14	21	28	14	17	11	4.0
Y	26	33	38	19	22	25	13
Ce	22	21	10	39	53	73	14
Lithology							

Appendix VI, Section 1, Manganiferous sandstones. Continued

	D57-2	D57-4	D73-1A
Fe %	9.1	5.6	6.4
Mn	19.90	10.50	12.70
Si	12.01	17.44	16.88
Na	1.94	1.68	2.45
Al	3.40	7.30	5.70
Ti	0.16	0.30	0.42
K	1.60	1.02	0.95
Mg	2.11	3.5	2.25
P	0.130	0.071	0.079
Ca	2.37	6.60	4.00
H_2O^+	5.5	2.8	3.5
H_2O^-	4.8	1.7	2.6
CO_2	0.02	0.01	0.14
LOI	-	-	-
Mo	240	140	85
Co	220	220	31
Cu	77	310	160
Ni	300	110	170
Pb	20	< 10	20
Sr	480	620	430
V	170	210	310
Zn	210	110	290
As	62	22	20
Ba	1000	790	460
Cd	12	2.10	8.0
Cr	17	77	5.8
Y	14	13	25
Ce	31	15	< 10
Lithology			

Section 2. Chemical Analyses by ICP spectroscopy of stratabound manganese oxide layers.

	D03-1	D03-3	D03-5	D08-8	D11-1-A	D20-1-A	D28-1-B	D28-1-C-1
Fe %	0.32	0.23	0.67	0.59	1.56	0.51	0.97	0.66
Mn	39.40	48.00	42.00	39.40	44.30	46.30	44.00	45.70
Si	1.01	0.57	1.96	1.40	1.96	1.64	1.21	0.56
Na	3.04	3.49	3.34	2.17	1.54	3.26	2.16	2.60
Al	0.35	0.29	0.85	1.02	0.83	0.57	0.49	0.30
Ti	0.02	0.02	0.04	0.05	0.10	0.04	0.07	0.04
K	0.26	0.40	0.42	0.96	1.55	0.51	1.12	0.90
Mg	0.78	0.68	0.91	2.71	1.76	0.82	2.37	1.97
P	<0.025	<0.025	<0.025	<0.025	0.057	<0.025	0.098	0.130
Ca	1.77	2.13	2.15	1.61	1.07	2.36	1.50	1.46
H_2O^+	7.4	6.9	10.1	10.3	7.4	7.6	7.2	8.5
H_2O^-	20.1	4.6	9.6	8.2	3.9	3.0	7.4	8.2
CO_2	0.06	0.04	0.04	0.06	0.06	0.04	0.04	0.06
LOI	33.0		24.0	25.7			23.9	25
Mo ppm	640	1300	910	330	840	980	390	460
Co	29	25	33	31	85	9	130	64
Cu	13	28	20	250	400	39	910	670
Ni	47	82	61	490	840	120	950	490
Pb	< 50	10	< 50	< 50	100	70	140	130
Sr	380	400	380	500	1100	360	450	430
V	< 5	< 5	< 5	500	410	30	270	320
Zn	110	110	110	420	840	720	5800	7700
As	87	140	110	41	110	110	38	48
Ba	690	500	700	1200	5000	450	660	650
Cd	1.90	1.40	0.70	32	16	2.75	32	36
Cr	< 1.0	3.5	4.8	2.3	5.8	< 2.0	1.5	1.0
Y	< 5	< 5	< 5	25	38	< 5	20	21
Ce	< 60	< 10	< 60	< 60	22	< 10	31	17
Lithology								

Appendix VI, Section 2, Stratabound Layers. Continued

	D28-1-C-2	D28-1-D	D28-1-E	D28-1-F	D28-1-G	D33-2-3	D41-2BA	D44-1
Fe %	0.34	0.11	0.096	0.10	1.21	4.4	1.09	5.4
Mn	44.30	46.10	47.00	45.40	41.20	41.00	44.30	34.70
Si	0.45	0.10	0.17	0.22	2.71	1.45	1.05	7.06
Na	2.75	2.20	2.37	2.60	1.77	1.37	1.69	3.12
Al	0.30	0.12	0.11	0.22	1.39	0.51	0.57	0.82
Ti	0.03	< 0.01	< 0.01	< 0.01	0.09	0.03	0.04	0.04
K	0.73	1.16	0.94	0.73	0.98	1.41	1.55	0.91
Mg	1.87	2.46	2.05	1.68	2.07	1.76	2.16	1.14
P	0.190	0.110	0.082	0.170	0.065	0.075	0.031	<0.025
Ca	1.52	1.39	1.42	1.59	1.66	0.97	1.38	1.26
H_2O^+	8.2	7.8	8.5	9.3	8.2	9.3	7.3	5.7
H_2O^-	7.7	7.0	7.4	8.2	6.8	6.1	6.2	6.2
CO_2	0.05	0.05	0.08	0.11	0.12	0.68	0.03	0.01
LOI	25.8	24.6	24.3	24.8	21.7	23.2		
Mo ppm	440	470	420	490	530	850	1200	670
Co	14	< 5	< 5	< 5	98	470	31	170
Cu	820	350	230	400	760	130	120	300
Ni	640	200	150	230	830	520	360	130
Pb	110	150	150	110	58	< 50	30	15
Sr	380	450	470	510	510	660	680	280
V	240	290	330	360	270	71	130	< 5
Zn	12100	6900	5200	11100	6800	400	440	35
As	42	32	38	64	50	71	78	50
Ba	450	600	900	1200	2300	2100	2100	1700
Cd	34	37	70	79	50	4.3	23	< 0.2
Cr	2.3	< 1.0	< 1.0	< 1.0	2.3	6.8	2.5	1.5
Y	20	16	17	27	24	17	54	7.5
Ce	< 10	< 10	< 10	11	< 10	< 60	< 10	< 10
Lithology								

Appendix VI, Section 2, Stratabound Layers. Continued

	D44-1-A	D51-1	D52-10	D52-11	D52-4-B	D52-5	D52-9
Fe %	5.4	1.90	1.28	3.7	0.17	6.3	2.58
Mn	32.40	33.40	45.00	37.70	47.20	35.00	39.20
Si	7.29	5.94	1.59	4.82	0.18	5.28	3.88
Na	3.56	2.67	2.45	2.82	2.37	2.01	2.52
Al	1.19	2.70	0.46	1.24	0.11	0.10	1.27
Ti	0.06	0.14	0.04	0.10	0.01	0.07	0.09
K	0.69	1.30	0.85	0.84	1.04	1.40	1.01
Mg	1.07	2.32	1.44	1.25	1.98	1.44	1.69
P	<0.025	0.059	0.040	0.070	<0.025	0.160	0.088
Ca	1.55	2.76	1.62	2.03	1.48	1.54	1.79
H_2O^+	6.1	5.5	8.4	7.1	8.6	6.5	8.6
H_2O^-	9.4	5.1	7.0	8.0	4.2	6.5	6.4
CO_2	0.06	1.5	0.06	0.01	0.02	0.03	0.08
LOI	20.3		21.3	19.9			20.3
Mo ppm	610	250	510	660	610	530	300
Co	75	44	72	270	190	230	87
Cu	190	60	29	61	18	62	52
Ni	95	150	98	210	30	280	170
Pb	< 50	18	< 50	60	< 10	38	68
Sr	260	580	540	430	450	520	510
V	< 5	160	< 5	< 5	< 5	< 5	98
Zn	< 50	190	65	110	18	140	170
As	44	34	48	64	28	98	46
Ba	970	870	1000	800	530	1300	920
Cd	< 0.10	10	2.5	7.5	0.50	< 0.2	6.0
Cr	2.0	2.0	4.0	4.0	< 1.0	7.0	2.5
Y	7.0	8.6	< 5	8.4	< 5	6.9	10
Ce	< 10	15	< 10	41	< 10	< 10	14
Lithology							

Appendix VI, Section 2, Stratabound Layers. Continued

	D55-4	D56-4	D73-1F
Fe %	0.11	0.074	0.34
Mn	44.20	46.20	45.20
Si	0.19	0.05	0.41
Na	2.07	2.00	2.05
Al	0.14	0.30	0.51
Ti	0.01	< 0.01	0.02
K	1.65	0.90	1.05
Mg	2.41	2.24	2.05
P	0.026	<0.025	<0.025
Ca	1.69	1.61	1.61
H_2O^+	6.7	9.1	7.7
H_2O^-	5.9	8.9	6.0
CO_2	0.04	0.10	0.30
LOI		24.1	
Mo ppm	520	230	290
Co	40	< 5	6.4
Cu	120	54	43
Ni	340	120	54
Pb	10	< 50	< 10
Sr	590	680	570
V	150	280	770
Zn	260	90	50
As	48	42	52
Ba	900	1700	5000
Cd	13	13	2.85
Cr	< 1.0	1.5	2.5
Y	6.9	< 5	18
Ce	< 10	< 10	< 10
Lithology			

Section 3. Chemical analyses by ICP spectroscopy of ferromanganese crusts and other samples of mixed genetic origin.

	D08-12-C	D08-20	D15-1-A	D28-1-A	D28-3-A	D28-4-A	D28-6-A	D33-2-1	D33-2-3-
Fe %	14.8	4.7	15.9	9.7	6.6	4.8	5.6	12.0	8.8
Mn	7.10	11.90	9.10	23.30	5.60	15.90	15.60	18.50	14.50
Si	15.19	17.67	15.29	7.53	20.76	15.71	15.43	9.77	-
Na	1.63	2.17	1.46	2.30	2.00	2.12	2.11	1.67	-
Al	5.30	6.50	4.90	2.90	7.60	5.80	5.70	3.30	3.10
Ti	0.88	0.32	0.27	0.53	0.38	0.34	0.41	0.19	0.14
K	1.01	0.85	0.93	0.84	0.48	0.57	0.72	0.93	0.84
Mg	1.48	2.68	1.79	1.49	3.4	2.49	2.41	1.49	1.29
P	0.270	0.074	0.160	0.240	0.056	0.039	0.054	0.150	0.100
Ca	3.40	6.60	3.20	2.32	6.20	5.00	5.20	2.55	2.00
H_2O^+	6.1	2.2	5.3	7.3	1.6	3.7	3.8	6.9	-
H_2O^-	4.0	1.2	3.6	9.6	1.5	2.6	2.0	9.2	-
CO_2	0.19	0.83	0.08	0.29	0.02	0.75	0.93	0.15	-
LOI	-	-	-	-	-	-	-	-	-
Mo ppm	19	56	190	230	< 5	67	70	730	220
Co	530	140	180	840	42	33	51	560	< 5
Cu	400	900	130	1300	140	96	190	160	45
Ni	730	120	260	2300	54	57	300	300	69
Pb	330	< 50	< 50	530	< 50	< 50	< 50	< 50	< 50
Sr	800	400	360	620	290	360	420	410	410
V	340	220	230	300	260	320	460	66	320
Zn	370	83	220	3600	110	110	390	270	320
As	120	12	180	110	12	14	19	120	-
Ba	880	290	850	1000	310	620	890	750	510
Cd	1.90	0.65	1.85	9.1	0.45	7.4	16	1.05	0.30
Cr	24	71	26	17	85	8.0	8.5	27	6.5
Y	110	15	20	71	17	24	34	17	35
Ce	210	< 10	17	260	< 10	< 10	< 10	< 60	17
Lithology									

Appendix VI, Section 3, Crusts and Mixed Origin. Continued

	D33-2-3-	D44-3	D52-4-A	D52-4-C	D52-9	D54-2-I	D73-2
Fe %	8.8	2.24	6.5	3.4	3.6	10.0	19.5
Mn	14.50	36.10	29.60	27.10	33.70	1.06	15.20
Si	-	6.03	8.04	9.91	6.36	20.15	5.38
Na	-	3.12	1.78	2.30	1.90	1.83	1.60
Al	3.10	1.72	2.54	4.20	2.28	7.50	1.64
Ti	0.14	0.10	0.14	0.23	0.13	0.49	0.80
K	0.84	1.00	1.61	1.89	1.63	1.48	0.49
Mg	1.29	1.68	2.02	2.33	2.20	3.4	1.02
P	0.100	<0.025	0.110	0.090	0.076	0.089	0.560
Ca	2.00	1.56	1.98	3.10	1.96	4.60	2.21
H_2O^+	-	7.7	6.5	5.9	6.9	4.9	8.4
H_2O^-	-	7.0	4.4	2.7	4.7	6.6	11.0
CO_2	-	0.04	0.04	0.03	0.02	0.05	0.25
LOI		20.2	-	-	20.3	20.6	-
Mo ppm	220	710	230	490	420	< 5	260
Co	< 5	200	87	35	100	46	2700
Cu	45	410	67	100	62	260	180
Ni	69	170	210	190	270	120	1900
Pb	< 50	< 50	28	43	43	< 50	1600
Sr	410	330	700	500	550	680	1300
V	320	24	130	58	59	240	640
Zn	320	100	180	210	200	100	500
As	-	24	57	21	50	3.0	320
Ba	510	730	2200	580	1300	380	940
Cd	0.30	4.7	9.8	5.9	6.9	< 0.10	2.35
Cr	6.5	2.0	2.5	12	4.5	42	15
Y	35	9.8	13	16	12	16	200
Ce	17	18	18	18	27	60	830
Lithology							